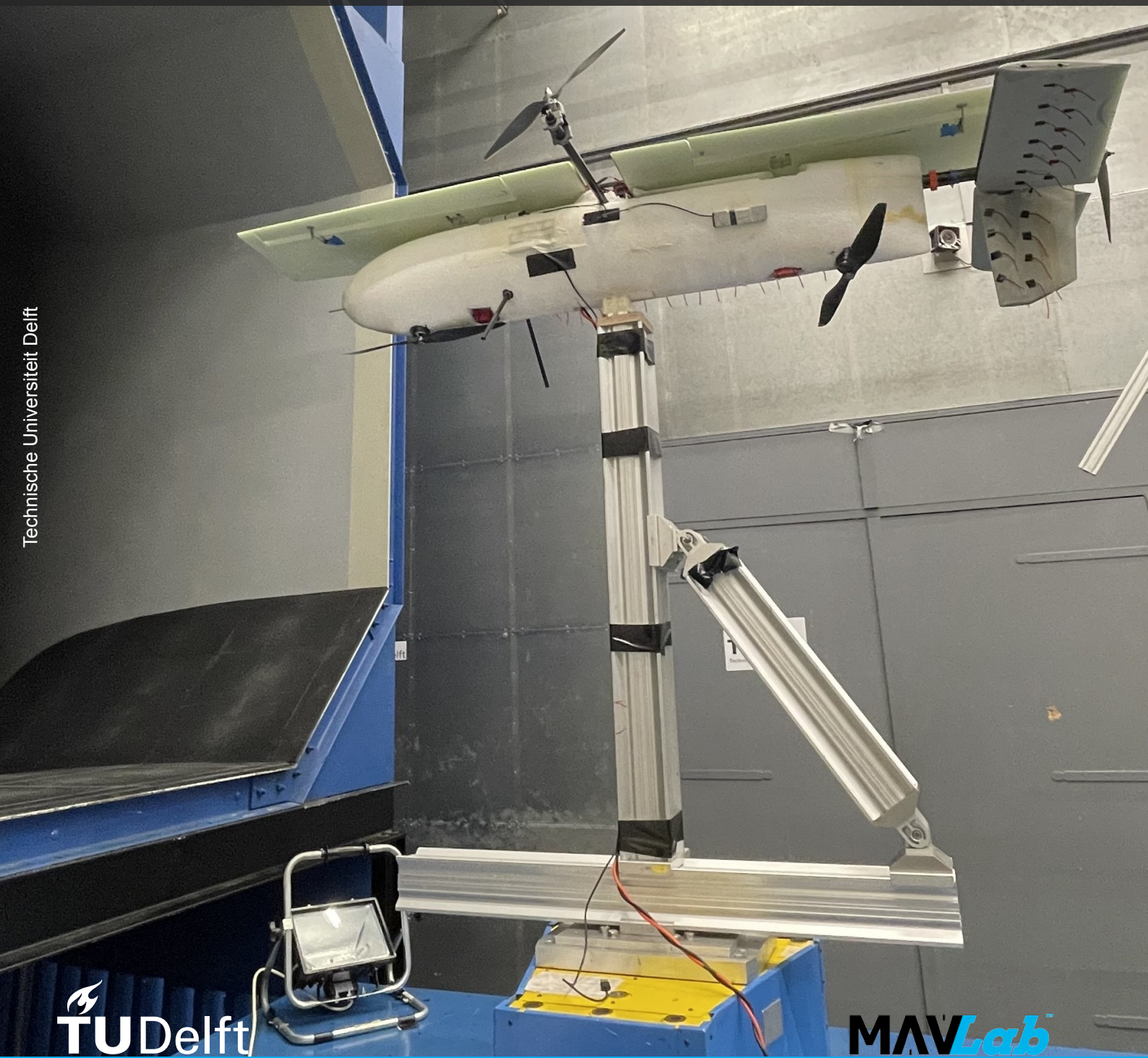


Synthetic Air Data System for Pitot Tube Fault Detection on Hybrid Vehicle

Improving the Safety of the Variable Skew Quad Plane

Frédéric D. Larocque

Technische Universiteit Delft



Synthetic Air Data System for Pitot Tube Fault Detection on Hybrid Vehicle

Improving the Safety of the Variable Skew Quad Plane

by

Frédéric D. Larocque

to obtain the degree of Master of Science
at the Delft University of Technology,
to be defended publicly on Tuesday July 4th, 2023 at 13:00.

Student number:	5481023
Project duration:	October, 2022 – July, 2023
Thesis committee:	Prof. dr. ir. Coen De Visser, Chair Prof. dr. Roberto Merino-Martinez, TU Delft, External Examiner Prof. dr. ir. Ewoud J.J. Smeur, Supervisor ir. Bart D. W. Remes, Supervisor ir. Tomaso M. L. De Ponti, Supervisor

An electronic version of this thesis is available at <http://repository.tudelft.nl/>.

Acknowledgments

These past two years studying Controls & Simulation at the TU Delft have acted as a catalyst, pushing me out of my comfort zone and deepening my knowledge and skill set as a future engineer through various experiences.

The completion of my master's thesis will have been a significant endeavour within a limited timeframe that helped me gain insights in the research process and experimental validation on a flying hybrid unmanned air vehicle. I am extremely grateful to have been able to work with talented and inspiring individuals. I would like to thank them, as they helped make this whole work possible.

First, I would like to express my sincere gratitude to my supervisors Ewoud Smeur, Bart Remes, and Tomaso de Ponti for their continuous guidance and assistance throughout the thesis. Their patient feedback and valuable expertise helped shape my work. I would also like to thank:

- Dennis and Kitso for supporting my work during experimental tests
- Freek for his constant willingness to help me troubleshoot various issues with hardware
- All other members of the MAVLab and Navy Team that helped me progress through my thesis

On a personal note, I would like to thank my parents, friends and family for the constant support and encouragement throughout this endeavour. Their belief in me has kept me on the right track during harder times.

*Frédéric D. Larocque
Delft, July 2023*

Contents

1	Introduction	1
1.1	Motivation	1
1.2	Research Formulation	2
1.3	Structure of Report	3
I	Scientific Article	4
2	Synthetic Air Data System for Pitot Tube Failure Detection on the Variable Skew Quad Plane	5
2.1	Introduction	5
2.2	The Variable Skew Quad Plane	6
2.3	Model-Independent Airspeed Estimation	7
2.4	Model-Aided Airspeed Estimation	8
2.5	Extended Kalman Filter for Airspeed Estimation	10
2.6	Fault Tolerance and Detection	11
2.7	Results and Discussion	12
2.8	Conclusion	15
2.9	Appendix A: Model Validation	18
2.10	Appendix B: Extended Kalman Filter Implementation	21
II	Literature Study	22
3	Introduction	31
4	Literature Study Plan	33
5	Variable Skew Quad Plane	35
5.1	VSQP Distinct Features	35
5.2	INDI	38
6	Fault Tolerant Control Methods	41
6.1	FTC General Principles	41
6.2	Passive FTC	41
6.3	Active FTC	42
7	Critical Failure Cases	45
7.1	Failure Mode and Effects Analysis	45
7.2	Selected Critical Failure Cases	46
8	Pitot Tube Failure	53
8.1	Use of Airspeed Data on VSQP	53
8.2	INDI Robustness	55
8.3	Airspeed Estimation	57
8.4	Pitot Tube Fault Detection Methods	61
9	Project Plan	63
9.1	Updated Research Objective	63
9.2	Methodology	63
9.3	Project Planning	64
10	Conclusion	67
	Bibliography	69

Appendices	73
A Failure Mode Analysis	74
B Rotor Loss Initial Calculations	87

Introduction

1.1. Motivation

Unmanned Air Vehicles (UAVs) are increasingly used for diverse missions ranging from military, search and rescue, aerial photography, surveillance to infrastructure inspection, and deliveries. They can operate autonomously without endangering the operator and provide mission capabilities where typical manned aircraft could not operate. Hybrid vehicles are a versatile subset of UAVs that can fly in both fixed-wing and Vertical Takeoff and Landing (VTOL) configurations, combining efficient lift and high speeds with precise hover flight capabilities.

The TU Delft's Micro Air Vehicle Laboratory (MAVLab) has been developing the Variable Skew Quad Plane (VSQP), a variant of the quad plane, where the whole wing rotates 90° around the vehicle's vertical axis, as shown in Figure 1.1. In hover flight, the wing is stowed over the fuselage, reducing landing space requirements and susceptibility to wind gusts. Lift is generated by four hover motors, with the vehicle acting as a conventional quadcopter. A pusher motor provides forward thrust to help transition to fixed-wing mode. In forward flight, the wing is skewed to its conventional position to generate lift and the hover motors are shut down. Ultimately, this vehicle is to be powered by hydrogen, a very flammable energy source, requiring a high degree of safety during its flight operations [1].

Accurate airspeed measurement is essential for ensuring safe autonomous flight, as aerodynamic forces are scaled with airspeed. Historically, the pitot tube is used to provide airspeed measurements. Control strategies that rely on airspeed-based gain scheduling are susceptible to instability and potential loss of the vehicle in the event of sustained airspeed measurement faults. The VSQP is no different from usual UAVs as it uses airspeed extensively in its control strategy, for both aerodynamic control surfaces effectiveness estimation and wing skew schedule. Pitot tube faults during VSQP test flights have resulted in loss of stability of the vehicle and required the safety pilot to take over.

Physical redundancy and a voting scheme are typically used to manage pitot tube faults on airliners [2]. Installing multiple pitot tubes is not always possible due to weight and space constraints. Additionally, low-cost pitot tubes used on smaller UAVs are prone to water blockage due to the absence of a drain tube [3]. When flying in a humid environment, it is highly likely that the pitot tubes could fail simultaneously, as their failure modes are not independent [4]. Therefore, it is highly pertinent to develop methods to estimate airspeed independently from the pitot tube. Using an alternate airspeed estimation, pitot tube faults can be identified and addressed.

Synthetic air data systems or the estimation of airspeed without a pitot tube is well covered in literature for fixed-wing and multicopter separately. These methods have limited direct application to hybrid vehicles due to their unique configuration and wide flight envelope. It is vital for hybrid vehicles to maintain a reliable airspeed estimation from hover flight to high-speed flight, including the transition. The main research goal and contribution of this thesis work is to estimate airspeed in the whole flight envelope of the VSQP using conventional sensors to ultimately detect pitot tube faults. While this work is specifically focused on the application to the VSQP, it is designed in a manner that allows its

applicability to other hybrid vehicles sharing a similar quad-plane configuration.



(a) VSQP in quad-mode configuration.

(b) VSQP in transition

(c) VSQP in forward flight configuration.

Figure 1.1: Different skew angle on the VSQP Prototype. In quad-mode configuration 1.1a, the wing is placed over the fuselage and hover motors are extended. In forward flight configuration 1.1c, the wing is completely extended and hover motors are stowed in the fuselage for reduced drag.

1.2. Research Formulation

The work was initiated with the general goal of improving the safety of the VSQP using Fault Tolerant Control (FTC) methods. The literature study in Part II helped narrow down the scope of the research to the development of a synthetic air data system and pitot tube fault detector for the VSQP. As such, the main goal of this work is:

Research Objective

To obtain pitot tube-free airspeed estimation and provide pitot tube failure detection capabilities for the Variable Skew Quad Plane (VSQP) in its whole flight envelope, using existing conventional sensors.

The main objective is airspeed estimation without the use of a pitot tube. Pitot tube detection comes as a secondary objective, as fault detection is a well-covered topic in literature. It is nevertheless included to provide a functional pitot tube fault detection system using the developed airspeed estimation. Research questions were defined to guide the thesis work for the different sections of the research objective. First, different airspeed estimation methods were investigated and developed:

Research Question 1

What methods can be used to provide a synthetic airspeed estimation for the variable skew quad plane, using existing conventional sensors?

Conventional sensors are defined as sensors already present on the vehicle such as the Global Navigation Satellite System (GNSS) receiver and Inertial Measurement Unit (IMU). Angle of attack and side slip vane will not be used to limit modifications to the vehicle.

The research question was broken down in sub-questions. Aerodynamic forces are function of air-speed. Knowing the physical characteristics of the vehicle's aerodynamic surfaces and their angle of attack, airspeed could be estimated. Therefore, the following research sub-question is defined:

Research Question 1.1

How can the forces generated by the VSQP's components such as the wing, fuselage, propellers, etc. be used to precisely estimate airspeed?

The different components of the VSQP can be modelled with varying fidelity. It is necessary to strike a balance between achieving sufficient fidelity for accurate airspeed estimation and developing a simple, adaptable model that can be easily customized:

Research Question 1.2

How can the forces generated by the VSQP's components be modelled to provide sufficient airspeed estimation precision without requiring complex modelling?

The main knowledge gaps for synthetic air data systems applied to hybrid vehicles is to estimate airspeed in the whole flight envelope. As such, accuracy must be assessed in different configurations:

Research Question 1.3

How does the airspeed estimation's accuracy change depending on the flight phase and skew angle?

Once an airspeed estimation method is obtained, pitot tube fault detection can be achieved. The ability of the method to detect different types of pitot tube failures must be assessed:

Research Question 2

Which types of pitot tube failure can be detected using the developed airspeed estimation method?

Airspeed estimation and fault detection are two separate functions that are interconnected. Airspeed estimation precision influences the detection capabilities of the fault detection system. Additionally, any fault in the estimation could lead to false detection of pitot tube failures. As such, the two systems must be studied as a whole:

Research Question 3

How can the synthetic airspeed estimation and pitot tube detection be integrated together to form one functioning system?

1.3. Structure of Report

This document is separated in two parts. First, in Part I is a scientific article with the main contributions and conclusions of this work. It can be read as a standalone document. Second, Part II consists of the literature study conducted for this work. The literature study starts from a general research objective aiming to improve the safety of the VSQP using FTC and converges to the review of strategies to detect and address pitot tube faults.

The literature study is structured as follows: chapter 4 introduces the research questions that guided the literature review and the research strategy used to answer them, chapter 5 presents the existing and new VSQP platform, chapter 6 assesses different FTC methods. Chapter 7 provides a Failure Mode and Effects Analysis (FMEA) based on literature to identify the most critical failure modes to be addressed on the VSQP. Chapter 8 provides an overview of topics relevant to the pitot tube failure. The initial project plan used for the thesis is presented in chapter 9. Chapter 10 concludes the review.

Part I

Scientific Article

Synthetic Air Data System for Pitot Tube Failure Detection on the Variable Skew Quad Plane

Frédéric D. Larocque*

Delft University of Technology, Netherlands

Faculty of Aerospace Engineering, Control & Simulation Section

ABSTRACT

Pitot tube-free airspeed estimation methods exist for fixed-wing and multirotor configurations, but lack direct applicability to hybrid unmanned air vehicles due to their wide flight envelope and changing dynamics during transition. This work proposes a novel synthetic air data system for the Variable Skew Quad Plane (VSQP) hybrid vehicle to allow airspeed estimation from hover to high speed forward flight and provide pitot tube fault detection. An Extended Kalman Filter fuses Global Navigation Satellite System (GNSS) and inertial measurements using model-independent kinematics equations to estimate wind and airspeed without the use of the pitot tube. The filter is augmented by a simplified vehicle force model. Pitot tube fault detection is achieved with a simple thresholding operation on the pitot tube measurement and the airspeed estimation residual. Accurate airspeed estimation was validated with logged test flight data, achieving an overall 1.62 m/s root mean square error. Using the airspeed estimation, quick detection (0.16 s) of a real-life abrupt pitot tube fault was demonstrated. This new airspeed estimation method provides an innovative approach for increasing the fault tolerance of the VSQP and similar quad-plane vehicles.

NOMENCLATURE

AR	Aspect Ratio [-]
a_x, a_y, a_z	Acceleration in Body Frame [m s^{-2}]
C_L	Lift Coefficient [-]
C_d	Drag Coefficient [-]
d	Diameter of Propeller [m]
e	Oswald Factor [-]
F	Force [N]
$f(x, u)$	State Dynamics [-]
$g(x, u)$	Output or Measurement Dynamics [-]
G	Control Effectiveness [-]
g	Gravity [m s^{-2}]
K	Gain, Parameter or Coefficient [-]
L	Lift [N]
m	Mass [kg]

p, q, r	Angular Rate in Body Frame [rad s^{-1}]
P	State Error Covariance Matrix [-]
Q	Process Noise Covariance Matrix [-]
R	Measurement Noise Covariance Matrix [-]
r	Residual [-]
S	Surface, Area [m^2]
T	Thrust [N]
u	Input [-]
u, v, w	Velocity in Body Frame [m s^{-1}]
V_a	Airspeed Norm [m s^{-1}]
v_a	Airspeed Vector [m s^{-1}]
$V_x^{NED}, V_y^{NED}, V_z^{NED}$	Ground Velocity in Earth Fixed Frame [m s^{-1}]
v_w	Wind Velocity Vector [m s^{-1}]
w	Noise [-]
x	State [-]
x_b, y_b, z_b	Body axis [-]
y	Innovation [-]
z	Measurement [-]
Z	Threshold [-]
α	Angle of Attack [rad]
β	Sideslip Angle [rad]
Λ	Skew Angle [$^\circ$]
μ_x, μ_y, μ_z	Wind Velocity in NED Frame [m s^{-1}]
ρ	Density [kg m^{-3}]
σ^2	Variance [-]
ϕ, θ, ψ	Euler angles [rad]

1 INTRODUCTION

Hybrid Unmanned Air Vehicles (UAVs) are versatile vehicles capable of flying in both fixed-wing and Vertical Take-off and Landing (VTOL) configurations. They leverage efficient wing-derived lift and achieve high cruising speeds, while also enabling seamless transitions to hover flight, providing precise VTOL capabilities. Hybrid UAVs require advanced control systems to stabilize their flight in various flying configurations.

Airspeed is one of the most vital measurements required for stable flight as aerodynamic forces vary with airspeed. Typically, a pitot tube is used to derive airspeed from dynamic

*Email address: f.larocque@student.tudelft.nl

pressure measurements. Unlike on larger aircraft, low-cost pitot tubes normally used on UAVs are particularly prone to water blockage due to the absence of a drain tube. The pressure slowly or immediately drops, resulting in a reduced or zero airspeed reading [1]. When flight controller parameters are scheduled with airspeed, any sustained airspeed measurement fault can lead to a loss of stability and ultimately the loss of the vehicle.

For larger vehicles, redundancy and a voting scheme can be used to isolate faulty pitot tubes and maintain a reliable airspeed estimation [2]. On smaller UAVs, such a strategy cannot be easily implemented due to weight and space constraints. Additionally, if one pitot tube is subjected to water blockage when flying in highly humid environment, it is highly likely that other pitot tubes would suffer from the same failure, as their failure modes are not independent [3]. It is therefore highly pertinent to estimate airspeed using existing sensors on the vehicle to ultimately identify pitot tube failures.

1.1 Previous Work

Synthetic air data systems or the estimation of airspeed without the use of a pitot tube is a well-explored topic for fixed-wing airliners. Different strategies can be used to fuse measurements from sensors such as Global Navigation Satellite System (GNSS), Inertial Measurement Unit (IMU), angle of attack and side-slip vanes to obtain an estimation of airspeed and wind [1, 4]. Rhudy et al. [5] use measurements from such sensors and wind triangle kinematics equations (see Fig. 2) to derive airspeed and wind estimations for fixed-wing vehicles. As a model-independent estimation method, it can be applied to different vehicles with minimal additional work, but requires angle of attack and side-slip measurements.

When such measurements are not available, a model of the fixed wing vehicle can be used to derive airspeed. Youn et al. [6] explored the use of the z -axis accelerometer and knowledge of the wing's and elevator's C_L curve to estimate airspeed. For hybrid vehicles such as the Variable Skew Quad Plane (VSQP), which transitions from hover flight to forward flight, relying solely on such a strategy is not feasible. Airspeed needs to be known during the transition, before lift starts being generated by the wing. Hansen and Blanke [7] used a similar approach on the drag axis, linking propeller rotational speed to an airspeed estimation, with the vehicle's drag coefficient being known.

Because of its hybrid nature, the VSQP's airspeed estimation also needs to be assessed in the hover flight portion of its mission. A simple strategy for airspeed estimation for multirotors links the vehicle's inclination angle to the airspeed using wind tunnel data assuming a constant drag coefficient [8]. Hattenberger, Bronz, and Condomines [9] show that rotor drag is the main contributor to drag forces on a multirotor and is linear to airspeed. A constant or varying estimation of

rotor drag [10] can be used to estimate airspeed, knowing that the only forces acting on the multicopter come from the rotors' thrust, drag or gravity. However, the assumptions used for these methods do not hold for hybrid vehicles that present additional actuators that can generate forward thrust, a varying drag coefficient and a fuselage that, at higher airspeed, might generate more drag than the rotors themselves.

The direct applicability of fixed-wing and multirotor synthetic air data methods to hybrid vehicles is limited. Therefore, the main goal of this work is to obtain a synthetic air data system capable of accurately estimating airspeed throughout the VSQP's flight envelope using existing sensors such as GNSS and IMU. With an accurate estimation of airspeed, pitot tube faults can be detected and effectively addressed. Although this research focuses on the application of synthetic airspeed estimation for the VSQP platform, it can be applied after some modifications to hybrid vehicles with a similar quad-plane configuration.

1.2 Novelties

This work provides an Extended Kalman Filter (EKF) with model-independent state equations based on kinematics, augmented with a 3 body axes simplified model of the vehicle. The covariance of measurements is scheduled according to the flight phase, taking advantage of the axis providing the most accurate airspeed estimation. Although it is not the main objective of this research, a simple pitot tube fault detection is achieved using a residual based thresholding method. The main contributions of this work are: 1) reliable airspeed estimation in the whole flight envelope of a hybrid vehicle, 2) a model of the VSQP with sufficient fidelity to estimate airspeed depending on the flight phase and 3) pitot tube fault detection on actual flight test data with a failure. To the best of the author's knowledge, this is the first synthetic air data system designed for a hybrid vehicle such as the VSQP.

The structure of this work is as follows. First, the VSQP vehicle is described in Sec. 2. The airspeed estimation model-independent kinematics equations are presented in Sec. 3. Sec. 4 covers modelling the forces acting on the vehicle for the model-dependent airspeed estimation. The EKF implementation is discussed in Sec. 5. The strategy to protect the filter against sensor faults and to detect pitot tube failures is explained in Sec. 6. Experiment's results are discussed in Sec. 7.

2 THE VARIABLE SKEW QUAD PLANE

The VSQP was designed by the TU Delft's Micro Air Vehicle Laboratory (MAVLab) as a derivative of the well-known quad-plane platform. In hover flight, the VSQP operates as a normal quadrotor, powered by two motors fixed to its fuselage and by two motors arranged perpendicular to the wing, as shown in Fig. 1a. The wing is positioned over the fuselage to minimize susceptibility to wind gusts and reduce the landing footprint. The wing-motor assembly can be rotated 90° around its z axis to transition from hover (defined as



(a) VSQP at $\Lambda = 0^\circ$, in quad-mode configuration, with the propellers' rotation conventions used.

(b) VSQP at $\Lambda = 45^\circ$, in transition

(c) VSQP at $\Lambda = 90^\circ$, in forward flight configuration, with axes definitions used.

Figure 1: Different skew angle on the VSQP Prototype. In quad-mode configuration 1a, the wing is placed over the fuselage and hover motors are extended. In forward flight configuration 1c, the wing is completely extended and hover motors are stowed in the fuselage for reduced drag.

$\Lambda = 0^\circ$) to forward flight (defined as $\Lambda = 90^\circ$), as shown in Fig. 1c. Drag is reduced by retracting the hover motors inside the fuselage. In forward flight, thrust is produced by a pusher motor while control is achieved using normal aerodynamic flight controls on the wing and tail. The vehicle is equipped with a pitot tube, GNSS receiver and IMU for obtaining state measurements.

Due to its variable skew wing, the VSQP possesses certain characteristics in common with the oblique flying wing, a manned aircraft concept where the whole wing is skewed around its center axis. Lift, drag, side force generated by the wing all become function of the skew angle [11]. Thus, modelling the vehicle and designing a conventional flight controller based on axis decoupling pose significant challenges.

An Incremental Nonlinear Dynamic Inversion Control (INDI) controller was developed by Van Wijngaarden and Remes [12] and De Ponti [13] for both the stabilization inner loop and guidance outer loop for the VSQP. It requires limited model knowledge, at the expense of increased sensor dependency. The vehicle's nonlinear dynamics can be inverted using the control effectiveness of actuators u on the vehicle's state dynamics $f(x, u)$ to obtain a linear system, easily controllable using classical control methods. Control effectiveness can be obtained analytically or using a least square estimation with flight test data [14, 15]. It is defined as:

$$\frac{\partial f(x, u)}{\partial u} \Big|_{\substack{x=x_0 \\ u=u_0}}. \quad (1)$$

The inner loop's control effectiveness of the aerodynamic control surfaces (ailers, elevator and rudder) and the outer loop's control effectiveness of the wing are both dependent on airspeed as these actuators are lifting surfaces. Additionally, to perform transition, the wing is skewed according to a schedule that aims to minimize power consumption and maximizes overall control effectiveness [13]. The result is an optimal wing skew angle for the current airspeed. Loss of airspeed data following a pitot tube failure leads to incorrect control effectiveness for the inner and outer loops and an in-

correct wing skew position. If sustained, the fault can lead to the vehicle's loss of stability.

3 MODEL-INDEPENDENT AIRSPEED ESTIMATION

GNSS measurements can provide precise ground speed v_{gnd} information. Airspeed v_a can be derived using the wind triangle, knowing the wind v_w . The wind triangle is visualized in Fig. 2 and is expressed in vector form as:

$$v_{gnd}^{\text{NED}} = v_a^{\text{NED}} + v_w^{\text{NED}}. \quad (2)$$

Note that ^{NED} and ^b indicate earth fixed axes and body axes coordinate frames, respectively. The axes used in this work are defined in Fig. 1c. Side slip angle β is defined as the angle between the aircraft airspeed v_a and its plane of symmetry. The direction cosine matrix $\text{DCM}(\phi, \theta, \psi)$ is used to transfer from body to earth fixed frame using the vehicle's Euler angles to obtain Eq. 3.

$$\begin{bmatrix} V_x^{\text{NED}} \\ V_y^{\text{NED}} \\ V_z^{\text{NED}} \end{bmatrix} = \text{DCM}(\phi, \theta, \psi) \begin{bmatrix} u \\ v \\ w \end{bmatrix} + \begin{bmatrix} \mu_x \\ \mu_y \\ \mu_z \end{bmatrix}, \quad (3)$$

where μ is the wind velocity in NED frame.

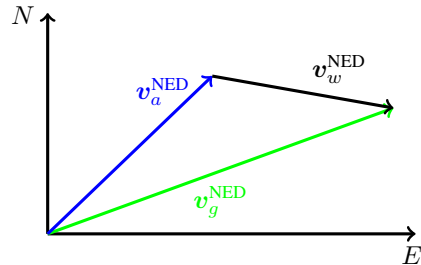


Figure 2: Wind triangle between airspeed, ground speed and wind speed. Airspeed can be derived from a subtraction between ground speed and wind speed.

In most cases, wind is not known and must be estimated simultaneously with airspeed. An EKF can be used to esti-

mate the airspeed by assuming slow changing wind magnitude and direction [5].

The state dynamics for the body axes velocities are expressed using kinematics equations to obtain:

$$\begin{bmatrix} \dot{u} \\ \dot{v} \\ \dot{w} \end{bmatrix} = - \left(\begin{bmatrix} p \\ q \\ r \end{bmatrix} + \mathbf{w}^\omega \right) \times \begin{bmatrix} u \\ v \\ w \end{bmatrix} + \mathbf{DCM}(\phi, \theta, \psi)^T \begin{bmatrix} 0 \\ 0 \\ g \end{bmatrix} + \begin{bmatrix} a_x \\ a_y \\ a_z \end{bmatrix} + \mathbf{w}^a. \quad (4)$$

The kinematics equations themselves present no process noise. Angular rate noise \mathbf{w}^ω and acceleration noise \mathbf{w}^a are added as zero mean Gaussian process noise. Acceleration and angular rates are assumed to be bias free as they are obtained from an independent attitude and position EKF removing bias.

Wind is modelled as a random walk process, as Rhudy et al. [16] showed it to lead to lower airspeed error standard deviation compared to a Gauss-Markov wind model. The wind state dynamics are modelled with zero mean Gaussian process noise \mathbf{w}^μ :

$$\begin{bmatrix} \dot{\mu}_x \\ \dot{\mu}_y \\ \dot{\mu}_z \end{bmatrix} = \mathbf{w}^\mu. \quad (5)$$

The original implementation of this model-independent airspeed method by Rhudy et al. [5] requires angle of attack and side-slip vane measurements. As the VSQP is not equipped with them, they are replaced by model-dependent airspeed estimation using the vehicle's accelerations. These additional measurements serve a dual purpose, as they also help accelerate wind estimation convergence when the vehicle is not moving relative to the ground or is moving in a straight line. They provide an additional airspeed estimation source.

Indeed, to converge on a valid wind estimation using the model-independent method, the vehicle must perform turns, to change the orientation of wind in relation to the vehicle's ground track.

4 MODEL-AIDED AIRSPEED ESTIMATION

Specific forces acting on the vehicle can be derived from the different body axes accelerations. The vehicle is modelled by separating it in different components that generate forces: fuselage, hover propellers, wing, ailerons, pusher propeller, elevator and rudder. Ailerons, elevator and rudder are assumed to generate forces that are negligible compared to other components or average to zero on a long horizon. As such, the measured acceleration relates to the sum of forces from the fuselage, hover motors, wing and pusher motor.

$$a_i = \frac{F_i}{m} = \frac{1}{m} (F_{i_f} + F_{i_h} + F_{i_w} + F_{i_p}) \quad (6)$$

with i being the x , y or z body axes and f , h , w , p being the fuselage, hover motor, wing and pusher motor, respectively.

4.1 Fuselage

Drag is modelled as:

$$D = \frac{1}{2} \rho V_a^2 S C_d. \quad (7)$$

The fuselage is assumed to have a constant drag coefficient and to generate negligible lift. By grouping constant parameters, the force generated by the fuselage is defined as proportional to u squared:

$$F_{x_f} = K_{x_f} u^2. \quad (8)$$

The side force is estimated by assuming that part of the fuselage's drag force D_f is projected on the y body axis when side-slip angle β is present [17]:

$$\sin \beta = \frac{-F_{y_f}}{D_f}. \quad (9)$$

Using a small angle approximation on β , substituting Eq. 7 into Eq. 9 and combining constant parameters, the side force generated by the fuselage can be written as:

$$F_{y_f} = K_{y_f \beta} \beta V_a^2. \quad (10)$$

4.2 Pusher Propeller

Standard definitions for propellers aerodynamic coefficient define a propeller's thrust coefficient C_T :

$$C_T = \frac{T}{\rho \omega^2 d^4}. \quad (11)$$

Test data shows that the thrust coefficient is proportional to the advance ratio $J = \frac{V}{\omega d}$ [18]:

$$C_T = a J + b, \quad (12)$$

where a and b are coefficients experimentally found, ω is the propeller's rotational speed, d is its diameter and V the flow speed parallel to the propeller's axis of rotation.

Isolating thrust in Eq. 11 and substituting the thrust coefficient from Eq. 12, the thrust can be modelled:

$$T = \rho d^3 a \omega V + b \rho \omega^2 d^4. \quad (13)$$

An additional term proportional to airspeed ($K_{x_{p3}}$) is added to better fit wind-tunnel data. It modifies the RPM at which the propeller starts generating thrust depending on airspeed.

For the pusher propeller, the propeller parallel flow V corresponds to body velocity u . Grouping all constant parameters, thrust generated by a propeller is obtained:

$$T_{x_p} = K_{x_{p1}} \omega_p^2 + K_{x_{p2}} \omega_p u + K_{x_{p3}} u. \quad (14)$$

4.3 Hover Propellers

The Hover propellers are modelled in a similar way to the pusher propeller. Flow perpendicular to the propeller's axis of rotation can increase thrust given a constant rotational speed [19]. As the hover motors are to be used mainly in low-speed hover flight, this effect is assumed to be negligible. Parallel flow V is also assumed to be 0, as the vehicle's climb speed in quad mode is generally low. These assumptions lead to another derivative of Eq. 13, where the average hover propeller rotational speed ω_h is used:

$$T_{z_h} = K_{z_h} \omega_h^2. \quad (15)$$

In cross flow, hover propellers mostly generate drag due to a linear difference in local airspeed for the advancing and retreating blade of a rotor. Rotor drag is known to be proportional to the product of rotor RPM and airspeed [20]. Assuming RPM to be constant in hover, hover motors can be modelled as generating drag linear to the incoming airflow [9, 21]:

$$F_{x_h} = K_{x_h} u \quad (16)$$

$$F_{y_h} = K_{y_h} v. \quad (17)$$

4.4 Wing

Classical lift and drag forces are defined as perpendicular to the airflow on the wing. At non-zero angles of attack, part of the lift and drag are projected in the x and z body axes:

$$F_x = L \sin \alpha - D \cos \alpha \quad (18)$$

$$F_z = -L \cos \alpha - D \sin \alpha. \quad (19)$$

Eq. 18 and 19 can be further expanded by developing the lift and drag equations. Lift is modelled in its usual form

$$L = \frac{1}{2} \rho V_a^2 S C_L. \quad (20)$$

The lift coefficient can be assumed to change linearly with the angle of attack

$$C_L = C_{L_0} \alpha + C_{L_0}. \quad (21)$$

with C_{L_0} being the lift coefficient value at 0° angle of attack.

Additionally, assuming constant air density ρ and wing surface S , and substituting Eq. 21 into Eq. 20, constant terms can be grouped together to lead to a formulation of lift as a function of the angle of attack multiplied by airspeed squared:

$$L = (K_{L_0} + K_{L_1} \alpha) V^2. \quad (22)$$

A similar strategy can be used with drag as well. The drag coefficient can be modelled with the simple parabolic drag polar:

$$C_d = C_{d_0} + \frac{C_L^2}{\pi AR e}. \quad (23)$$

The aspect ratio AR and Oswald efficiency e are assumed to be constant. Substituting Eq. 21 into Eq. 23 and grouping all common constants, a second order polynomial multiplied by airspeed squared is obtained:

$$D = (K_{D_0} + K_{D_1} \alpha + K_{D_2} \alpha^2) V^2. \quad (24)$$

Using the small angle approximation on Eq. 18 and 19, substituting in Eq. 24 and 22 and removing third order terms as they are of small magnitude compared to first and second order terms, a formulation of forces in the x and z axis due to lift and drag is obtained:

$$F_x = (K_{x_0} + K_{x_1} \alpha + K_{x_2} \alpha^2) V^2 \quad (25)$$

$$F_z = (K_{z_0} + K_{z_1} \alpha + K_{z_2} \alpha^2) V^2. \quad (26)$$

Lift for the skewed wing is assumed to be derived from the chordwise airspeed V_n component of airspeed V_a [13]:

$$V_n = V_a \sin \Lambda, \quad (27)$$

where Λ is the skew angle.

When fully retracted, the wing can still generate some lift and drag, captured by the addition of a constant term ($K_{x_{w3}}$). It follows that force in the x and z body axes can be modelled as a function of airspeed, skew angle and angle of attack:

$$F_x = (K_{x_{w0}} + K_{x_{w1}} \alpha + K_{x_{w2}} \alpha^2) (\sin \Lambda^2 + K_{x_{w3}}) V_a^2 \quad (28)$$

$$F_z = (K_{z_{w0}} + K_{z_{w1}} \alpha + K_{z_{w2}} \alpha^2) (\sin \Lambda^2 + K_{z_{w3}}) V_a^2. \quad (29)$$

The wing generates a side force when it is skewed as some of its resultant aerodynamic force is projected in the y body axis. As such, it is expected that side force will be a function of skew angle, angle of attack and airspeed. To simplify the model, the side force is modelled at a singular angle of attack that should be representative of the vehicle's angle of attack during transition. As transition occurs rapidly in 4–5 s, this model offset error should have limited impact on the airspeed estimation. Wind tunnel testing lead to an empiric relationship between side force, skew angle and x -body axis airspeed:

$$F_y = (K_{y_w} \sin \Lambda \cos \Lambda^2) V_a^2. \quad (30)$$

A model of side force based on the physical phenomena of lift and drag was attempted but lead to model offset when validated with wind tunnel data. Refer to Appendix A for additional information.

The coefficients for the all the previous models are obtained with wind tunnel experimentation and adjusted slightly with flight test results. Appendix A reviews the wind tunnel data validation campaign completed.

4.5 Model-Dependent EKF Formulation

With the whole aircraft model developed, the measurement equations for the EKF can be written as the sum of the forces generated by each vehicle's component on each body axis:

$$a_{x_{meas}} = \frac{1}{m}(F_{x_f} + F_{x_w} + F_{x_h} + T_{x_p}) \quad (31)$$

$$a_{y_{meas}} = \frac{1}{m}(F_{y_f} + F_{y_w} + F_{y_h}) \quad (32)$$

$$a_{z_{meas}} = \frac{1}{m}(F_{z_w} + T_{z_h}). \quad (33)$$

5 EXTENDED KALMAN FILTER FOR AIRSPEED ESTIMATION

The states \mathbf{x} , inputs \mathbf{u} and measurement \mathbf{z} are defined:

$$\mathbf{x} = [u \ v \ w \ \mu_x \ \mu_y \ \mu_z]^T \quad (34)$$

$$\mathbf{u} = [a_x \ a_y \ a_z \ p \ q \ r \ \phi \ \theta \ \psi \ \omega_p \ \omega_h \ \Lambda]^T \quad (35)$$

$$\mathbf{z} = [V_x^{\text{NED}} \ V_y^{\text{NED}} \ V_z^{\text{NED}} \ a_{x_{meas}} \ a_{y_{meas}} \ a_{z_{meas}}]^T. \quad (36)$$

A classical EKF formulation is used and detailed in Appendix B. All measurements are pre-filtered using a second order Butterworth filter with a cutoff frequency chosen empirically to 5 Hz, to reduce acceleration noise for the model-based component of the filter, at the expense of a slight time-delay. To ensure that lag is not introduced between measurements and inputs, all inputs are filtered with the same cutoff frequency.

5.1 Process Noise

The derived kinematic equations (Fig. 4) themselves do not present process noise, however, they use inputs that do. For each sensor, its variance is calculated when the vehicle is at rest and used to populate the process noise matrix

$$\mathbf{Q} = \text{diag}([\sigma_{a_x}^2 \ \sigma_{a_y}^2 \ \sigma_{a_z}^2 \ \sigma_p^2 \ \sigma_q^2 \ \sigma_r^2 \ \sigma_{\mu_x}^2 \ \sigma_{\mu_y}^2 \ \sigma_{\mu_z}^2]). \quad (37)$$

The resulting numerical values are enumerated in Tab. 1.

The vertical wind μ_z covariance is set arbitrarily to a value 10 times smaller than the horizontal winds μ_x and μ_y , as vertical wind is assumed to be close to zero and with limited gusts.

The optimal covariance to model the wind dynamics is obtained by minimizing the Root Mean Square Error (RMSE) between the filter's airspeed estimation and the airspeed measured by a pitot tube installed onboard. For the six flights presented in Tab. 4, wind covariance is cycled through values ranging from 1×10^{-8} to 1×10^{-2} leading to Fig. 3.

RMSE is minimized for a wind covariance within 1×10^{-6} to $2 \times 10^{-4} \text{ m}^2 \text{s}^{-2}$. A high value of $1.25 \times 10^{-4} \text{ m}^2 \text{s}^{-2}$ within the range was chosen to allow the wind estimation to adapt fast enough for gusts, but not to adjust excessively to measurement errors and lead to a wrong wind estimation.

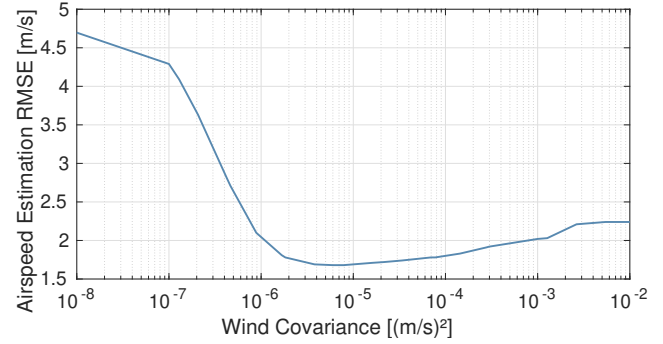


Figure 3: Wind covariance tuning by minimizing airspeed estimation RMSE.

\mathbf{Q}		\mathbf{R}	
$\sigma_{a_x}^2 (\text{m/s}^2)^2$	1.2×10^{-4}	$\sigma_{V_x}^2 (\text{m/s})^2$	4.1×10^{-5}
$\sigma_{a_y}^2 (\text{m/s}^2)^2$	6.2×10^{-4}	$\sigma_{V_y}^2 (\text{m/s})^2$	4.2×10^{-5}
$\sigma_{a_z}^2 (\text{m/s}^2)^2$	3.0×10^{-4}	$\sigma_{V_z}^2 (\text{m/s})^2$	1.4×10^{-4}
$\sigma_p^2 (\text{rad/s})^2$	3.1×10^{-9}	$\sigma_{a_{x_{meas}}}^2 (\text{m/s}^2)^2$	5×10^{-5}
$\sigma_q^2 (\text{rad/s})^2$	1.2×10^{-9}	$\sigma_{a_{y_{meas}}}^2 (\text{m/s}^2)^2$	1×10^{-4}
$\sigma_r^2 (\text{rad/s})^2$	1.3×10^{-9}	$\sigma_{a_{z_{meas}}}^2 (\text{m/s}^2)^2$	5×10^{-4}
$\sigma_{\mu_x}^2 (\text{m/s})^2$	1.25×10^{-4}		
$\sigma_{\mu_y}^2 (\text{m/s})^2$	1.25×10^{-4}		
$\sigma_{\mu_z}^2 (\text{m/s})^2$	1.25×10^{-5}		

Table 1: Covariance assumptions for process and measurement noise of EKF filter. Sensor noise was obtained by measuring variance with the vehicle at rest.

5.2 Measurement Noise

The measurement noise is defined as:

$$\mathbf{R} = \text{diag}([\sigma_{V_x}^2 \ \sigma_{V_y}^2 \ \sigma_{V_z}^2 \ \sigma_{a_{x_{meas}}}^2 \ \sigma_{a_{y_{meas}}}^2 \ \sigma_{a_{z_{meas}}}^2]). \quad (38)$$

It is assumed to be zero mean and Gaussian. For GNSS velocities, the measurement noise is the sensor noise. The acceleration measurement noise $a_{i_{meas}}$ contains the addition of sensor noise and modelling noise. It is assumed to be zero mean and Gaussian. It is hand tuned to provide good filter performance.

5.3 Initial Conditions

The EKF's initialization occurs once the aircraft has taken off. This precautionary measure ensures that the filter is not running while on the ground. Ground-generated forces, which are not accounted for in the model, could result in inaccurate wind estimates. As body velocities and wind speed are unknown at initialization, they are set to 0, as are the offsets. The initial covariance matrix is set to the identity matrix, except for the wind states, which are set to their process noise \mathbf{Q} value.

5.4 Covariance Modifications

As wind is initially set to zero, some time is required to allow the estimated wind to converge to its steady state value.

Ideally, in this phase, one would like the wind estimation to change rapidly with measurement updates. To accelerate convergence of the wind estimation, the wind process noise is multiplied by 100 for the first 20 s of flight. This was tuned empirically to allow for quick convergence.

The z axis acceleration model only provides airspeed information once the wing starts producing lift. Therefore, its covariance is increased when the skew angle is smaller than 60° so as to not rely on it in this phase. A gain multiplier K_{a_z} is scheduled between two hand tuned skew angle set points:

$$K_{a_z} = \begin{cases} 10^2, & \text{if } \Lambda \leq 60^\circ \\ 10^{(\frac{-2(\Lambda-60)}{60-70})}, & \text{if } 60^\circ < \Lambda < 70^\circ \\ 10^0, & \text{Otherwise.} \end{cases} \quad (39)$$

The gain is multiplied with the existing accelerator measurements covariance. This scheduling allows a smooth transition into using the z axis during a transition.

6 FAULT TOLERANCE AND DETECTION

The airspeed estimation will be used to detect pitot tube and EKF's sensor failures using a simple thresholding method.

6.1 Pitot Tube Fault Detection

Two types of pitot tube faults are to be detected: incipient and abrupt, modelled as ramp and step response, respectively.

The pitot tube's measurement is compared to the EKF's airspeed estimation to obtain the pitot tube's residual r . To identify a fault, a thresholding operation is performed on the residual's low-pass filtered signal using two criteria:

$$1. |r| \geq Z_{norm} \text{ for } T_{norm}$$

$$2. \left| \frac{dr}{dt} \right| \geq Z_{deriv} \text{ for } T_{deriv},$$

with Z being a threshold and T a threshold time condition.

The thresholds and time conditions must be selected as a compromise between rapid failure detection and limiting false detections. A threshold set too low will not allow fault detection while a threshold set too high will lead to false detections. Estimating the likelihood of positive detection is more challenging and will be evaluated experimentally.

A statistical approach is used to select thresholds and timing values to reach a desired false detection rate. Assuming non-correlated signals, the probability p_{seq} of the absolute value of a signal sequence to be higher than a threshold Z for a set time T is derived:

$$p_{seq} = p_{single}^{f_{EKF} T}, \quad (40)$$

where f_{EKF} being the frequency of the filter and p_{single} the probability of the signal's absolute value being higher than the threshold for a single occurrence.

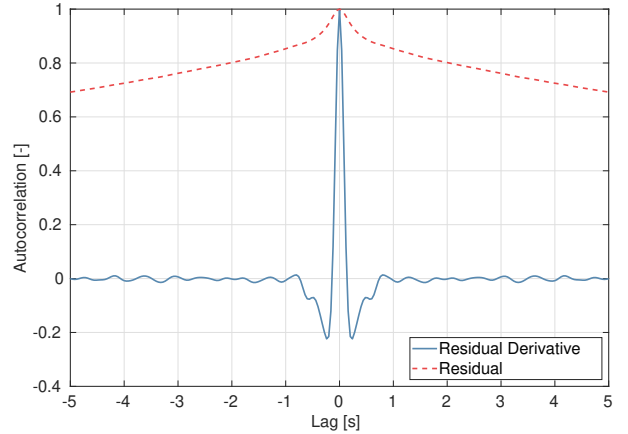


Figure 4: Autocorrelation for the pitot tube residual and residual's derivative, using airspeed estimation results for 23 test flights (over 2 hours of flight time).

The false detection's probability for a set flight time can be calculated knowing the flight's duration T_{flight} :

$$p_{flight} = 1 - (1 - p_{seq})^{T_{flight} f_{EKF}}. \quad (41)$$

An arbitrary rate of $< 0.1\%$ false detection rate per flight hour is used to select thresholds. It is shown through experimentation to lead to fast fault detection, but could be modified depending on the vehicle's required fault detection time and the operator's tolerance to false detections hindering flight operations.

Indeed, a false detection would result in disregarding a healthy sensor, using an alternate airspeed estimation and landing as soon as possible as airspeed measurements would no longer be redundant.

The residuals for 23 flights were compiled to compute the pitot tube's residuals distribution and autocorrelation. As shown in Fig. 4, autocorrelation for the derivative is minimal and allows Eq. 41 to be used. The residual's derivative distribution is shown in Fig. 5. The area under the curve is used to compute the residual's probability of exceeding a certain threshold.

The pitot tube's residual autocorrelation is significantly higher than its derivative, hypothesized to be a result of the wind estimation slowly changing and increasing the likelihood of the residual being correlated to last values. A false detection probability cannot be calculated statistically using the above method due to the higher autocorrelation. Thresholds are hand-tuned to ensure that false detection does not occur during flights.

The selected thresholds are presented in Tab. 2. The time thresholds for the residual's derivative are low, as fast changes in residual need to be detected rapidly as they are indications of an abrupt pitot tube failure. To ensure a low false detection rate, derivatives' threshold values are high.

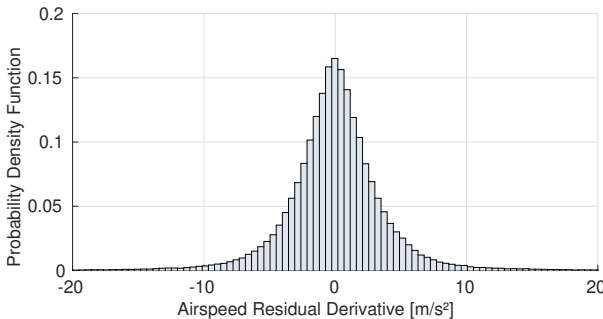


Figure 5: Distribution of the pitot tube’s residual derivative. The histogram is used to estimate false detection rate.

The pitot tube residual threshold value is high, as the residuals can occasionally reach such high values during normal operation at the start of flight when the wind estimation has not fully converged. Pitot tube fault detection could be inhibited during that phase of flight, but this would limit the detection capabilities when the pitot tube is first used near the ground.

Component	Threshold Value	Time Threshold [s]	Cutoff Frequency [Hz]	False Detection Probability [% per flight hour]
Pitot Tube Res.	5.5 m s^{-1}	0.25	5	-
Pitot Tube Res. Derivative	25 m s^{-2}	0.12	5	4×10^{-2}
V_x^{NED} Innov.	2.5 m s^{-1}	0.08	5	7×10^{-2}
V_y^{NED} Innov. Derivative	30 m s^{-2}	0.08	5	2×10^{-3}
$a_{x_{\text{meas}}}$ Innov.	1.25 m s^{-2}	2	0.1	$< 1 \times 10^{-6}$
$a_{x_{\text{meas}}}$ Innov. Derivative	250 m s^{-3}	0.12	0.1	5×10^{-5}

Table 2: Thresholds selected for pitot tube detection and sensor fault detection using statistical analysis.

6.2 EKF Fault Tolerance

If a sensor feeding the estimation system fails without being detected, the precision of the estimation diminishes. The drop in precision might be attributed to a pitot tube failure while the failure may lie within the filter itself. It is crucial to detect sensor faults before the pitot tube fault detector can attribute them to a pitot tube fault.

First, we consider the accelerations, Euler angles and angular rates to be fault free, as they are estimated by a state estimation filter that can be made triple redundant¹. The Eu-

¹Refer to PX4’s EKF:
https://docs.px4.io/main/en/advanced/config/tuning/the_ecl_ekf.html

ler angles are used to convert ground speed measurements from the NED frame to the body frame (see Eq. 3). Without them, no ground speed measurement could be used for the state update. Additionally, the accelerations, Euler angles and angular rates are used directly in the state update equations (refer to Fig. 4). Their absence would render the state prediction and the whole EKF inoperative.

Measurement innovation is defined as the difference between the EKF’s expected measurement value and its actual measurement value. Various sensor failures will have effects on different innovation values, as derived in Tab. 3. This table was built by identifying where each sensor is used in the model-dependent and independent equations.

Impact Innovation	Failure Type	Pitot	GNSS	Skew Sensor	RPM Hover	RPM Push
Pitot	X					
V_x^{NED}		X				
V_y^{NED}		X				
V_z^{NED}		X				
$a_{x_{\text{meas}}}$			X			X
$a_{y_{\text{meas}}}$			X	X		
$a_{z_{\text{meas}}}$			X	X		

Table 3: Innovation impact depending on failure. Table can be interpreted as such: if a failure occurs on a specific sensor (column), it will impact specific innovation values (rows).

A similar strategy as for the pitot tube fault detection is used, with one detector for each EKF’s measurement innovation. Once a fault is detected, the filter does not update the state with the measurement and increases its covariance to represent the measurement’s faulty state.

Thresholds are selected using a similar strategy used for the pitot tube fault detection and are presented in Tab. 2. For the acceleration, the innovation needs to be aggressively filtered. Noise makes it challenging to distinguish small innovation changes due to sensor fault from the background noise. For this work, only thresholds for the x axis innovation acceleration were implemented, but a similar approach can be used for the other axes.

7 RESULTS AND DISCUSSION

This section details the experiments and results used to determine the airspeed estimation precision of the newly developed EKF and its usability to detect pitot tube and sensor faults.

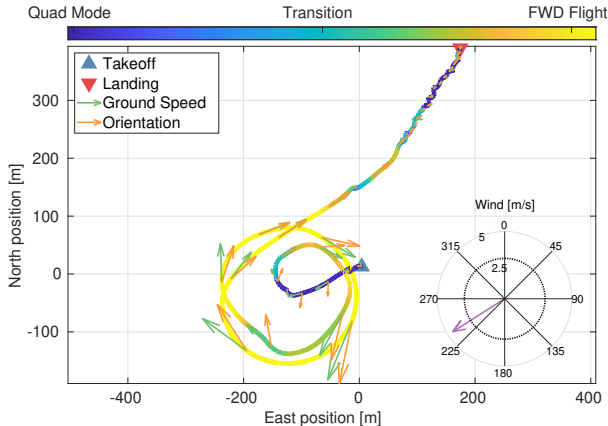


Figure 6: Flight 1 trajectory, with the skew angle shown as line colour. Note the different takeoff and landing points, as the aircraft was launched from a moving ship.

7.1 Airspeed Estimation

Six test flights with the VSQP were selected to demonstrate the filter’s precision in different flight phases and wind conditions, as enumerated in Tab. 4. Flight 1’s flight trajectory is shown in Fig. 6 as an example of a typical transition flight.

The different measurements and inputs required for the EKF filter are logged during each flight. The filter is ran offline at 25 Hz from raw logged data. The filter’s airspeed estimation is compared to the pitot tube’s measured airspeed to obtain the error ΔV and subsequent RMSE over the different flight modes. The comparison is completed when the estimated angle of attack and side-slip are within $\pm 25^\circ$, the typical range where pitot tube readings are not sensitive to flow angles [22]. The quantitative results for each flight are summarized in Tab. 5.

A C++ onboard implementation of the filter was also coded on the open source autopilot paparazzi UAV² for future use in flight. Performance tests on the PX4 Cube Orange main computing board³ demonstrated that the filter only requires approx. 140 μ s per cycle, leaving ample time for other autopilot processes.

7.1.1 Overall Results

The average RMSE between airspeed estimation and pitot tube readings for all flights is 1.62 m s^{-1} , with an average error of -0.49 m s^{-1} . Using a completely model-independent EKF, Rhudy et al. [5] obtained a better overall average error of 0.22 m s^{-1} , albeit by using angle of attack and side-slip vanes. For a model-dependent method based on the lift coefficient, Youn et al. [6] obtain a slightly higher 1.89 m s^{-1} RMSE. Considering our method is not using additional angle

of attack or side slip sensors, it provides airspeed estimation results comparable to the model-dependent and independent method on which it was based. Contrary to the two methods cited, our strategy is able to estimate airspeed in all flight phases of the vehicle.

The RMSE in quad mode is on average twice as for forward flight RMSE. The increased error in quad mode can be attributed to three different factors. First, there is generally less movement to estimate wind and airspeed using the ground speed measurement. The filter has to rely on the acceleration model-dependent airspeed estimation. Additionally, propeller-induced vibrations introduce increased noise levels during hover. This creates challenges for extracting the necessary acceleration signal for accurate airspeed estimation. Finally, the accuracy of pitot tubes generally decreases with airspeed [23]. As it is used as a reference, in low speed hover flight, its reduced precision could increase the hover flight RMSE.

In forward flight, the estimation error is reduced compared to quad mode. Ground speed, x and z acceleration measurements can be used to estimate the airspeed, providing higher precision. Additionally, acceleration noise is reduced, providing easier airspeed estimation from acceleration measurements.

In transition, the higher RMSE compared to forward flight can in part be attributed to the changing wing dynamics in transition and possible imprecision of the wing model when skewed. In flight 4, which was flown with a sustained wing skew, the RMSE is increased, as is the average error ΔV . Again, this points to some model uncertainty that offsets the airspeed estimate. For example, the wing model could be overestimating the lift at a set skew angle, leading to a lower airspeed to be propagated in the filter.

Flight	Flight Type	Average Wind Speed [m s^{-1}]	Flight Duration		
			Total [s]	Quad Mode [s]	Forward Flight [s]
1	Transition	4.6	352	169	79
2	Transition	5.7	241	140	92
3	Transition	5.3	310	155	139
4	Wing Skewed 30-60 degrees	9.1	227	164	0
5	Hover Flight	7.6	307	307	0
6	Pitot Tube Failure	7.0	338	249	0

Table 4: Flight selection for testing the EKF filter, with different flight types and wind speeds.

7.1.2 Closer Examination of a Single Flight

Flight 3 shows higher error values than other flights due to various factors. It warrants a closer examination in Fig. 7. The vehicle takes off in quad mode ($\Lambda = 0^\circ$). As the vehicle

²<https://github.com/paparazzi/>

³<https://ardupilot.org/copter/docs/common-thecubeorange-overview.html>

Flight		RMS ΔV [m s $^{-1}$]			
	Full Flight	Quad Mode	Transition	Forward Flight	average(ΔV) [m s $^{-1}$]
1	1.25	1.70	1.14	0.91	-0.14
2	1.42	2.06	1.80	0.75	-0.82
3	2.03	2.58	1.40	1.29	1.12
4	1.91	2.04	1.56	-	-1.34
5	1.50	1.62	-	-	-0.75
6	1.64	1.73	-	-	-0.99
Average	1.62	1.95	1.47	0.98	-0.49

Table 5: Airspeed error for selected flights, comparing between EKF’s estimation and pitot tube measurements. Transition is defined as a skew angle between 30–80°. RMSE is smallest in forward flight and biggest in quad mode.

took off, the wind covariance is increased, leading to the wind estimation to quickly converge in about 10 s to its steady state value.

At $t = 350$ s, the vehicle starts its transition to forward flight, with the airspeed estimation closely following the pitot tube measurement. Once in forward flight ($\Lambda = 90^\circ$), the aircraft travels in circles with the airspeed estimation oscillating slightly, at the same period as the wind estimation. This is due to a slight side-slip angle offset varying throughout the circle that is not captured by the filter, generating an oscillating wind estimation to compensate. This increases the forward flight RMSE slightly compared to other flights.

At $t = 545$ s, the drone comes back to its landing pad and descends slowly. An offset between pitot tube and airspeed estimation builds up starting from $t = 550$ s. This is assumed to be due to the reduction in wind velocity close to the ground, as the landing pad is sheltered from the wind. The filter’s wind estimation magnitude does decrease slowly, but not rapidly enough, contributing to the increased hover airspeed estimation error.

7.2 Pitot Tube Fault Detection

7.2.1 Abrupt Fault

The ability of the thresholding method to detect abrupt pitot tube faults was validated using real flight test data where a fault was present. An abrupt pitot tube fault occurred during flight 6 at $t \approx 311.9$ s, as shown in Fig. 8. The fault is first detected by the derivative criterion in 0.16 s and later by the normal criterion. The derivative criterion detected the fault earlier than the normal residual criterion, as the abrupt fault is characterized by a rapidly changing airspeed measurement. Such a quick detection time should allow sufficient time for the autopilot to switch to the synthetic airspeed estimation before loss of stability.

Both the normal and derivative criteria detection time are longer than their time threshold (0.25 and 0.12 s respectively) due to the delay induced by filtering the residual. Increasing the low pass filter’s cutoff frequency would reduce the delay,

but would require a higher threshold to guarantee the same low false detection rate.

7.2.2 Incipient Fault

The incipient fault is simulated on flight 2 as a negative ramp with a -2.5 m s $^{-2}$ rate, simulating a water blockage [1]. Fig. 9 shows a detection only occurring after 2.5 s, resulting in an approx. 7 m s $^{-1}$ airspeed error. The long detection time is due to the high 6 m s $^{-1}$ residual threshold required before starting to recognize the behaviour as a possible fault.

This is a limitation of the thresholding method. A lower threshold could be used, but would lead to false detections at the start of the flight, where the wind is converging to its real value. Other methods that examine the statistical mean and variance of the signal such as generalized likelihood tests [24] can be explored to reduce detection time. These come at the expense of additional computing power, as a statistical model needs to be fitted to the residual signal in real time to see if this model changes over time.

7.3 EKF Fault Tolerance

To validate the EKF’s ability to tolerate sensor faults and to detect them in time, simulated sensor faults were inserted in flight 2’s logged data.

7.3.1 GNSS Fault

A GNSS failure is simulated in forward flight, by setting the measurement to 0. Fig. 10 shows detection by the derivative criterion in 0.12 s, at which point the Global Positioning System (GPS) ground speed measurement is no longer used to update the states. As a result, the wind estimation stops being updated and stays constant. The acceleration measurements directly update the body velocities of the vehicle.

The fault results in a 2 m s $^{-1}$ drop in estimated airspeed which would not trigger the pitot tube fault detector. The airspeed estimation increases back to its normal value after the fault. Precision after the fault is reduced from 1.55 to 2.23 m s $^{-1}$, due to the reduced number of measurements used to update the airspeed.

7.3.2 Pusher RPM Sensor Fault

A pusher RPM sensor failure is simulated by setting the measured RPM to 0 in forward flight, when it would normally be around 8000 RPM. With RPM at 0 and at a high airspeed, the filter assumes that the aircraft should be slowing down, updating the airspeed estimation down. Fig. 11 shows a 4.3 s detection time that leads to a 2 m s $^{-1}$ drop in estimated airspeed similar to the GNSS fault.

Airspeed estimation is maintained. As with the GNSS fault, the loss of a measurement leads to a drop in airspeed precision, from 1.55 to 2.33 m s $^{-1}$. It is shown that the filter can tolerate and detect sensor faults. Once a fault is detected, it is recommended to land as the airspeed estimation’s precision is reduced and cannot guarantee accurate pitot tube fault detection using the thresholds defined for the fault-free sensor condition.

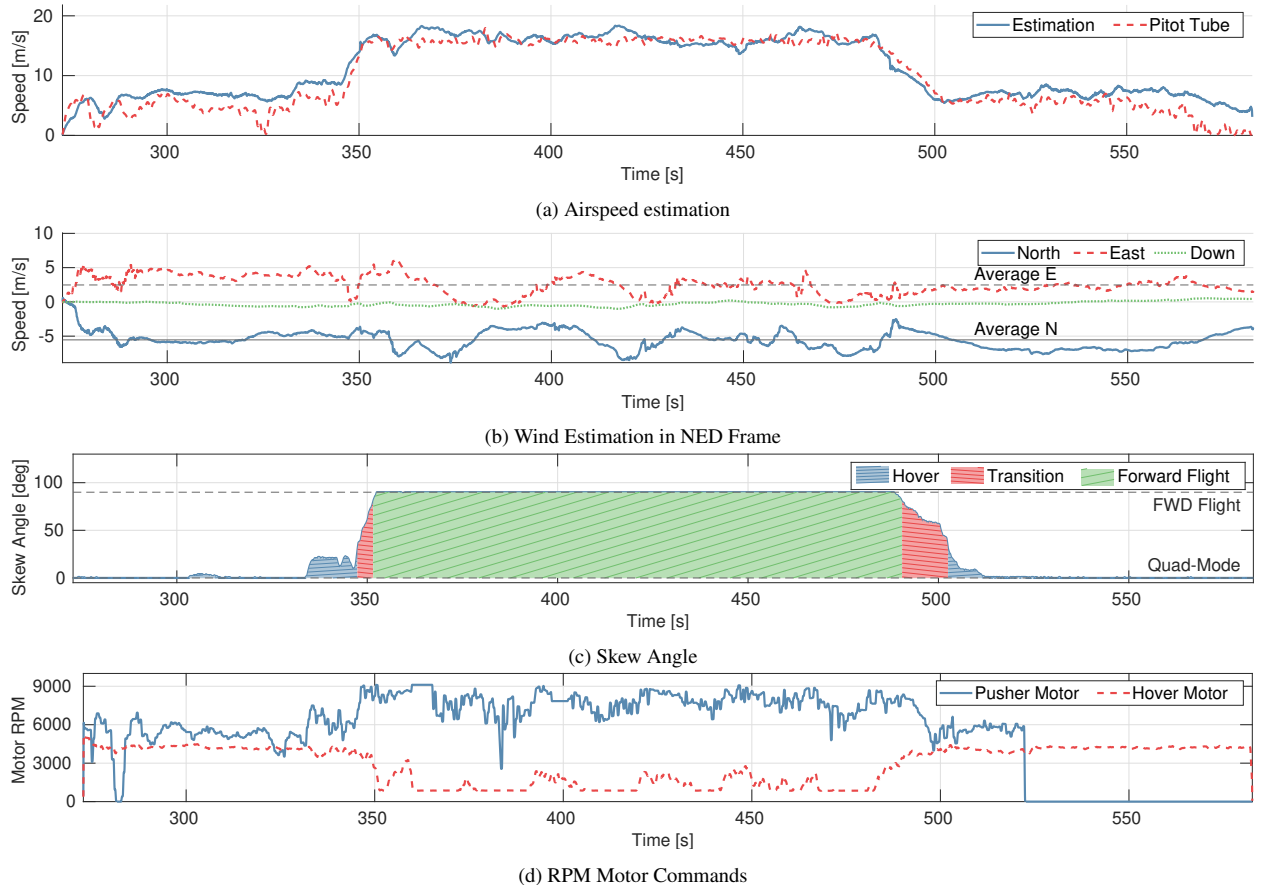


Figure 7: Flight 3 with full transition from quad to forward flight mode at $t = 350$ s. Overall 2.03 m s^{-1} RMSE, hover RMSE 2.58 m s^{-1} , transition 1.40 m s^{-1} RMSE, forward flight 1.29 m s^{-1} RMSE

7.4 Application to Other Vehicles

To validate that the filter can be applied to hybrid vehicles of a similar configuration with minimal work, the filter was tested on an older VSQP prototype, flying in TU Delft’s Open Jet Facility (OJF) wind tunnel [13]. Compared to a normal flight where the vehicle is moving and wind is varying slowly, in the wind tunnel tests, the vehicle is trying to keep its position constant while incoming wind is changed. The wind covariance was increased to model these changes. The sensor covariance was adjusted to fit the sensors installed on the older prototype. The prototype’s force model coefficients were identified using flight test data in different configurations. As RPM feedback from the motors was not available, the Pulse Width Modulation (PWM) control signal is used to estimate motor RPM.

Fig. 12 shows three transitions. The overall 1.66 m s^{-1} RMSE is comparable to results with the newest VSQP. Airspeed estimation oscillations can be observed during transition, which seems to be derived from the pusher motor oscillating. In forward flight, the RMSE is low, due to the constant magnitude and gust-free airflow of the wind tunnel.

Overall, the precise airspeed estimation obtained on an older prototype show that the filter can be used on other platforms having a similar configuration. Instead of using wind tunnel data to obtain the coefficients necessary to model the forces, flight test data can be used to empirically estimate them.

8 CONCLUSION

The intent of this work was to develop a synthetic air data system for the Variable Skew Quad Plane (VSQP) hybrid vehicle in order to detect pitot tube failures. An Extended Kalman Filter (EKF) based on kinematic equations using GNSS and inertial measurements was developed. It is augmented using a simplified model of the vehicle and acceleration measurements. Validation on six different test flights lead to an average airspeed Root Mean Square Error (RMSE) of 1.62 m s^{-1} and an average airspeed error of -0.49 m s^{-1} . Precision is maximal in forward flight, when all measurements can be used to estimate airspeed and the rotor induced acceleration noise is minimal. The airspeed estimation was able to detect a real-life abrupt pitot tube fault in 0.16 s using

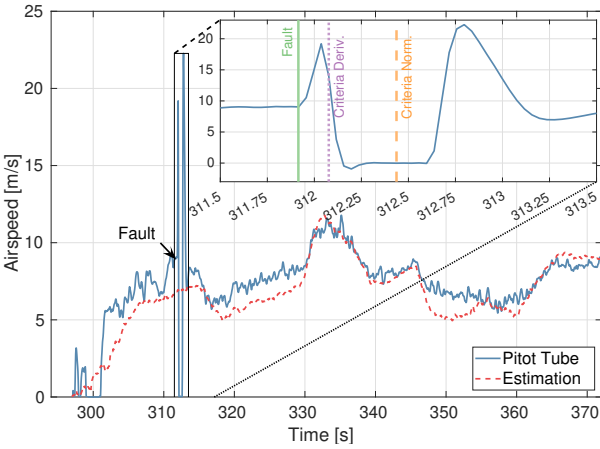


Figure 8: Abrupt pitot failure in flight 6 at $t \approx 311.9$ s. Fault is detected in 0.16 s by the derivative criterion and by the normal criterion 0.36 s later.

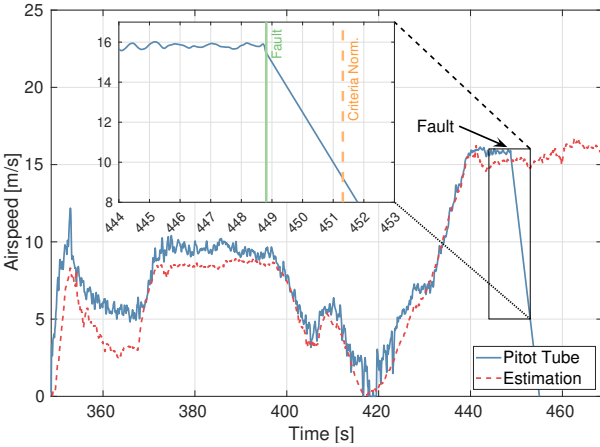


Figure 9: Simulated incipient pitot tube fault at $t = 448.8$ s during flight 2. Detection is achieved in 2.5 s by the normal residual criterion.

a simple residual thresholding method. A similar approach was shown to provide fault tolerance to the filter, ensuring that sensor faults do not lead to a wrong airspeed estimation and to false pitot tube failure detection. One of the biggest benefits of the developed EKF filter is its ability to estimate airspeed for the whole flight envelope of the hybrid vehicle using conventional GNSS and inertial sensors, without the use of angle of attack or side slip vanes.

8.1 Recommendations

Additional work should examine how to improve the force models to reduce the average airspeed estimation error. To guide this research, the author recommends to analyze the effect of each model component (fuselage, wing, pusher propeller, hover propeller) on the precision of the airspeed estimation. Such a sensitivity analysis would contribute to

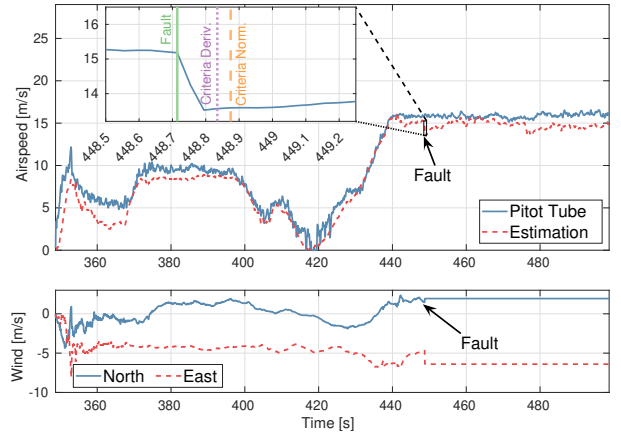


Figure 10: Simulated GNSS Failure at $t = 448$ s during flight 2. Detection is achieved in 0.12 s, leading to a 2 m s^{-1} airspeed estimation drop.

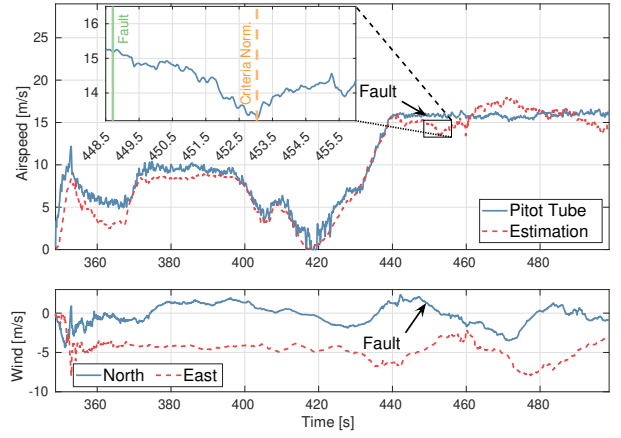


Figure 11: Simulated pusher RPM sensor failure at $t = 448$ s during flight 2. Detection is achieved in 4.3 s and leads to a 2 m s^{-1} airspeed estimation drop.

a better understanding of the robustness of model-dependent airspeed estimation in relation to variations in vehicle characteristics.

The airspeed estimation filter was initially developed as to be completely independent from the pitot tube. Integration of the pitot tube as a measurement into the filter should be considered, for which faults are monitored on each measurement's innovation. Such a system would improve the airspeed estimation during fault-free flight and group the airspeed estimation and fault detection functions in a single, easier to implement package on the vehicle.

Alternative detection methods based on statistical signal analysis should also be explored. They could provide a shorter detection time that be less affected by the measurement noise. These could identify the change in mean or standard deviation that occurs on innovation after a fault, while being more robust to noise. This would directly improve the

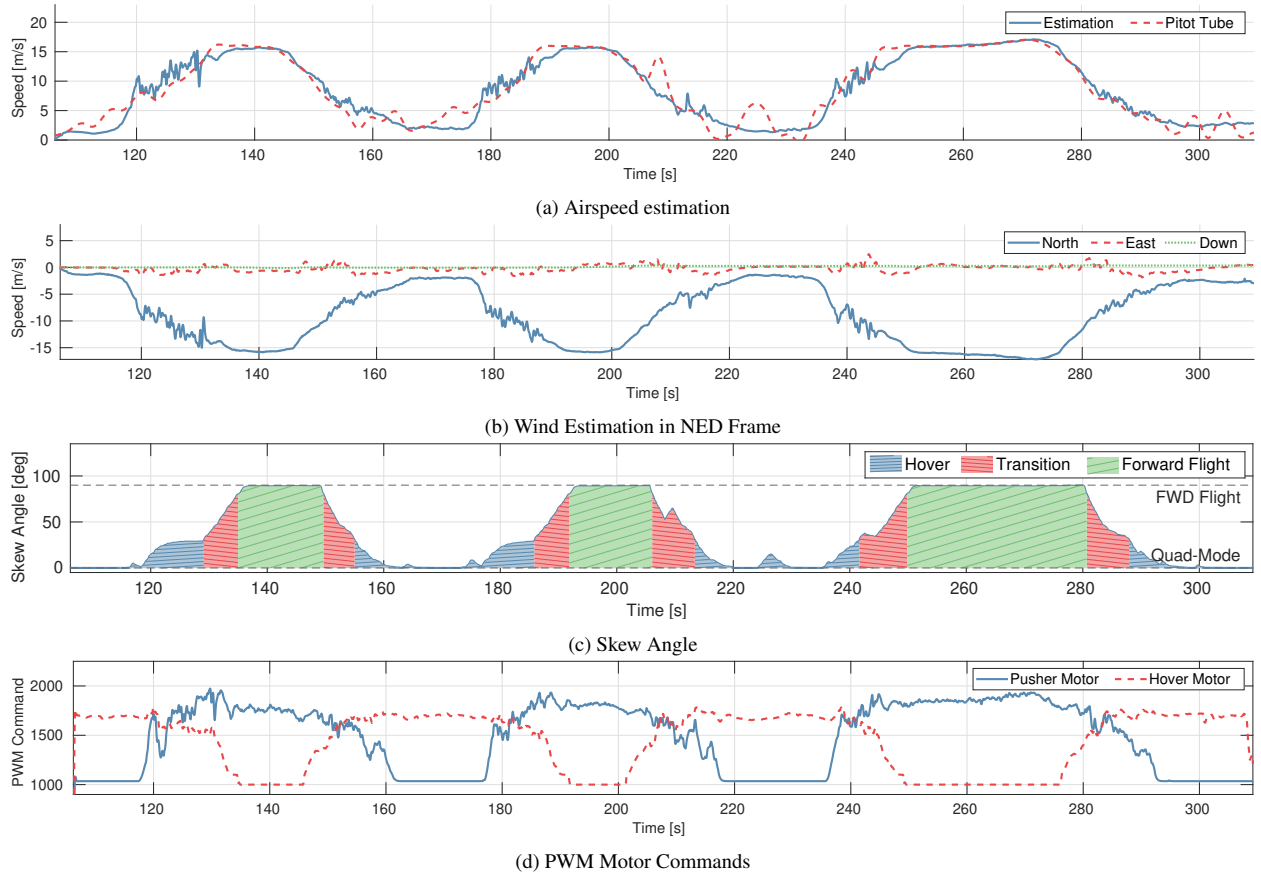


Figure 12: Airspeed estimation during wind tunnel flights with the older VSQP prototype. Wind is increased and decreased while the model tries to hold its position. Overall 1.66 m s^{-1} RMSE, hover 1.92 m s^{-1} RMSE, Transition 2.06 m s^{-1} RMSE, forward flight 0.40 m s^{-1} RMSE. Note that North is defined as pointing towards the wind tunnel and airflow.

detection time for the incipient fault. Although they might require increased computing power, they could potentially offer better and more robust fault protection.

Finally, if the filter's airspeed estimation is to be ultimately used for control of the vehicle, further research should go into characterizing and understanding the interaction between the estimation and control aspects. For example, pusher RPM oscillations have been seen to lead to airspeed estimation oscillations. These should be contained as to not lead to control oscillations, that could be amplified by the estimation process, leading to instability.

REFERENCES

- [1] Kerry Sun and Demoz Gebre-Egziabher. “Air data fault detection and isolation for small UAS using integrity monitoring framework”. In: *Institute of Navigation* 68.3 (2021), pp. 577–600. DOI: 10.1002/navi.440.
- [2] R.P.G Collinson. *Introduction to Avionics Systems*. 3rd. New York: Springer, 2011, pp. 217–230.
- [3] John Downton. *When failure is an option : redundancy, reliability and regulation in complex technical systems*. London: Centre for Analysis of Risk, Regulation at the London School of Economics, and Political Science, 2009, p. 24. ISBN: 9780853283959.
- [4] Omar Hazbon Alvarez. “Fault Tolerant Air Data System for Pitot Tube Failure”. PhD thesis. Medellin: Universidad Pontificia Bolivariana, 2020.
- [5] Matthew B. Rhudy et al. “Aircraft model-independent airspeed estimation without pitot tube measurements”. In: *IEEE Transactions on Aerospace and Electronic Systems* 51.3 (July 2015), pp. 1980–1995. ISSN: 00189251. DOI: 10.1109/TAES.2015.130631.
- [6] Wonkeun Youn et al. “Model-Aided Synthetic Airspeed Estimation of UAVs for Analytical Redundancy”. In: *IEEE Robotics and Automation Letters* 6.3 (July 2021), pp. 5841–5848. ISSN: 23773766. DOI: 10.1109/LRA.2021.3086428.
- [7] Søren Hansen and Mogens Blanke. “Diagnosis of Airspeed Measurement Faults for Unmanned Aerial Vehi-

- cles”. In: *IEEE Transactions on Aerospace and Electronic Systems* 50.1 (2014). DOI: 10.1109/TAES.2013.120420.
- [8] Patrick P. Neumann and Matthias Bartholmai. “Real-time wind estimation on a micro unmanned aerial vehicle using its inertial measurement unit”. In: *Sensors and Actuators, A: Physical* 235 (Nov. 2015), pp. 300–310. ISSN: 09244247. DOI: 10.1016/J.SNA.2015.09.036.
- [9] Gautier Hattenberger, Murat Bronz, and Jean Philippe Condomines. “Estimating wind using a quadrotor”. In: *International Journal of Micro Air Vehicles* 14 (Jan. 2022). ISSN: 17568307. DOI: 10.1177/17568293211070824.
- [10] Robert C Leishman et al. “Quadrotors and Accelerometers: State Estimation with an Improved Dynamic Model”. In: *IEEE Control Systems Magazine* 34.1 (2014), pp. 28–41. URL: <https://scholarsarchive.byu.edu/facpub>.
- [11] Michael J. Hirschberg, David M. Hart, and Thomas J. Beutner. “A summary of a half-century of oblique wing research”. In: *Collection of Technical Papers - 45th AIAA Aerospace Sciences Meeting*. Vol. 3. 2007, pp. 1781–1815. ISBN: 1563478900. DOI: 10.2514/6.2007-150.
- [12] D C Van Wijngaarden and B D W Remes. “INDI Control for the Oblique Wing-Quad Plane Drone”. In: *International Micro Air Vehicle Conference*. Delft, 2022, pp. 119–126.
- [13] Tomaso Maria Luigi De Ponti. “Incremental Nonlinear Dynamic Inversion Controller for a Variable Skew Quad Plane”. In: *2023 International Conference on Unmanned Aircraft Systems (ICUAS)*. Warsaw, June 2023, pp. 241–248.
- [14] Christophe Wagter et al. “Modelling of a Hybrid UAV Using Test Flight Data”. In: *International Micro Air Vehicle Conference*. 2014. DOI: <https://doi.org/10.4233/uuid:2eed26cf-a7e8-4a6c-ac42-89a9608e4d2a>.
- [15] Ewoud J. J. Smeur, Murat Bronz, and Guido C. H. E. de Croon. “Incremental Control and Guidance of Hybrid Aircraft Applied to a Tailsitter UAV”. In: *Journal of Guidance, Control, and Dynamics: devoted to the technology of dynamics and control* 43.2 (Feb. 2018). DOI: 10.2514/1.G004520. URL: <http://arxiv.org/abs/1802.00714>.
- [16] Matthew B. Rhudy et al. “Comparison of wind speed models within a Pitot-free airspeed estimation algorithm using light aviation data”. In: *Aerospace Science and Technology* 86 (Mar. 2019), pp. 21–29. ISSN: 12709638. DOI: 10.1016/j.ast.2018.12.028.
- [17] Ewoud J.J. Smeur, Qiping Chu, and Guido C.H.E. De Croon. “Adaptive incremental nonlinear dynamic inversion for attitude control of micro air vehicles”. In: *Journal of Guidance, Control, and Dynamics* 39.3 (2016), pp. 450–461. ISSN: 15333884. DOI: 10.2514/1.G001490.
- [18] John Burton Brandt. *Small Scale Propeller Performance at Low Speed*. Master’s Thesis, 2005.
- [19] Bart Theys et al. “Wind Tunnel Testing of a VTOL MAV Propeller in Tilted Operating Mode”. In: *International Conference on Unmanned Aircraft Systems*. Orlando, 2014. ISBN: 3216328058.
- [20] Yasushi Morikawa and Takeshi Tsuchiya. “H-Force of Rigid Rotor in Forward Flight of Multi-rotor”. In: *International Symposium on Aerospace Technology*. Vol. 912. 2023, pp. 595–606. ISBN: 9789811926884. DOI: 10.1007/978-981-19-2689-1_46.
- [21] Erik Van Baasbank. *Estimating wind fields using drones in a network*. Delft: Master’s Thesis, 2022.
- [22] Robert P Benedict. *Fundamentals of Temperature, Pressure, and Flow Measurements*. Third Edition. Wiley-Interscience, 1984.
- [23] Icaro De Oliveira Buscarini et al. “Impact of Pitot tube calibration on the uncertainty of water flow rate measurement”. In: *Journal of Physics: Conference Series*. Vol. 648. 1. Institute of Physics Publishing, Oct. 2015. DOI: 10.1088/1742-6596/648/1/012005.
- [24] Søren Hansen, Mogens Blanke, and Jens Adrian. “Diagnosis of UAV Pitot Tube Defects Using Statistical Change Detection”. In: *IFAC Proceedings Volumes* 43.16 (Jan. 2010), pp. 485–490. ISSN: 1474-6670. DOI: 10.3182/20100906-3-IT-2019.00084.
- [25] Stephen James Morris. “Integrated Aerodynamic and Control System Design of Oblique Wing Aircraft”. PhD thesis. Stanford, Jan. 1990. URL: <https://ntrs.nasa.gov/search.jsp?R=19930074026>.

APPENDIX A MODEL VALIDATION

The force models presented in Sec. 4 were validated using wind tunnel data obtained at TU Delft’s OJF. The model is set on a pole connected to a 6-component balance measuring forces and moments. The assembly is placed on a turntable to submit the vehicle to different angles of attack or side-slip angles, as shown in Fig. 13.

Different test rounds are completed with the same wind speed, angle of attack, side-slip and actuator commands, but removing components on the vehicle (wing, elevator, hover propellers, pusher propellers). Specific components of the vehicle can be isolated by subtracting test rounds results with the same parameters.

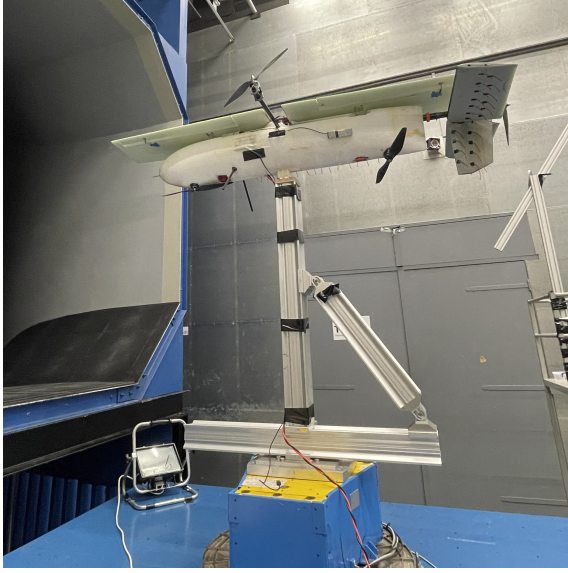


Figure 13: Static test in TU Delft’s OJF wind tunnel. The VSQP is placed on a 6-component balance that is rotated through 360° to subject the vehicle to various angle of attack and side-slip conditions.

The coefficients for the force models can be determined by minimizing the average RMSE between model estimation and wind tunnel data points. Fig. 14 to 17 report the wind tunnel data points and the estimation obtained for the fuselage, hover propeller, wing and pusher propeller.

Fig. 15a shows that a constant drag coefficient with angle of attack can be assumed without sacrificing significant fidelity. A second order fit on the angle of attack leads to a slightly better average 0.3 N RMSE compared to the initial 0.6 N RMSE, but results in a more complex model. Fuselage side force is well modelled as linear to side-slip angle in Fig. 15b, with a small 1.21 N average RMSE in comparison to the ± 50 N range. Assuming a negligible fuselage z axis force, this leads to a low 1.93 N RMSE, relative to the wing or hover motors that produce approx. 60–70 N.

Fig. 16a and 16c show the relationship between angle of attack and wing F_x and F_z forces. To simplify results, force is divided by the airspeed squared. For a skew angle of 0° , the wing generates minimal body x or z axis force. As skew angle is increased, as modelled by Eq. 28 and 29, the wing generates more force. The F_x wing model developed in Eq. 25 is validated by a $3 \times 10^{-3} \text{ N}/(\text{m/s})^2$ RMSE. The F_x force becomes positive when approaching an angle of attack of $2\text{--}3^\circ$, as the lift force is projected forward in the body x -axis and supplants the drag force projection. The F_z wing model developed in Eq. 29 is validated in Fig. 16c with a low $1.7 \times 10^{-2} \text{ N}/(\text{m/s})^2$ RMSE. Validation for both models was limited to an angle of attack ranging from -5 to 15° , which corresponds to the general flight envelope of the vehicle in

forward flight.

Fig. 16b shows an empiric fit linking the side force to the skew angle using trigonometric functions from Eq. 30 with a 0.66 N RMSE for a 6° angle of attack. Side force is underestimated at high skew angles. A fit based on James Morris [25]’s work on oblique wing modelling was also attempted:

$$F_{y_w} = \pm \frac{\cos \Lambda}{\sin \Lambda} \left(\frac{C_L^2}{\pi AR e} + C_L \alpha \right), \quad (42)$$

where the \pm is used to specify the side force sign depending on the skew direction (left or right wing forward).

However, the model in Eq. 42 did not properly capture the peak in side force around $30\text{--}35^\circ$ of skew angle. This might be due to some spanwise flow on the wing modifying the lift behaviour at low skew angles. Ultimately, Eq. 30 was chosen as it better captured the peak side force.

Hover motor drag force as a function of cross-flow is shown in Fig. 17a, for a normal 3800–4100 RPM hover regime. As expected, the plot highlights a linear relation between hover motor drag force and airspeed, with a slope that increases with RPM. An average value of -0.75 N s m^{-1} from the 4000 RPM curve will be used for further work. For the hover motor thrust force F_z , a quadratic fit with RPM is validated in Fig. 17b with an average 2.5 N RMSE. As predicted, cross-flow has no significant effect.

The pusher propeller thrust force as a function of RPM and airspeed is validated in Fig. 14, with a low 0.42 N RMSE relative to the pusher thrust 30 N range. Thrust force is reduced as airspeed is increased as expected by Eq. 14.

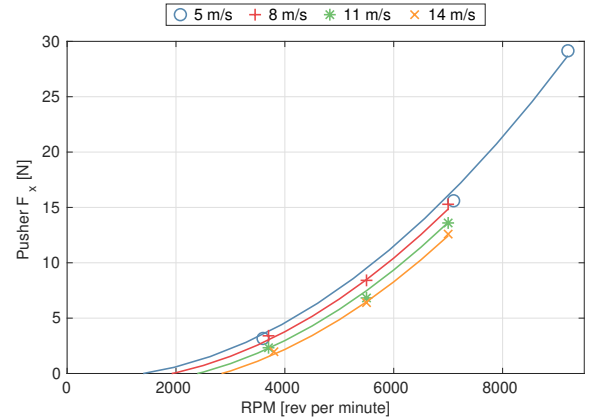
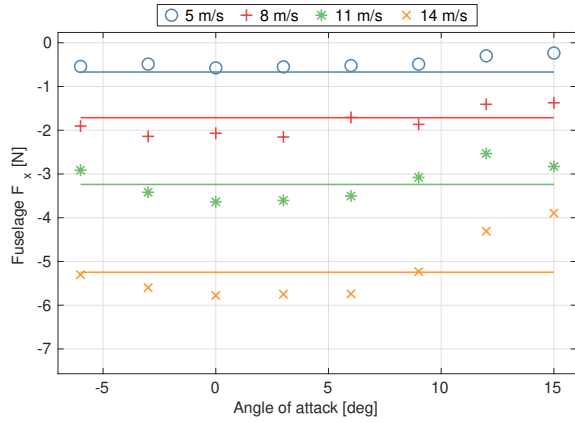
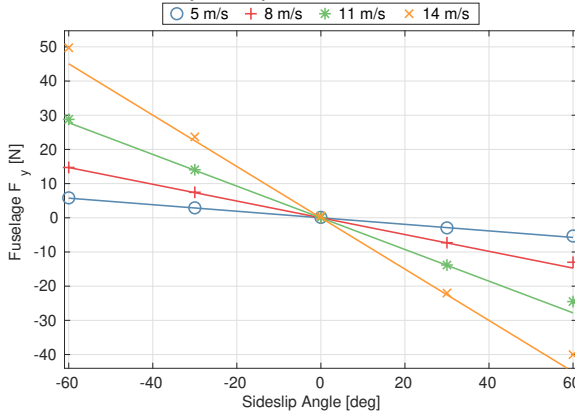


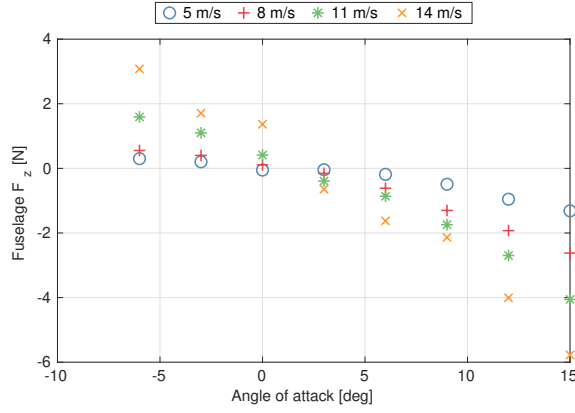
Figure 14: Pusher motor x -axis force fit depending on RPM for different airspeed. Fit shown is $T_{x_p} = K_{x_{p1}} \omega_p^2 + K_{x_{p2}} \omega_p u + K_{z_{p3}} u$, with 0.419 N RMSE.



(a) Linear Fit between fuselage x -axis force and angle of attack for different airspeed. Shown fit is $F_{x_f} = K_{x_f} u^2$, with 0.6 N RMSE.

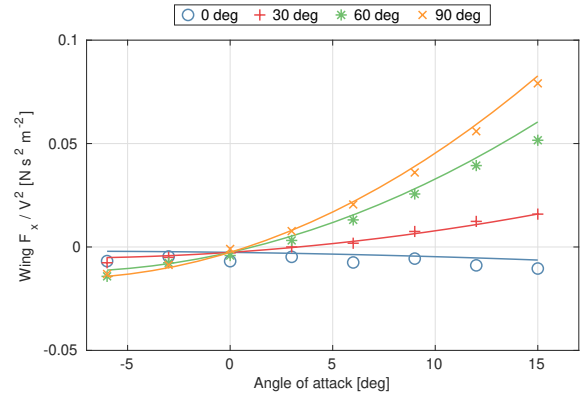


(b) Linear Fit between fuselage y -axis force and side-slip angle for different airspeed. Fit shown is $F_{y_f} = K_{y_f \beta} \beta V_a^2$, with 1.21 N RMSE.

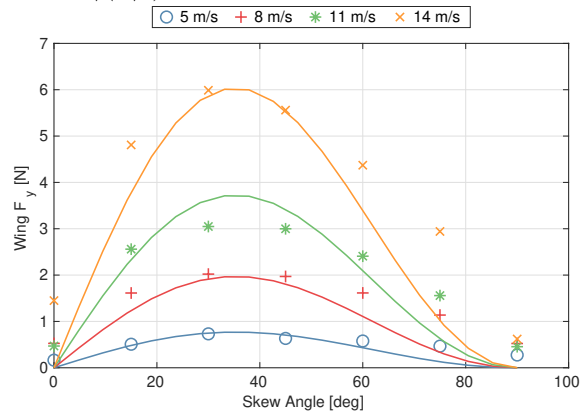


(c) Fuselage z -axis force depending on angle of attack for different airspeed. Fuselage z -axis force was assumed to be negligible, with 1.93 N RMSE.

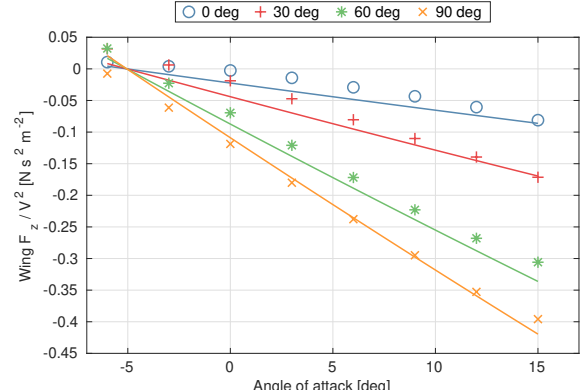
Figure 15: Fuselage fit from wind tunnel testing in OJF



(a) Airspeed scaled wing x -axis force depending on angle of attack for different skew angles. Fit shown is $F_{x_w} / u^2 = (K_{x_w0} + K_{x_w1} \alpha + K_{x_w2} \alpha^2)$, with 0.003 N/(m/s)² RMSE.

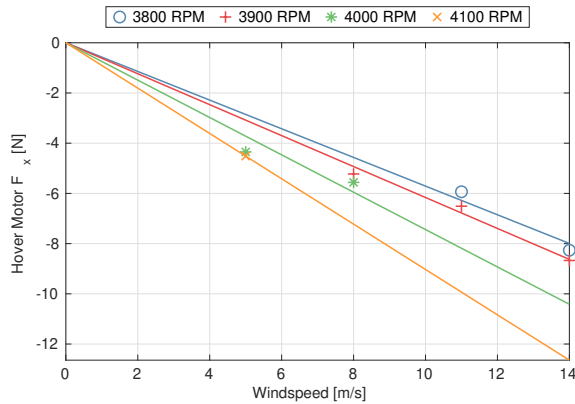


(b) Wing side force (y -axis) depending on skew angle for a fixed angle of attack of 6°. Fit shown is $F_{y_w} = (K_{y_w} \sin \Lambda \cos \Lambda^2) u^2$, with 0.66 N RMSE.

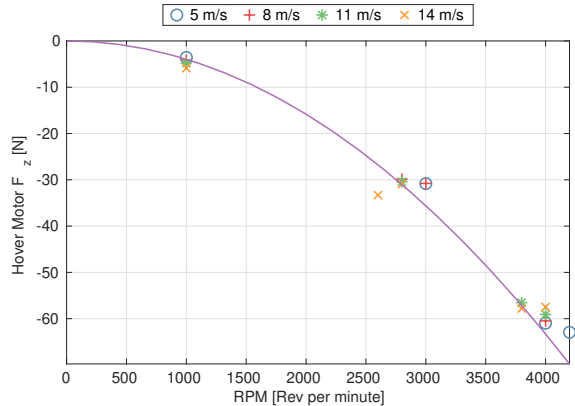


(c) Airspeed scaled wing z -axis force depending on angle of attack for different skew angles. Fit shown is $F_{z_w} / u^2 = (K_{z_w0} + K_{z_w1} \alpha + K_{z_w2} \alpha^2)$, with 0.017 N/(m/s)² RMSE.

Figure 16: Wing fit from wind tunnel testing in OJF



(a) Linear Fit between total hover motor x -axis force and different hover RPM values. Shown fit is $F_{x_h} = K_{x_h} u$, with 1.52 N RMSE.



(b) Quadratic Fit between hover motor z -axis force and RPM for different airspeed. Shown fit is $T_{z_h} = K_{z_h} \omega_h^2$, with 2.53 N RMSE.

Figure 17: Hover motor fit from wind tunnel testing in OJF

APPENDIX B EXTENDED KALMAN FILTER IMPLEMENTATION

State vector \mathbf{x} , input vector \mathbf{u} and measurement vector \mathbf{z} are defined as:

$$\mathbf{x} = [u \ v \ w \ \mu_x \ \mu_y \ \mu_z]^T \quad (43)$$

$$\mathbf{u} = [a_x \ a_y \ a_z \ p \ q \ r \ \phi \ \theta \ \psi \ \omega_p \ \omega_h \ \Lambda]^T \quad (44)$$

$$\mathbf{z} = [V_x^{\text{NED}} \ V_y^{\text{NED}} \ V_z^{\text{NED}} \ a_{x_{\text{meas}}} \ a_{y_{\text{meas}}} \ a_{z_{\text{meas}}}]^T. \quad (45)$$

With state dynamics $f(x, u)$ and measurement output function $g(x, u)$:

$$\dot{x} = f(x, u) \quad (46)$$

$$z = g(x, u). \quad (47)$$

States, output, state noise and measurement noise Jaco-

bians are respectively $F(x, u), G(x, u), L(x, u), M(x, u)$:

$$F(x, u) = \frac{\partial f}{\partial \mathbf{x}} \quad (48)$$

$$L(x, u) = \frac{\partial f}{\partial \mathbf{w}} \quad (49)$$

$$G(x, u) = \frac{\partial g}{\partial \mathbf{x}} \quad (50)$$

$$M(x, u) = \frac{\partial g}{\partial \mathbf{w}}. \quad (51)$$

The main equations of the EKF are as follows. First, state and covariance are predicted:

$$\mathbf{x}_{\text{pred}} = f(x, u) dt \quad (52)$$

$$P_{\text{pred}} = F(x, u) P F_x(u)^T + L(x, u) Q L(x, u)^T. \quad (53)$$

After which innovation and the innovation matrix S are calculated:

$$\mathbf{y} = \mathbf{z} - g(x, u) \quad (54)$$

$$S = G(x, u) P_{\text{pred}} G(x, u)^T + M(x, u) R M(x, u)^T. \quad (55)$$

The Kalman Gain can be calculated and used to update the state \mathbf{x} and covariance P :

$$K = P_{\text{pred}} G(x, u)^T S^{-1} \quad (56)$$

$$\mathbf{x} = \mathbf{x}_{\text{pred}} + K \mathbf{y} \quad (57)$$

$$P = (I - K G(x, u)) P_{\text{pred}}. \quad (58)$$

Part II

Literature Study

Literature Study Contents

3	Introduction	31
4	Literature Study Plan	33
5	Variable Skew Quad Plane	35
5.1	VSQP Distinct Features	35
5.1.1	Issues with the VSQP Prototype.	35
5.1.2	New VSQP version.	35
5.1.3	Comparison to Oblique Wing Aircraft	36
5.2	INDI	38
5.2.1	General Principles	38
5.2.2	INDI for Stabilization and Guidance	39
5.2.3	INDI Advantages	40
6	Fault Tolerant Control Methods	41
6.1	FTC General Principles	41
6.2	Passive FTC	41
6.3	Active FTC	42
6.3.1	Detection	42
6.3.2	Supervision	43
7	Critical Failure Cases	45
7.1	Failure Mode and Effects Analysis.	45
7.1.1	Listing Failure Modes.	45
7.1.2	Severity and Probability of Failure	46
7.2	Selected Critical Failure Cases	46
7.2.1	Rotor Loss	47
7.2.2	Stuck Stabilator.	49
7.2.3	Wing skew angle Sensor Failure	49
7.2.4	Pitot Tube Failure.	50
8	Pitot Tube Failure	53
8.1	Use of Airspeed Data on VSQP	53
8.1.1	Control Effectiveness Estimation	53
8.1.2	Wing Rotation Scheduling	55
8.2	INDI Robustness	55
8.3	Airspeed Estimation	57
8.3.1	Dynamics Based	57
8.3.2	Wind Triangle Based	58
8.3.3	Forces Based	61
8.4	Pitot Tube Fault Detection Methods	61
9	Project Plan	63
9.1	Updated Research Objective	63
9.2	Methodology	63
9.2.1	Modeling and Simulation.	63
9.2.2	Experimentation	64
9.3	Project Planning	64
9.3.1	Limitations	64
9.3.2	Work Packages.	65
10	Conclusion	67

Bibliography	69
Appendices	73
A Failure Mode Analysis	74
B Rotor Loss Initial Calculations	87

List of Figures

1.1	Different skew angle on the VSQP Prototype. In quad-mode configuration 1.1a, the wing is placed over the fuselage and hover motors are extended. In forward flight configuration 1.1c, the wing is completely extended and hover motors are stowed in the fuselage for reduced drag.	2
3.1	Quad Plane Configuration for a Hybrid UAV. Shown is fours hover motors for vertical flight and a forward flight tractor motor.	31
3.2	Rotation of the Wing and Hover Motors on the VSQP Prototype [10]	32
5.1	Downwash induced by rear hover motor	36
5.3	Aerodynamic Characteristics of Oblique Wing due to Asymmetry of Wing	38
5.4	Cascaded version of INDI based on Smeur, Croon, and Chu [18], with position ξ , attitude η (NED), angular rate Ω , thrust T , commanded motor rotation ω_c , system output y	39
6.1	Structure of Active FTC systems (inspired by Abbaspour et al. [24])	42
7.1	Tree Visualization of the Failure Mode and Effect Analysis, with the actuator system branch expanded. H = hover, FF = Forward Flight and the \rightarrow signify a transition from one state to the other	46
7.2	Gimbaled pusher motor with front motor failure	48
7.3	Water Blockage Pitot Tube Failure Mode	50
8.1	Skew Scheduling with Airspeed Using Weights $\gamma_\phi = 2, \gamma_\theta = 3, \gamma_\psi = 1, \gamma_T = 4$ [10]	55
8.2	INDI Stability with control effectiveness uncertainty by Veld, Van Kampen, and Chu [19] using its non-linear Cessna Citation Model with, $F = 2$, $K_u = 13$, $K_x = 7$ and $\gamma = \frac{G}{G+\Delta G}$	56
8.3	Wind Triangle	59
8.4	Dual EKF Architecture with Aircraft Dynamic Model [49]	59
9.1	Gantt Chart of Project Plan for VSQP as of December 15th 2023	66

List of Tables

5.1 Modifications to the VSQP	36
6.1 Summary of different FTC methods	44
7.1 Severity Classification of Failure Modes	46
7.2 Risk Matrix Used to Classify Failure Modes by Criticality	47
7.3 Critical Failure Cases for VSQP	52
8.1 Summary of Airspeed Estimation Methods	58

List of Abbreviations

Abbreviation	Description
CFD	Computational Fluid Dynamics
CG	Center of Gravity
EKF	Extended Kalman Filter
FMEA	Failure Mode and Effects Analysis
FTC	Fault Tolerant Control
GNSS	Global Navigation Satellite System
IMU	Inertial Measurement Unit
INDI	Incremental Nonlinear Dynamic Inversion
LQR	Linear Quadratic Regulator
MAV	Micro Air Vehicle
MAVLab	Micro Air Vehicle Laboratory
MIMO	Multi-Input and Multi-Output
MPC	Model Predictive Control
NDI	Nonlinear Dynamic Inversion
NED	North-East-Down
OJF	Open Jet Facility
PID	Proportional Integral and Derivative
SISO	Single-Input and Single-Output
TWR	Thrust to Weight Ratio
UAV	Unmanned Air Vehicle
VSQP	Variable Skew Quad Plane
VTOL	Vertical Takeoff and Landing
WLS	Weighted Least Square

List of Symbols

Abbreviation	Description	Unit
x_b	Body x-axis	-
y_b	Body y-axis	-
z_b	Body z-axis	-
L	Lift	N
D	Drag	N
T	Thrust	N
W	Weight	N
F	Force	N
C_L	Lift Coefficient	-
C_d	Drag Coefficient	-
g	Gravity	m s^{-2}
m	Mass	kg
L	Roll Moment	N m
M	Pitching Moment	N m
N	Yaw Moment	N m
x	State	-
r	Residual	-
u	Input	-
y	Output	-
A	State State Space Matrix	-
B	Input State Space Matrix	-
v	Virtual Control Input	-
G	Control Effectiveness	-
W	Weighting Matrix	-
w	Weight	-

Abbreviation	Description	Unit
ϕ	Roll angle	rad
θ	Pitch angle	rad
ψ	Yaw angle	rad
α	Angle of Attack	rad
β	Sideslip Angle	rad
η	Attitude Vector	rad
Ω	Angular Rate Vector	rad s^{-1}
Ω	Angular Rate Motor	rad s^{-1}
p	Angular Rate in Body Frame x-axis	rad s^{-1}
q	Angular Rate in Body Frame y-axis	rad s^{-1}
r	Angular Rate in Body Frame z-axis	rad s^{-1}
ξ	Position Vector	m
\vec{v}_g	Ground Velocity Vector	m s^{-1}
\vec{V}_x	Velocity in Earth Fixed Frame x-axis	m s^{-1}
\vec{V}_y	Velocity in Earth Fixed Frame y-axis	m s^{-1}
\vec{V}_z	Velocity in Earth Fixed Frame z-axis	m s^{-1}
\vec{v}_a	Airspeed Vector	m s^{-1}
\vec{v}_w	Wind Velocity Vector	m s^{-1}
a	Acceleration	m s^{-2}
a_x	Acceleration in Body Frame x-axis	m s^{-2}
a_y	Acceleration in Body Frame y-axis	m s^{-2}
a_z	Acceleration in Body Frame z-axis	m s^{-2}
u	Velocity in Body Frame x-axis	m s^{-1}
v	Velocity in Body Frame y-axis	m s^{-1}
w	Velocity in Body Frame z-axis	m s^{-1}
μ_x	Wind Velocity in Earth Fixed Frame x-axis	m s^{-1}
μ_y	Wind Velocity in Earth Fixed Frame y-axis	m s^{-1}
μ_z	Wind Velocity in Earth Fixed Frame z-axis	m s^{-1}
Λ	Skew Angle	rad
k	Gain, Parameter or Coefficient	-
γ	Climb Angle	rad
b	Arm	m
S	Surface, Area	m^2

Abbreviation	Description	Unit
w	Gaussian Process Noise	-
I_v	Inertia Tensor Vehicle	-
I	Inertia Tensor	-
k_t	Thrust Coefficient of Motor	$\text{N s}^2 \text{ rad}^{-2}$
k_q	Torque Coefficient of Motor	N m N^{-1}
δ	Deflection	rad
ρ	Density	kg m^{-3}
λ	Control Effectiveness Uncertainty	-
τ	Time Constant	s^{-1}
τ	Torque	N m

3

Introduction

Unmanned Air Vehicles (UAVs) have seen an increase in use for diverse missions ranging from military, search and rescue, aerial photography, surveillance, to infrastructure inspection and deliveries. They have garnered attention as they can perform tasks autonomously without endangering the operator and can be miniaturized to perform missions where classical manned vehicles could not operate. The ideal UAV would be deployable from confined areas, be able to fly efficiently and rapidly to their area of interest, be integrated with regular air traffic, while being fully autonomous and exhibiting the same reliability as classical manned air vehicles.

Historically, UAVs have been developed as either fixed wing vehicles with efficient cruise characteristics or as rotorcrafts (multicopters, helicopter) with hover capabilities and confined space landing capabilities. Hybrid platforms, a subset of UAV, correspond to vehicles that can fly both in fixed wing and Vertical Takeoff and Landing (VTOL) configurations. They take advantage of efficient wing derived lift and high cruising speed while being able to transition to hover flight for precise VTOL capabilities [5]. A wide variety of hybrid configurations have been explored, as summarized by Saeed et al. [5]: from tail-sitters [6], tilt-rotor [7, 8], tilt-wing [1] and quad-plane [9] vehicles. In the quad-plane configuration (as shown in Figure 3.1), a conventional aircraft configuration is used, on which four vertical rotors are installed to allow hover flight as a quadcopter. In transition, the forward flight motor is started to provide horizontal thrust. Once in forward flight, lift is generated by the wing and the hover motors can be shut down. Some drawbacks arise from the addition of hover motors on the vehicle. In forward flight, the non-operational hover motors create additional drag. In hover, the vertical stabilizer is susceptible to wind gusts, which can only be counteracted using reactionary torque from the propellers. Finally, a quad plane requires a bigger landing space than normal rotorcraft due to its wing size.

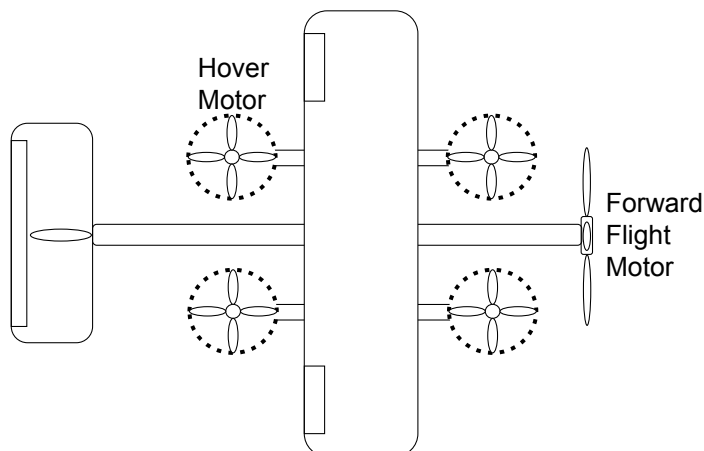


Figure 3.1: Quad Plane Configuration for a Hybrid UAV. Shown is fours hover motors for vertical flight and a forward flight tractor motor.

To minimize these drawbacks, the Variable Skew Quad Plane (VSQP) prototype was designed by the Micro Air Vehicle Laboratory (MAVLab) at the TU Delft. As shown in Figure 3.2, two hover motors are fixed to the fuselage longitudinally and two hover motors are fixed on arms perpendicular to the wing. The wing can be skewed (defined with angle Λ) from 0 degrees in hover to 90 degrees in forward flight. This way, in forward flight, the hover motors are housed in the fuselage for reduced drag. In hover, the wing is in line with the fuselage, reducing its susceptibility to wind gusts and allowing for landing in confined areas. To the best of the author's knowledge, this specific configuration has only been developed by De Ponti [10] and Van Wijngaarden and Remes [11].

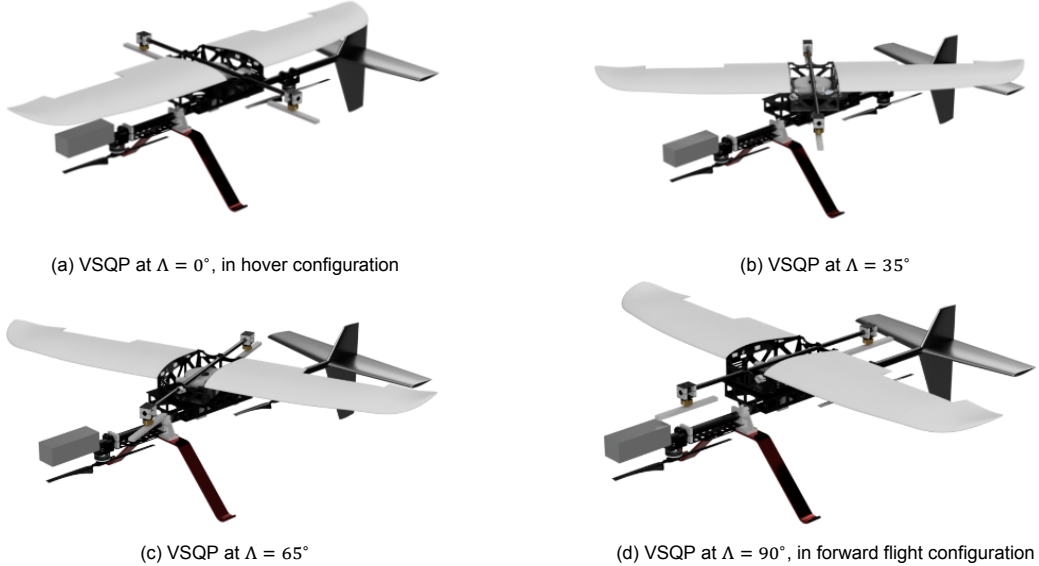


Figure 3.2: Rotation of the Wing and Hover Motors on the VSQP Prototype [10]

Ultimately, this vehicle is to be powered by hydrogen, a very flammable energy source, requiring a high degree of safety during its flight operations [1]. Reliability can be improved by using redundant systems, at the expense of additional weight [12]. Fault Tolerant Control (FTC) is another avenue to improve the reliability of a vehicle by allowing it to fly after a fault occurred, either by being naturally robust (passive FTC) or by readapting the use of its actuators and controller (active FTC). FTC is a software-based method and that at its most basic level does not require additional hardware or mass to be added to the vehicle. With this demand for high reliability and performance throughout the flight of the VSQP, fault-tolerant control is an attractive control method to use. The goal of this work is to improve the safety of the VSQP using fault tolerant control methods.

This report is structured as follows: chapter 4 introduces the research questions that will guide the literature review and the research strategy used to answer them, chapter 5 presents the existing and new VSQP platform, chapter 6 assesses different FTC methods. Chapter 7 provides a Failure Mode and Effects Analysis (FMEA) based on literature to identify the most critical failure modes to be addressed on the VSQP. Chapter 8 provides an overview of topics relevant to the pitot tube failure. The initial project plan used for the thesis is presented in chapter 9. Chapter 10 concludes the review.

4

Literature Study Plan

The initial goal of this thesis research was:

“To achieve and maintain stable flight of the variable skew quad plane after the failure of the most critical component of the vehicle (i.e. most probable failure with most severe effects), using fault tolerant based control methods”

VSQP and Most Critical Failure Mode

The research goal was purposely kept generic as to which component failure should be analyzed and which fault tolerant control method should be used to maintain stable flight. The most critical failure mode must be identified, using knowledge on the VSQP vehicle. The first questions to be addressed by the literature study were defined as:

Q1 What distinctive flight and control features does the VSQP exhibit?

Q1.1 How does the VSQP compares to an oblique wing? Are there any related control challenges?

Q1.2 How was the VSQP prototype stabilized? How was Incremental Nonlinear Dynamic Inversion (INDI) implemented?

Q2 What are the most critical failure modes of the vehicle?

Q2.1 What are the possible failures modes of the VSQP's components?

Q2.2 What failure modes have the highest probability of occurring during flight?

Q2.3 What failure modes have the most severe effects on the ability to maintain stable flight?

Q3 How can fault tolerant methods be used to achieve and maintain stable flight after a failure?

Q3.1 What are the different types of fault tolerant control? What advantages and disadvantages do they present?

Q3.2 How are fault tolerant control methods typically used to maintain stability of UAVs after a fault.

Q1 aims to understand the dynamics of the vehicle and how existing research on this platform allows stable flight. By understanding these dynamics, it will be easier to identify which component and which flight phase are critical to the safe flight of the vehicle. **Q2** is centered around identifying the most critical components of the VSQP by listing the component's failure modes, analyzing their probability and severity. This process is known in the literature as FMEA. **Q3** focuses on the general principles behind FTC, their different classifications and how they can be used to maintain an aircraft in stable flight. This topic will be revisited with specific applications found in the literature for the pitot tube failure in chapter 8.

Evaluation of Most Critical Failure Modes

The four most critical failure modes can be analyzed in further details to assess the solutions provided in the literature and identify potential knowledge gaps. The following research questions were selected for each of the most critical failure modes:

Q4 What solutions are documented in the literature to address these failure modes?

Q5 What challenges or knowledge gaps are present?

Pitot Tube Failure

As will be detailed in chapter 7, the pitot tube failure was selected for further research due to the high probability of water blockage occurrence for small UAVs and VSQP's controller high reliance on airspeed. The effects of an unreliable airspeed on the controller, estimation methods and detection must be analyzed:

Q6 Which methods using conventional sensors can be used to estimate airspeed without a pitot tube, for a hybrid aircraft?

Q7 By what means can the stability of the aircraft be maintained with uncertainty on airspeed?

Q7.1 What is the robustness of the VSQP controller to airspeed uncertainty?

Q7.2 How to adapt the existing INDI controller to allow flight with airspeed uncertainty?

Q8 What methods can be used to detect a pitot tube failure?

Q7 aims to determine the VSQP's controller robustness to uncertainty on airspeed data. Understanding how the airspeed data is integrated in the controller's architecture will help find potential solutions to improve its robustness and will provide an overview of the required precision for the airspeed estimation. Answering **Q6** will give an overview of possible airspeed estimations methods, their precision and the required sensors. Ideally, the estimation method should provide accurate results on the whole vehicle envelope using its existing sensors. **Q7** and **Q6** are highly connected as the achievable airspeed estimation precision will serve as a requirement for the tolerance of the controller to an inexact airspeed. Finally, as a secondary objective of this work, **Q8** will help to select and develop a rudimentary detection method for the pitot tube fault.

To summarize, the questions guiding the literature review cover the identification of the most critical failure modes on the VSQP, possible solutions and existing knowledge gaps. This led to choosing the pitot tube failure as the most critical failure mode to be further investigated. The additional questions related to the pitot tube failure will lead to subsequent steps in this thesis, with simulation and experimentation. Although all the critical failure modes were not explored further, this literature review will hopefully have identified knowledge gaps and other solutions to improve the safety of the VSQP.

5

Variable Skew Quad Plane

This chapter reviews the distinct features of the VSQP platform to identify failure modes. The limitations faced by the VSQP prototype and how they should be addressed in a newer iteration is discussed in subsection 5.1.1 and 5.1.2. Additionally, its similarity to an oblique wing aircraft will be explored in subsection 5.1.3, to understand the control challenges that surround a rotating wing and proposed solutions found in the literature. The general principles behind the INDI controller stabilizing the VSQP will be developed in section 5.2.

5.1. VSQP Distinct Features

As introduced in chapter 3, the VSQP is a hybrid design between a conventional aircraft and a quad copter. It can takeoff using its hover motors with its wing rotated over the fuselage (Figure 3.2a, where $\Lambda = 0^\circ$). With the configuration of a quad copter, all lift and control moments are provided by the rotors. The vehicle can tilt to gain forward airspeed. At this point, the wing can be rotated to start transferring lift force from the rotors to the wing. After full transition, the wing is perpendicular to the airflow (Figure 3.2d, where $\Lambda = 90^\circ$) as in a conventional aircraft configuration. Control surfaces can be used to stabilize and control the aircraft in forward flight. To the best of the author's knowledge, there exists no UAV with the same configuration yet mentioned in the literature.

5.1.1. Issues with the VSQP Prototype

It was found during testing by Van Wijngaarden and Remes [11] and De Ponti [10] that at a speed regime of $7 - 8 \text{ m s}^{-1}$ (corresponding to a skew angle of $30 - 45^\circ$), the elevator and rear hover motor saturate in the pitch down position. It is believed that the hover motor's downwash interfered with the horizontal tail stabilizer, resulting in the horizontal tail stabilizer having a negative angle of attack (see Figure 5.1). Wind Tunnel tests are planned at the Open Jet Facility (OJF)¹ to investigate the interaction between the propeller downwash and the horizontal tail angle of attack. Additionally, the VSQP prototype presented a Thrust to Weight Ratio (TWR) of approx. 1.5 with full batteries and 1.08 at low battery level, leaving little to no thrust available to fight disturbances [10].

5.1.2. New VSQP version

A new VSQP version is being built to overcome the aforementioned issues and increase the total weight of the vehicle. Figure 5.2c shows the latest version. The most important changes are presented in Table 5.1.

By incorporating a stabilator (Figure 5.2a), it is hoped that the horizontal tail can maintain pitch authority even with major airflow changes due to the hover motors. By tilting the hover motors slightly to the side (Figure 5.2b), additional yaw moment can be generated with minimal penalty on the vertical thrust produced. This should improve the ability of the VSQP to counteract lateral disturbances. With a

¹<https://www.tudelft.nl/lr/organisatie/afdelingen/flow-physics-and-technology/facilities/low-speed-wind-tunnels/open-jet-facility>

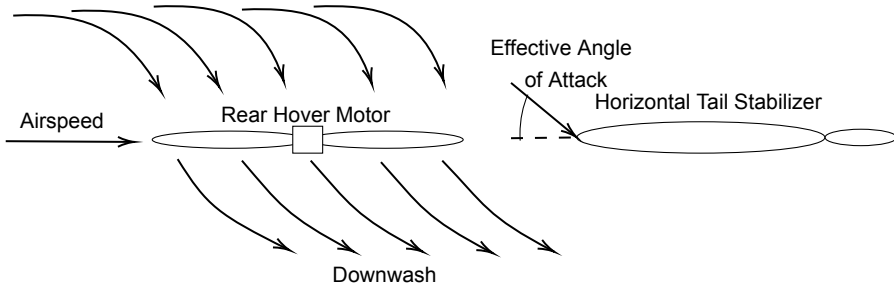


Figure 5.1: Downwash induced by rear hover motor

Modifications	Explanation
Fully movable horizontal tail (stabilator)	Ability to change local angle of attack of the whole stabilizer
Tilted hover motors	Increased yaw authority
Increased TWR (2)	Increased available thrust for control

Table 5.1: Modifications to the VSQP

planned TWR of 2, VSQP will have sufficient excess thrust available to stabilize the aircraft.

5.1.3. Comparison to Oblique Wing Aircraft

The variable skewing wing of the VSQP closely resemble the mechanism used on oblique wing aircraft. Contrary to the oblique wing aircraft that improves its performance at high Mach number by reducing the effective airspeed on the wing [13], the VSQP aims to reduce its landing footprint and susceptibility to wind gusts with its wing stowed over its fuselage [11]. Nevertheless, some of the distinct control and dynamic characteristics of the oblique wing are shared with the VSQP when transitioning.

Inertia

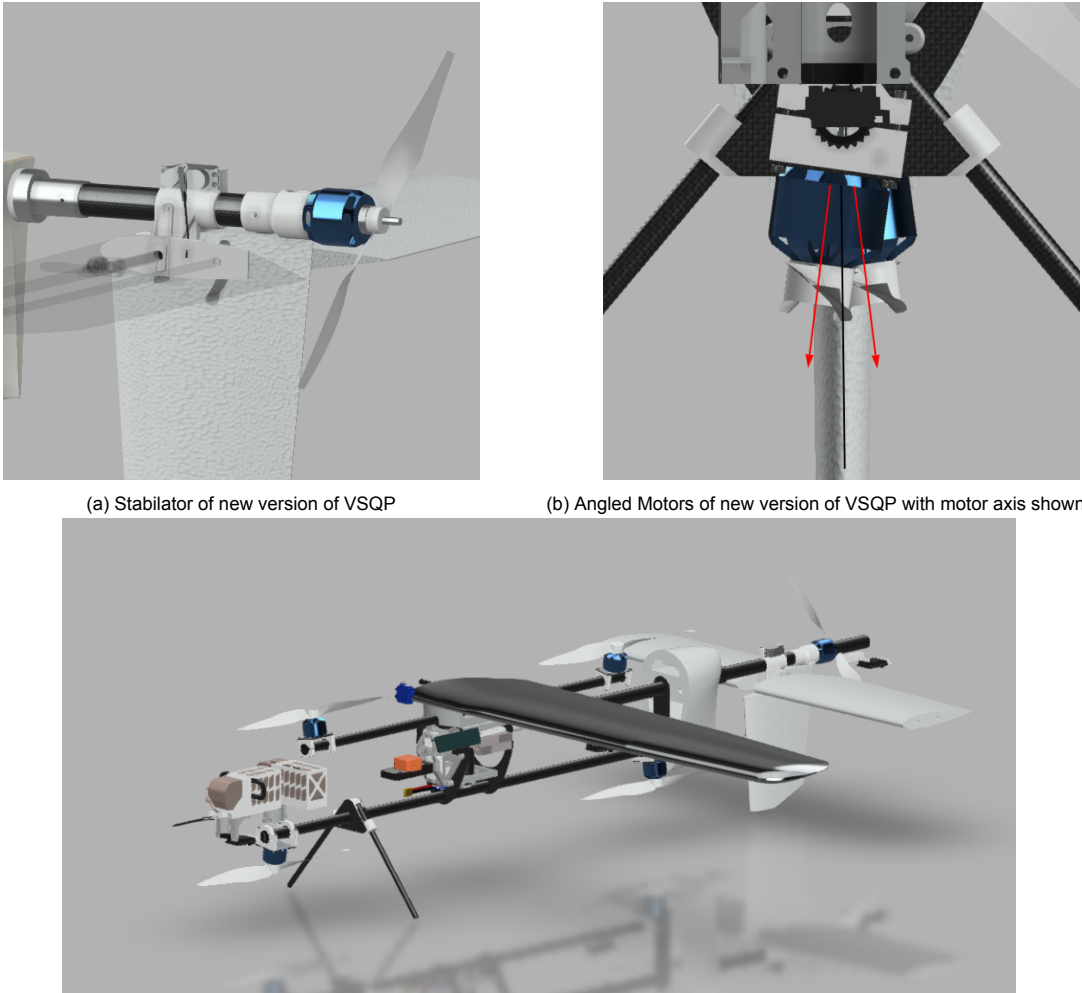
The asymmetry created by the rotation of the wing on a classical oblique wing creates cross products of inertia that are no longer zero for I_{xy} and I_{yx} . It must be noted that for the VSQP, due to the hover motors mounted perpendicular to the wing and rotating with it, the imbalance in mass is partially compensated and I_{yx} and I_{xy} could be assumed as 0 [10].

Aerodynamic Forces

The skewed wing produces side force, pitching and rolling moment that change the trim attitude of the aircraft [14]. As shown in Figure 5.3a, the velocity v_0 is divided in the chordwise component v_n and the parallel component v_t . Drag is generated from the chordwise airspeed into D_{NL} . Due to the asymmetry of the wing, drag forces are projected laterally in the same direction on each wing, creating a side force. As the skew angle decreases (more sweep), the side force increases. Wang, Xu, and Yue [14] suggest to either bank the aircraft to use gravity to balance the side force or fly with a sideslip.

More lift is induced on the back swept wing due to spanwise flow. As shown in Figure 5.3b, the left wing (back swept in this case) presents higher suction and hence higher lift. This creates a right rolling moment and a pitch down moment due to the back swept wing being behind the Center of Gravity (CG) of the aircraft. These aerodynamic forces can be corrected with roll and pitch inputs from the control surfaces [13]. Experimental tests with radio-controlled models (NASA Ames) have also used propeller torque to their advantage to combat the wing-induced rolling moment.

One would assume that the forward swept wing is highly susceptible to aeroelastic divergence, a phenomenon where the lift force, twists the wing and increases the angle of attack, generating even more twist. However, wind-tunnel tests showed that oblique wing could sustain speeds much higher



than the first estimated divergence speed [13, 15]. Twisting of the wing only occurs for the forward swept wing, where the increases in the angle of attack induces roll and an instant reduction in the angle of attack and of twist on the wing. It would therefore seem that the asymmetry of the oblique wing protects it against divergence.

Coupling of Axis

The oblique wing exhibits strong coupling between the longitudinal and lateral axes. Any change in the angle of attack of the wing generates a rolling moment, as the increase of lift on the right and left wing is not symmetric [14]. As such, a pitch up maneuver initiated with the elevator leads to roll as well.

Control Surfaces Effectiveness

As the skew angle is decreased from forward flight to a hover flight configuration, the ailerons change position, reducing their roll moment arm and increasing their pitch moment arm. The control effectiveness of ailerons was modeled by De Ponti [10] as a function of skew angle and airspeed. The back swept and forward swept aileron also present different control effectiveness due to spanwise flow generating increased lift on the back swept wing. For this reason, Wang, Xu, and Yue [14] argue that it is preferable to separate the control of ailerons.

A split elevator (also named differential tail) can also be used to increase roll effectiveness even at high skew angle, where the aileron rolling effectiveness is highly reduced [13]. It should be noted that this is less of an issue for the VSQP, as at high skew angles, the hover motors are deployed and can generate a rolling moment by varying their thrust.

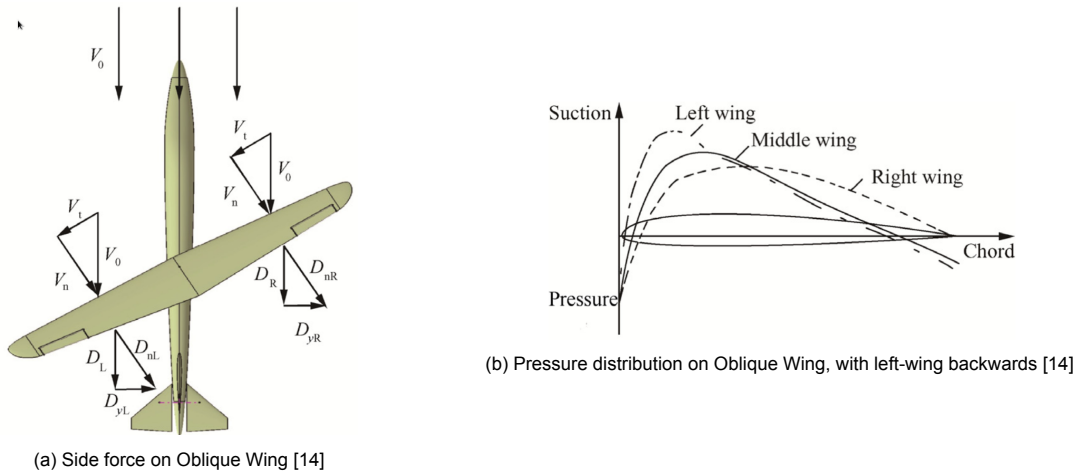


Figure 5.3: Aerodynamic Characteristics of Oblique Wing due to Asymmetry of Wing

In general, control surfaces must be coordinated to provide a single moment component. For example, consider an oblique wing as in Figure 5.3 with a right forward swept wing, with its CG centered around the wing pivot point. In order to roll left, the right aileron can be deflected downward and the left can be deflected upward. Due to the wing skew, both ailerons will in addition generate a pitch up moment that needs to be compensated by the elevator. This illustrates the need for control systems that consider the system as a whole, instead of decoupling longitudinal and lateral axis as is common for conventional aircraft. The same strategy should be applied to the VSQP to obtain adequate control during flight with a skewed wing.

With the following knowledge in mind, should a control surface fail, its impact will be more complex to evaluate on an oblique wing than on a conventional aircraft, due to the coupling it might generate between axis and due to its variable effectiveness.

5.2. INDI

INDI is a control method derived from Nonlinear Dynamic Inversion (NDI). NDI is a control method developed where the non-linear dynamics of a system are inverted to obtain a closed loop system acting as a linear system that can then be controlled using conventional linear control methods. With NDI, gain scheduling is no longer required as it directly incorporates the aircraft's non-linearities in the dynamics inversion. Additionally, the aircraft-dependent handling qualities can be separated from those generated using the control laws, as the NDI resulting linear system should be the same for every aircraft. A drawback of NDI is that it is highly model-dependent and performance can be severely altered should there be model mismatch [16]. In this case, the NDI controller is no longer linearizing the non-linearities of the system. Obtaining a precise and exact model of a UAV can be time consuming and especially hard in the case of hybrid UAVs, where the transition is hard to model.

5.2.1. General Principles

INDI was developed as a variation of NDI to reduce model dependency by relying instead on sensor data. Consider the following system:

$$\dot{x} = f(x, u) \quad (5.1)$$

The system can be linearized at the current time 0 using Taylor's expansion:

$$\dot{x} \simeq f(x_0, u_0) + \frac{\partial f(x, u)}{\partial x} \Big|_{\substack{x=x_0 \\ u=u_0}} (x - x_0) + \frac{\partial f(x, u)}{\partial u} \Big|_{\substack{x=x_0 \\ u=u_0}} (u - u_0) \quad (5.2)$$

$$\dot{x} \simeq \dot{x}_0 + F(x_0, u_0)(x - x_0) + G(x_0, u_0)(u - u_0) \quad (5.3)$$

$G(x_0, u_0)$ is defined as the control effectiveness of the system and will be used extensively in the INDI controller. Equation 5.3 can be simplified using the time separation principle if the sample rate is high

[17]. This assumption is valid when the actuators are fast and have more effect on the change of state than the dynamics of the system F . In this case, the term $F(x_0, u_0)(x - x_0)$ can be neglected:

$$\dot{x} \simeq \dot{x}_0 + G(x_0, u_0)(u - u_0) \quad (5.4)$$

The INDI control can be obtained by performing the dynamic inversion, by using the Moore-Penrose pseudo-inverse G^{-1+} of the control effectiveness matrix G and defining v as the virtual control input or desired state derivative \dot{x} :

$$u = G^{-1+}(v - \dot{x}_0) + u_0 \quad (5.5)$$

In Equation 5.5, it is possible to observe the incremental nature of the INDI controller. The total control input is based on the last control input u_0 and the difference between the desired state derivative v and the actual measurement \dot{x}_0 . This difference is used as an increment to the last control input. The only part of the controller that is model-dependent is the control effectiveness matrix G that can be analytically obtained or estimated using test flight data[18]. Note that \dot{x}_0 must be measurable as well.

5.2.2. INDI for Stabilization and Guidance

The INDI controller has been used frequently on UAVs for attitude control [6]. A cascaded architecture has been implemented, where two INDI and linear controllers are used to provide outer loop position control (guidance) and INDI inner loop attitude control (stabilization) [6, 1]. The general architecture of the controller is presented in Figure 5.4. The linear controllers are used to generate the pseudo-input v used as reference for the INDI controllers. As two different INDI controllers are used, two different control effectiveness matrix must be computed, one for the effectiveness of the UAV's actuators to induce angular accelerations and one for the effectiveness of attitude and thrust levels to induce position acceleration.

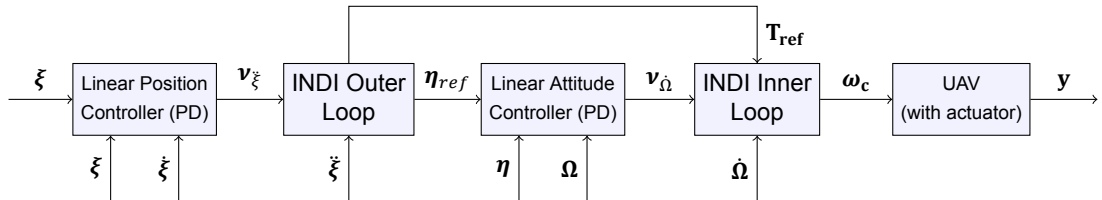


Figure 5.4: Cascaded version of INDI based on Smeur, Croon, and Chu [18], with position ξ , attitude η (NED), angular rate Ω , thrust T , commanded motor rotation ω_c , system output y

In the inner loop, the angular rate derivative is required to control the attitude. It can be obtained by differentiating the gyroscope measurement. As this measurement is often noisy, it must be filtered, which delays the measurement to the INDI controller. To avoid completing an iteration of the INDI controller with non-synchronized measurements, the actuator measurement must be filtered with the same time delay [18, 19]. For the outer loop, the accelerometers can directly provide the acceleration measurements.

An additional controller, not shown in the figure, can be used to counteract sideslip [6], using feed forward to allow coordinated turns and using feedback from the sideslip angle β :

$$\psi = \frac{g \tan(\phi_{ref})}{V} + K_\beta \beta \quad (5.6)$$

β can be either measured with a sideslip vane or estimated. For small sideslip angle, Smeur, Bronz, and Croon [6] propose a method to estimate β from the side force f_y measured by accelerometer. During a sideslip, part of the drag force ($D = q S C_d V^2$) is projected in the Y body axis, which can be measured by the accelerometers. This leads to Equation 5.7, an estimation using a constant parameter c_1 and a bias b_1 :

$$\beta = c_1 \frac{f_y}{V^2} + b_1 \quad (5.7) \qquad \beta = c_2 f_y + b_2 \quad (5.8)$$

To obtain the values of c_x and b_x , a least square fit is completed on flight test data performed with a sideslip vane. For low airspeed, the sideslip angle is not defined with Equation 5.7. To circumvent this, the airspeed can be removed from the estimation to obtain Equation 5.8, obtaining accuracy over a broader range of airspeed [6].

5.2.3. INDI Advantages

The main objective of INDI is to reduce model dependency and is accordingly its greatest advantage. The INDI controller can rapidly be implemented on complex vehicles that would conventionally require significant modeling effort to design the controllers. The only required information from the vehicle is the control effectiveness of the actuators. This will again be an advantage when developing the controller for the new iteration of the VSQP. The same controller architecture can be used, with a shorter development time.

Another advantage of INDI is its disturbance rejection capabilities. As the measurement of state derivatives is directly used in the controller, INDI is able to react directly to disturbances that affect those states. In comparison, a Proportional Integral and Derivative (PID) controller would need to register the difference between the reference state and the actual state before taking action.

INDI provide excellent disturbance rejection against constant disturbances. Smeur, De Croon, and Chu [20] compared an INDI controller and PID controller in constant wind conditions. Due to its incremental nature, the INDI rapidly corrects for the disturbance, while the PID controller has to wait for its integral term to fill up. It can be argued that the integral term could be increased to improve disturbance rejection. This, however, leads to a decrease in stability. A trade-off must be completed between stability and disturbance rejection, which is not the case for the INDI controller.

Additionally, due to its incremental nature, the INDI controller has been shown to be robust to model inaccuracies in several simulations [19, 21, 22], where the control effectiveness matrix could be reduced by half while maintaining stability. Real world experiments by De Wagter et al. [1] has also shown that stability and adequate performance could be maintained for a 12 propeller UAV with one of its outboard propellers reversed, acting as a highly dynamic disturbance. INDI's robustness could be a great asset in some failure cases studied in chapter 7, where some actuators partially fail. INDI's robustness will be further discussed in section 8.2.

Summary

The VSQP is a unique configuration between a quadcopter and fixed wing that uses a rotating wing to transition from one flying mode to another. It possesses certain characteristics in common with the oblique wing. With the wing skewed, asymmetric forces, highly coupled dynamics and variable control effectiveness of the ailerons in the pitch and roll axis make modeling the vehicle challenging. Additionally, to generate single moments, a coordinated action of the actuators is required. Transition is therefore a critical flight phase for failures. The INDI controller was used on the VSQP prototype as it requires limited model knowledge, at the expense of increased sensor dependency. Using the control effectiveness of actuators on the states of the vehicle, the nonlinear dynamics can be inverted to obtain a linear system, easily controllable using classical control methods. A cascaded architecture is used on the VSQP to provide stabilization in an inner loop and guidance in the outer loop. The incremental nature of the INDI controller, provides high disturbance rejection capabilities and high robustness to control effectiveness inaccuracies. Additionally, by using the states derivatives internally, INDI is able to react immediately to disturbances.

6

Fault Tolerant Control Methods

This chapter broadly reviews the different types of FTC that can be used to increase safety on a vehicle as the VSQP. Passive and active FTC are compared in section 6.2 and 6.3 to show how their advantages could be used for specific failures modes. The two most common categories of fault detection methods, model based and knowledge based, are explored in subsection 6.3.1 to understand their limitations. The review is not intended a an in-depth assessment of FTC methods, as specific applications to the pitot tube failure will be explored in more details in chapter 8.

6.1. FTC General Principles

The main elements of a control system are: the plant (main system dynamics), actuators and sensors. Each of these elements can fail in different ways, from partial performance degradation to a complete failure, leading to different effects on the whole system: measurement errors, changed dynamics of the plant, inability to apply control action [23]. Any system that can compensate for a fault while maintaining stability is said to be fault tolerant [24]. FTC improves the safety and reliability of a system and can generally be categorized in two main types: passive and active.

6.2. Passive FTC

Passive FTC is closely linked to robust control, where the controller does not rely on knowledge of the fault but instead relies on hardware redundancy and the natural robustness of a fixed controller to certain faults [24]. When multiple hardware components used in parallel are subjected to the same input, their output can be compared to switch between redundant components should a fault happen. This method is used extensively in aviation, where the control system (different boards running different codes), actuators (different energy types) and sensors are tripled if not quadrupled [4]. This control strategy is simple, requires low computational power and can rapidly accommodate itself to the fault [25]. Sliding mode control and H_∞ are common approaches used to design passive FTC.

Passive FTC is therefore highly dependent on hardware redundancy, which increases the size, weight and cost of its implementation. On smaller platforms like Micro Air Vehicles (MAVs) where weight is critical, implementing this fault-tolerant method may not be feasible unless the hardware redundancy can be miniaturized (e.g. in the avionics) or is already present (over-actuated systems). Another disadvantage of passive FTC is its normal performance without faults. In order to accommodate a wide variety of faults without changing its controller, a passive FTC is generally more conservative to guarantee stability should a fault arise [24].

For a vehicle with narrow performance margins like the VSQP prototype, having to design a conservative controller for passive FTC is probably not feasible to allow stable flight. However, with the changes brought with the new VSQP iteration that increase pitch authority and overall TWR, it might be possible to implement such a controller.

6.3. Active FTC

Active FTC acts in two steps: detection and supervision. The general structure of active FTC is presented in Figure 6.1. The main goal of detection is to identify that a fault has occurred, isolate its source (which component has failed) and determine its magnitude (to which extent the component has failed). The detection component makes use of data from the actuators, plant and sensors to diagnose a fault. The compensator can take multiple actions (switch between controllers, retune gains, park the system to a safe state, etc.) to adjust the controller to maintain stability of the system after a fault.

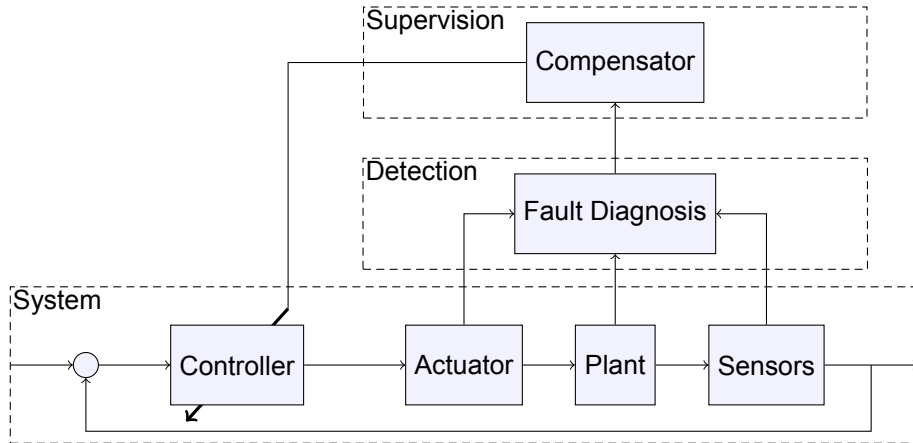


Figure 6.1: Structure of Active FTC systems (inspired by Abbaspour et al. [24])

A main advantage of active FTC compared to passive FTC that is repeatedly cited in the literature is its ability to reconfigure itself to provide optimal performance after different types of faults [24, 23, 26]. Hamadi [25] suggests that its ability to constantly monitor the system's health is an even bigger advantage. Actions can be taken before a fault worsens to a point where the vehicle cannot adapt for it. This is especially attractive for hybrid aircraft as the VSQP, where a specific fault in forward flight might not reduce performance significantly in this flight phase, but could have significant effects once in hover flight. The fault could be identified in forward flight and an emergency landing in forward flight or parachute landing could be initiated instead of risking landing in hover configuration.

Understanding the inner workings of active FTC shows how dependent it is to its ability to detect faults. If a fault is detected late or not detected at all, the system is left unprotected. Additionally, its high computational requirements could make it unattractive for applications onboard a MAV, where computing power is limited. Approaches proposed by Hansen, Blanke, and Adrian [27] that use telemetry and offline detection for failure cases that develop slowly have a potential for use with MAVs, although dependency to the telemetry link is introduced.

6.3.1. Detection

Abbaspour et al. [24] claims that fault detection is the most important part of an active FTC system. The main design factors for detection are accuracy and speed. If the faults are not identified correctly, the system might adapt itself when no fault is occurring (false positive) or not adapt to a fault (false negative). Detection can be achieved using different methods requiring variable knowledge of the system's model and/or prior input-output data from the system.

Model Based

Model based detection methods are centered around comparing the system's actual behaviour to a model of the system. The model can be obtained either using first principles or system identification. One of the simplest model based detection is based on a linearized system observer:

$$\begin{cases} \hat{x}(k+1) = A\hat{x}(k) + Bu(k) + Kr(k) \\ r(k) = y(k) - \hat{y}(k) \\ \hat{y}(k) = C\hat{x}(k) \end{cases} \quad (6.1)$$

where:

\hat{x} = Estimate of State
 \hat{y} = Estimate of Output
 r = Residuals
 K = Observer Gain

The observer gain must be selected to optimize the observer's sensibility to fault while making it robust against disturbances [23]. One simple method to detect fault is to compare the residual to a threshold corresponding to a fault. The threshold value must be selected as a compromise between false positive and false negatives. To isolate the fault to a specific component, Hansen and Blanke [28] suggests using a set of observers and residuals that are only sensitive to specific component failures. This assumes that the faults can only happen on these components. Another approach to fault detection is to use stochastic methods to analyze the whiteness, mean and covariance of the residuals. Different variants of the Kalman filter are generally used in this case [24].

Knowledge Based

Knowledge-based methods don't require a model of the system. Using a large amount of historical data from the system, pattern recognition algorithms can determine which behaviours of the system are seen as "healthy" and which are out of the ordinary, potentially indicating a fault [23]. This method is less relevant for the VSQP as it is currently developed and possesses limited flight data. For this reason, this detection method was not explored further.

6.3.2. Supervision

The supervision phase of the active FTC adapts the controller to maintain stability after a fault (see Figure 6.1). Several methods have been examined in the literature, the most common being control allocation and controller reconfiguration (change of gain or architecture).

In cases where the vehicle possesses redundant effectors, the control allocation scheme can be modified. For a constrained quadratic formulation of control allocation, Zhang [29] proposes to change the weighting matrix W used:

$$\begin{aligned} J &= \arg \min_u u^T W u \\ \text{s.t. } v_i &= B_{ui} u \end{aligned} \tag{6.2}$$

where:

$W = \text{diag}([w_1, w_2, \dots, w_m])$, with m as the number of actuators

With a fault on actuator j , the weight of w_j can be set to infinity or the actuator can be completely removed from the control allocation scheme by changing its formulation. This leads to control efforts to be redistributed to the remaining healthy actuators. This method is only effective in situations where redundant actuators are available as replacements Zhang [29].

In cases where control allocation is not sufficient to maintain stability and performance of the system, additional modifications to the controller are needed. Those modifications are as varied as the number of design parameters in a controller. Milhim, Zhang, and Rabbath [30] propose using gain scheduling, with gains calculated for fault-free flight and for different known faults on a quadcopter. Although simple, this method can only guarantee stability for the selected fault cases. Zhang [29] proposes an adaptive scheme capable of changing high level control gains when tracked states are outside defined boundaries, to bring back the tracked states to an acceptable level, even if the vehicle has less control authority. Ducard et al. [31] use a different strategy to acknowledge the loss of performance in the vehicle and adapt its controller. It evaluates the stability of an aircraft after an aileron fault and adjusts the maximum bank allowable accordingly. With this new saturation limit, the guidance controller's gains are adapted to only generate feasible paths. This strategy could also be used to guarantee flight within a strict flight envelope that satisfies assumptions used to design a fault controller (e.g. low bank angles, small rate of climb, etc.).

This limited overview of supervision algorithms show that any parameter in a controller could be used as a potential parameter to be changed by active FTC. Different strategies can be desirable depending on the type of fault, desired coverage of the FTC, vehicle dynamics, etc.

Summary

Table 6.1 summarizes advantages, disadvantages and examples for active and passive FTC. Passive FTC is well suited in situations where physical redundancy is present. As it does not require to detect faults, it is simple to implement and can rapidly accommodate a fault. Active FTC can provide optimal performance for specific faults and does not require additional hardware, although its performance is extremely dependent on detection of faults. For a vehicle like the VSQP where redundancy is limited, the active approach seems preferable, although its higher computational load might limit the use of a complex detection algorithm.

FTC Type	Advantages	Disadvantages	Examples
Passive	<ul style="list-style-type: none"> -Simple -Low delay between fault and accommodation 	<ul style="list-style-type: none"> -Dependent on redundancy -Assumes stability can be attained for any type of fault -Conservative controller 	<ul style="list-style-type: none"> -Voting System -Sliding Mode Controller [32, 33, 25] $-H_\infty$
Active	<ul style="list-style-type: none"> -Optimal performance for fault -Does not require additional hardware 	<ul style="list-style-type: none"> -Highly dependent on detection -High computational load 	<ul style="list-style-type: none"> -Control Allocation [33] -Controller Reconfiguration (gain, architecture) [8, 34, 30] -Model Predictive Control (MPC)[35]

Table 6.1: Summary of different FTC methods

7

Critical Failure Cases

This chapter identifies the most critical failure cases for the VSQP and reviews solutions suggested in the literature. Subsection 7.1 justifies the use of the FMEA method to evaluate failure modes and explains the criteria used to evaluate the severity and probability of failures. The full FMEA is presented in Appendix A, leading to the selection of the rotor loss, stuck stabilator, wing angle sensor fault and pitot tube failure as the most critical failure cases for the VSQP. Section 7.2 explores existing solutions and open challenges relative to each failure case.

7.1. Failure Mode and Effects Analysis

To assess reliability and identify the most critical failure modes of a vehicle, multiple tools can be employed. The most commonly used are the FMEA and the fault tree analysis. The fault tree analysis divides a system in different components and evaluates the probability of failure of each component. Its purpose is to understand how overall reliability is affected by each system's reliability. According to Reimann et al. [36], this tool is well suited to determine relationships and interactions between failures to obtain a better estimate of overall reliability. Fortna Murtha [37] adds that the fault tree analysis is a tool better used in the early design process, where each system is generic and no component is chosen yet.

Once a system is built and components chosen, the FMEA is more commonly used. Either using a top down (identify the components that can cause a specific system failure) or bottom-up (identify the effect of a component's failure) approach can be used to identify all failure modes of a UAV. Freeman and Balas [38] and Reimann et al. [36] both favor a bottom-up approach where failure modes are analyzed at the component level and for which the effect on a system level is then analyzed. It is easier to list all components and their failure mode and explore their effects on the overall system than perform the opposite strategy. As the end goal is not to obtain the quantitative reliability of the VSQP, but to identify the most critical component qualitatively, the application of the FMEA from a bottom-up approach is considered sufficient.

7.1.1. Listing Failure Modes

For the FMEA, the VSQP is separated into its various systems: actuators, sensors, structure and electronics. Each system is divided in different components that have different failure modes. These failure modes must be evaluated in its different flight phases:

- Hover
- Forward Flight
- Transition from hover to forward flight
- Transition from forward flight to hover

Figure 7.1 presents a tree visualization of how the failure modes were enumerated. A complete list of all failure modes and components evaluated can be found in Appendix A.

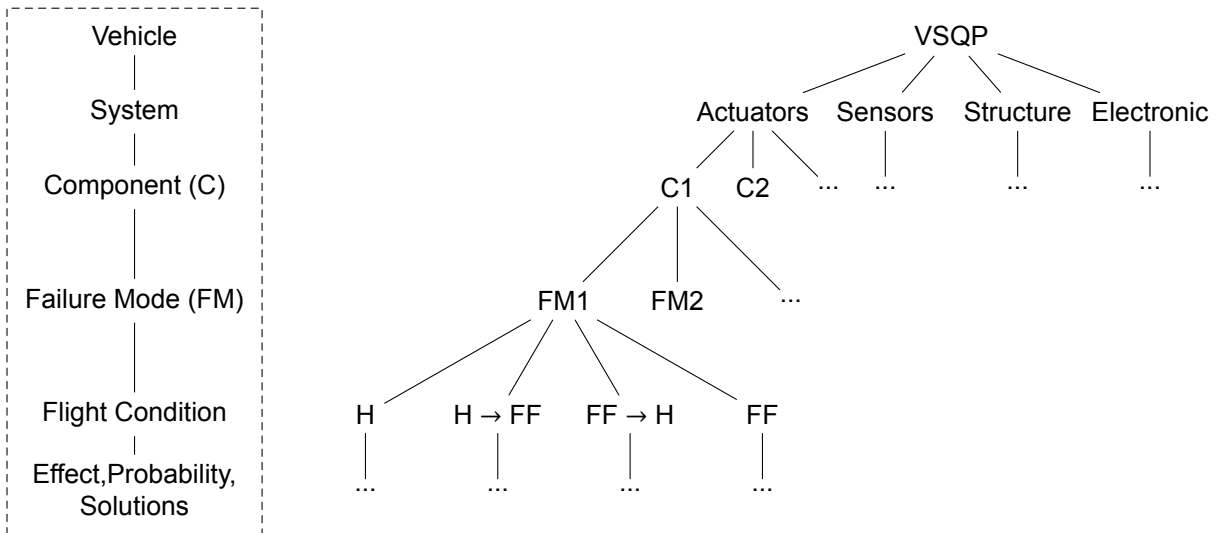


Figure 7.1: Tree Visualization of the Failure Mode and Effect Analysis, with the actuator system branch expanded. H = hover, FF = Forward Flight and the → signify a transition from one state to the other

7.1.2. Severity and Probability of Failure

The ultimate goal of this research is to improve the safety of the VSQP and, not primarily improve its mission reliability. However, improving its overall reliability should also improve general mission reliability. Therefore, the severity scale used and presented in Table 7.1 is more similar to work completed by Petritoli, Leccese, and Ciani [12], which is centered around effects on the drone and people on the ground, compared to a more classical severity scale based on mission objectives completion completed by Freeman and Balas [38].

Severity	Explanation
High	<ul style="list-style-type: none"> -Loss of control is inevitable after failure (uncontrolled crash) -Could result in damage to vehicle and to people on ground
Medium	<ul style="list-style-type: none"> -Stability can be maintained temporarily but might still lead into a controlled crash -Lower chance of causing damage to vehicle and to people on ground
Low	<ul style="list-style-type: none"> -Stable flight can be maintained after failure -Alternate configuration or redundancy is present on the vehicle -Might cause a mission abort, but vehicle is still able to fly

Table 7.1: Severity Classification of Failure Modes

Probability of failure can be estimated using reference data such as the *Nonelectronic Parts Reliability Data Publication* [39], tests results found in the literature [37, 12, 40] or general knowledge of systems if no data was found for a specific component. The most critical failure modes are identified using a risk matrix, where the most critical component presents the highest severity and probability of occurrence, as shown in Table 7.2.

7.2. Selected Critical Failure Cases

The FMEA method led to the identification of the VSQP's four most critical failure, presented in Table 7.3. The result is a blend of critical failures modes specific to fixed wing vehicles (stuck stabilator, pitot tube failure) and rotorcraft (complete rotor loss) in addition to one failure case (wing angle sensor) specific to the VSQP platform. Literature for fixed wing and rotorcraft come to similar conclusions. Reimann et al. [36] determined that for a fixed-wing radio-controlled aircraft, the most critical failure modes were affecting the servomotors, the radio-controlled receiver and propellers. Matsuda, Ibuki,

Probability of Occurrence	Severity		
	High	Medium	Low
High			
Medium			
Low			

More Critical

Table 7.2: Risk Matrix Used to Classify Failure Modes by Criticality

and Sampei [41] conclude that a rotor loss is the most critical failure possible for a rotor craft. It is therefore logical than a hybrid vehicle encompassing features of both fixed wing and rotorcrafts is subject to failures for these two configurations. The following sections will review these failure cases, solutions in the literature and existing knowledge gaps, as summarized in Table 7.3.

7.2.1. Rotor Loss

The rotor loss failure case is defined as the complete loss of thrust from one of the rotors of the vehicle, in hover or in transition. On multicopters, the most common solution to this type of failure is redundancy. Using configurations with additional rotors such as octo or hexacopters, controllability can be maintained after a single rotor failure [42]. For quadcopters, a new strategy must be used to maintain stability as at least four actuators are required to independently control the roll, pitch, yaw angles and thrust level [41].

Quadcopter

Mueller W. Mark and D'Andrea Raffaello [43] define a new state of equilibrium in the case where a conventional quadcopter is subjected to a rotor loss (see Appendix B for full development). This new equilibrium state requires the UAV to relinquish yaw control and to spin rapidly around a new defined primary axis. The equilibrium yaw rate can be calculated analytically depending on the inertial properties of the drone and its drag coefficient. Different controllers have been developed and tested experimentally to attain and maintain this new equilibrium state. Mueller W. Mark and D'Andrea Raffaello [43] used a Linear Quadratic Regulator (LQR), Lu and Kampen [44] implemented an active FTC switching between two INDI controllers and Ke, Cai, and Quan [45] used a switch-free controller based on control allocation. The available literature tends towards the same conclusions. The quadcopter becomes rapidly unstable after failure, requiring a fast detection algorithm and rapid yaw rate increase after the failure rate. With small but powerful quadcopters, the equilibrium yaw rate is achieved within less than 1 sec. Ke, Cai, and Quan [45], using a spinning top analogy, expect larger quadcopters to be less controllable in the new equilibrium position due to their lower equilibrium yaw rate in consequence of their higher drag coefficient.

Hybrid Vehicle

The new state of equilibrium presented in the last section is well documented in the literature for small and powerful quadcopters similar to racing drones but is scarce for implementations on larger quadcopter or hybrid vehicles featuring wings and a tail. The tail increases the rotational drag coefficient significantly due to its long moment arm. The fuselage, wing and tail could create moments that would act as disturbances on the system. To the best author's knowledge, there is no existing data regarding rotor loss on a configuration similar to the VSQP: quadplane with a tail. The closest analog is work on a quad-plane flying wing configuration by Wang and Sun [9]. An INDI controller with adaptive sliding mode is used to maintain stability after rotor loss. Computational Fluid Dynamics (CFD) was used to model the reverse flow that occurs over the retreating wing during the fast rotation. The INDI controller treats the wing as a disturbance in the system and is able to reach and maintain a high yaw rate equilibrium state in the simulation. The adaptive controller developed allowed better position tracking than

a normal INDI controller but lacks validation in an experimental real-life setting.

Early Calculations VSQP

As no existing literature was found on the VSQP's specific configuration, the model developed by Mueller W. Mark and D'Andrea Raffaello [43] was adapted to model the effect of a vertical stabilizer and the angled hover motor on the equilibrium state. The latest geometric, inertial and propulsion-related parameters from the VSQP were used. The modified model is developed in Appendix B. The conclusions from this preliminary estimation indicate that the VSQP could reach and attain an equilibrium state as defined by Mueller W. Mark and D'Andrea Raffaello [43], although its degree of controllability and stability is much harder to define [45]. With a planned TWR of 2, the VSQP can maintain the new equilibrium position with 10% surplus thrust for maneuvering. The tail surface does lowers the equilibrium yaw rate (from approx. 20 rad s^{-1} to approx. 12 rad s^{-1}), but also makes it harder to reach due to the increased drag coefficient. The angled hover motor help reach the equilibrium yaw rate faster, depending on their angle (angle not fixed yet on the new the VSQP). It appears like the equilibrium yaw rate could be attained under 1 sec. However, this assumes an instantaneous fault detection and spool up of the motors. This time delay would probably be the main limitation to the ability of the VSQP to attain and maintain stability after a rotor loss.

As airspeed increases during transition, the wing starts generating lift, reducing the required hover motor commands. The control effectiveness of the control surfaces increases as well. Should a rotor loss occur during transition, there is a speed at which the aircraft should have enough control surface authority to continue through transition. Afterwards, a landing in fixed-wing configuration can be completed. Similar to a V1 speed on an airliner, this speed could be used as a decision point for the controller to decide whether to continue with the transition or to initiate the fast spin up of the vehicle to attain the fast yawing equilibrium state.

Additional solutions have been explored for the rotor loss. A two axes gimbal could be added to the pusher motor to counteract the moments induced by the rotor, as shown in Figure 7.2. In this configuration, the pusher motor can produce large pitch (M_y) and yaw (M_z) moments with a combination of gimbal angles and pusher motor thrust. However, its effectiveness in roll (M_x) is limited to the reactionary torque of the motor. In the event of a pitch hover motor failure, the most critical failure would be a front motor failure, as the gimbaled pusher motor would need to counteract the rear hover motor pitch down moment by generating thrust downward. The TWR required by the motors to maintain flight depends on the pitch moment arm of the pusher motor.

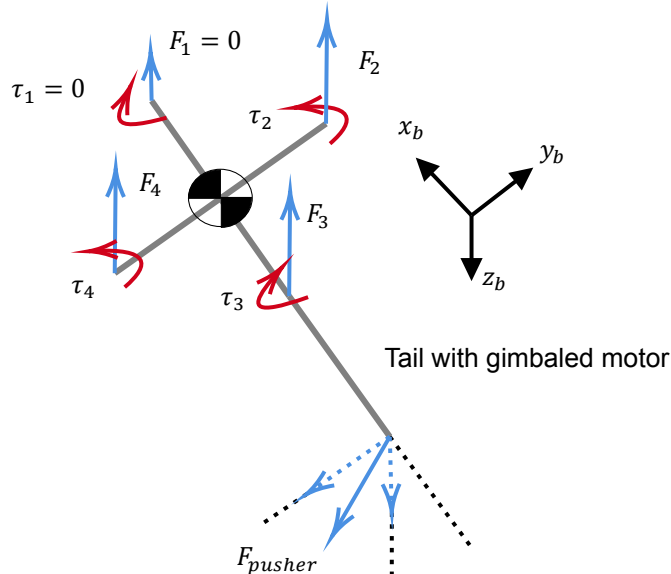


Figure 7.2: Gimbaled pusher motor with front motor failure

In a roll hover motor failure, the TWR requirements are more stringent. As the gimbaled pusher motor has no sustained effectiveness in roll, any roll moment would need to be generated by the remaining

healthy roll motor. The pusher propeller would be required to counteract the yaw moment generated by the roll motor. All vertical thrust would need to be generated by the pitch motors. As such, a TWR higher than two would be required. The gimbaled pusher motor has potential to allow stable flight after a hover motor fault. Finally, if flight cannot be sustained in a normal configuration, the gimbaled pusher motor could be used to generate sufficient yaw moment to accelerate the drone to a stable rotative stability state.

7.2.2. Stuck Stabilator

This failure refers to the case where the horizontal stabilizer is stuck in full deflection (either completely up or down) and cannot be moved. This results in loss of pitch authority from the horizontal stabilizer and induces a pitching moment dependent on the airspeed. The failure is therefore more critical in high-speed forward flight.

To regain pitch authority, cross-functionality of aerodynamic controls could be used. For example, ailerons and flaps can be used to generate a pitching moment if the elevator was to fail. Venkataraman et al. [46] propose to evaluate the flight envelope in which an aircraft can be trimmed using flap deflection and airspeed for different stuck elevator angles. This evaluation only considers an elevator failure, while a stabilator failure can generate considerably more pitching moment due to the whole horizontal surface moving. The allowable flight envelope will be reduced if the only actuators used to generate pitching moments are the flaps. In the case of the VSQP, another solution can be explored. Recall that pitch effectiveness of the aileron is a function of the skew angle of the wing. By skewing the wing back from the fixed wing angle, it would theoretically be possible to gain pitch authority.

In forward flight, the hover motors from quad planes like the VSQP are turned off for lower power consumption. Prochazka and Stomberg [47] and Mizrak, Alwi, and Edwards [32] propose to employ them to generate a pitching moment if the elevator fails. Using control allocation weighted with the fault state of the actuators ($W = \text{diag}(w_1, w_2, w_3, \dots)$, with $w_i = 1$ for a fully functional actuator and $w_i = 0$ for a faulty actuator), the virtual control can be reallocated from control surfaces to hover motors:

$$u(t) = WB_2^T (B_2 W^2 B_2^T)^{-1} v(t) \quad (7.1)$$

where:

$u(t)$ = command sent to the actuators

$v(t)$ = virtual control

B_2 = hover motor input matrix.

A sliding mode controller is used to adjust the controller's gains when the elevator fails to maintain the same dynamics as when using the control surfaces for stabilization. A simulation at a specific trim point validated that the controller could maintain tracking performance in cases of loss of effectiveness and complete control surface hardover (locked in place). Further work is needed to apply the controller to the whole flight envelope of a quad plane and to validate with flight testing.

For the VSQP, a symmetric airfoil, elliptic lift distribution and thin airfoil theory can be assumed to determine the maximum airspeed at which a full 15° stabilator failure can be managed while keeping 15% of thrust for maneuvering. Using one, two or all hover motors, they can respectively generate sufficient pitching moment up to 14 , 17.5 and 23.5 m s^{-1} . The lower limit is within the transition airspeed of the aircraft. If this method is to be further studied, more than one motor should be used for alternative pitch control.

It is unclear how a fully deflected stabilator could affect the transition of the VSQP. The rear hover motor and elevator were already fully saturated during tests of the VSQP prototype. A fully deflected stabilator could lead to a situation where the transition is no longer possible and where a fixed-wing landing is required.

7.2.3. Wing skew angle Sensor Failure

The wing angle sensor failure refers to the loss of the wing skew angle, measurement. It is used in the calculation of the control effectiveness of the ailerons, rotating hover motors and wing lift [10]. When operating in forward or quad mode with a fixed angle, a sensor failure has minimal consequences. The

likelihood of such a failure during the transition is low, as it only happens twice per flight and within a short time frame. Nonetheless, fault detection algorithms could be employed to identify sensor failures and, in response, either initiate a return to land or execute a forward flight landing instead of transitioning

The simplest and most effective solution is to add redundancy to the sensor. Rotary sensors are light, low cost and precise when compared to other alternatives such as an online skew angle estimation from the flight dynamics of the vehicle [48]. Different types of sensors (e.g. hall effect, potentiometer) should be used to limit common fault modes.

7.2.4. Pitot Tube Failure

The pitot tube failure refers to the complete loss of airspeed data. On airliners, the pitot tube generally fails due to water ingress, water freezing and clogging the inlet tube¹. On smaller UAV's pitot tubes that are not equipped with a drain tube, water blockage in the inlet tube is sufficient to clog the pitot, as shown in Figure 7.3. The pressure slowly or immediately drops, resulting in a reduced or zero airspeed reading [3]. It is a failure with important effects on the VSQP, as airspeed is required to compute the control effectiveness for both the stabilization and guidance controllers, as well as being used for the wing skew schedule. If airspeed data is lost, the control effectiveness can no longer be calculated for control surfaces and the lift model of the wing. The dependence of airspeed on the VSQP will be further explored in section 8.1.

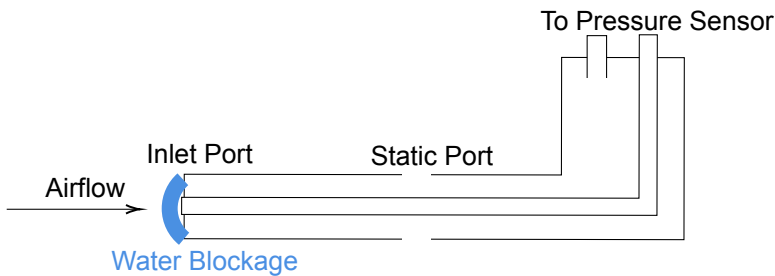


Figure 7.3: Water Blockage Pitot Tube Failure Mode

If multiple pitot tubes are present on the vehicle, redundancy and a voting scheme can be employed to disregard erroneous measurements coming from the faulty pitot tube. This cannot be easily implemented on the VSQP due to weight constraints. Additionally, if one pitot tube is subjected to water blockage (when flying in highly humid environment), it is highly likely that the other pitots will suffer from the same failure, as their failure modes are not independent [4].

There is a significant body of work that deals with the estimation of airspeed using sensors normally found on airliners (high precision Inertial Measurement Unit (IMU), angle of attack and sideslip vane, Global Navigation Satellite System (GNSS)) receiver, known as synthetic air data estimation [3, 49, 50]. Limited literature is available relative to MAVs, which are generally not equipped with an angle of attack and sideslip vanes. These methods are explored further in subsection 8.3.1. When sensors are limited, model based methods can be used to take advantage of knowledge of drag, lift and propulsion characteristics of the aircraft to estimate airspeed (presented in subsection 8.3.3).

Even if an estimate of airspeed is obtained using alternative methods, it might be uncertain and lead to instabilities if the controller is highly dependent on it, as can be the case for gain schedules. INDI has been shown to be robust to control effectiveness inaccuracies in several simulations [19, 21, 22], although validation in experimental settings are more limited. Hansen and Blanke [28] use an active FTC that reverts to a more conservative attitude control that is no longer gain scheduled with airspeed when a pitot tube failure is detected. This assumes that control gains were already generated for the failure case and are guaranteed to stabilize the aircraft. This can be hard to attain for hybrid aircraft operating in a large speed envelope with different flight modes.

Airspeed uncertainty was covered in work by Smeur, Bronz, and Croon [6] in a slightly different scenario. For a tail sitter hybrid UAV with a fixed pitot tube, the airspeed measurement becomes imprecise

¹<https://www.avweb.com/flight-safety/risk-management/pitot-static-system-failure/>

as the angle of attack is increased. The control effectiveness of this vehicle was function of airspeed. To circumvent the possible control effectiveness matrix computation errors in high angle of attack scenarios, a composite control effectiveness function was used:

$$G(\theta, V) = \begin{cases} G(\theta) & \text{if } V < \text{Threshold Airspeed} \\ G(V) & \text{if } V \geq \text{Threshold Airspeed} \end{cases} \quad (7.2)$$

where:

$G(\theta)$ = Control effectiveness based on pitch angle

$G(v)$ = Control effectiveness based on airspeed

Both control effectiveness matrices were calculated using a least square fit in changes of angular acceleration depending on control surfaces actuation. Over a threshold velocity, the control effectiveness is computed using the measured airspeed. As the angle of attack increases, the airspeed measurement by the pitot diverges from the real airspeed. Under a set threshold airspeed, the control effectiveness is estimated using the pitch angle. In the case of the tail sitter, the pitch angle was representative of the general airspeed of the aircraft (assuming no climb gradient). The scenario is different for the VSQP. With the over-actuation of forces in the outer loop, the vehicle can both tilt forward with its hover motor or use the pusher motor to generate forward thrust. The composite control effectiveness could not be used directly on the VSQP, but potential variations could be implemented in forward flight, where the hover motors are shut down.

Summary

The FMEA was used to identify failure modes and classify their impacts and probability of occurrence to evaluate their overall criticality. This lead to the identification of the four most critical failure modes on the VSQP: the complete rotor loss, the stuck stabilator, wing skew angle measurement failure and pitot tube failure. Existing solutions and knowledge gaps are presented for each failure case in Table 7.3.

The single rotor loss is a failure mode well documented for small but powerful quadcopters. By reaching a new state of equilibrium in fast rotation around a primary axis, stability can be maintained. It is function of the physical parameters of the quadcopter, with the drag coefficient playing a major role. Limited literature exists regarding configurations that include a tail, fuselage and wing that increase the drag coefficient and introduce disturbances in the system when spun rapidly. Early calculations estimated the VSQP's equilibrium state to be at a lower angular rate due to the increased drag coefficient of the tail. If instantaneous detection and motor spool up is assumed, the VSQP could attain the equilibrium state in 1 second. This time frame appears to be the upper limit to maintain stability after a rotor loss. Additional solutions for the rotor loss such as using a gimbal pusher motor was explored, but the vehicle would still be susceptible to side hover motor failure and require a high TWR.

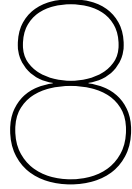
The stuck stabilator failure could be solved using redundant control surface. By rotating the wing, the ailerons can generate pitching moment. Nevertheless, the most effective method would involve using the fixed hover motors to generate pitching moments, that are normally unused during forward flight, where this failure case would be the most severe. The main knowledge gap for this failure case covers the airflow dynamics during transition, which could generate substantial forces on the stabilizer.

The wing skew angle sensor failure has severe effects on the calculation of the control effectiveness of the rotating hover motors and the ailerons, but can be easily fixed using simple sensor redundancy. Alternative methods to estimate the wing angle could be used using the aircraft dynamics, but would be unnecessarily complex.

Ultimately, the pitot tube failure presents the most severe effects on the controller, as airspeed is used both in the guidance, stabilization control effectiveness and in the wing skew angle schedule. Its occurrence can be high as MAV's pitot tube are generally not equipped with a drain tube, making them susceptible to water blockage in high humidity environments. Different synthetic air data estimation methods to estimate airspeed using other sensors available on the vehicle are documented. Other methods focus on changing the controller's architecture and parameters to maintain stability after losing airspeed data. The pitot tube was chosen as the most critical failure mode that warrants additional research.

Failure Case	Solutions	Knowledge Gaps
Complete Rotor Loss	<ul style="list-style-type: none"> -New equilibrium point in high yaw rate state [45, 44, 43, 51, 9] -Gimbaled pusher motor 	<ul style="list-style-type: none"> -Effect of tail on equilibrium state -Effect of angled rotors on ability to reach equilibrium state -Time to reach equilibrium yaw rate -Critical flight condition for failure case
Stuck Stabilator	<ul style="list-style-type: none"> -Redundant control surfaces [46, 52] -Use of hover motors [32, 47] -Skew wing to gain pitch effectiveness with ailerons 	<ul style="list-style-type: none"> -Airflow dynamics on stabilator during transition -Pitch effectiveness and control using ailerons with skewed wing
Wing Skew Angle Sensor	<ul style="list-style-type: none"> -Redundancy -Skew angle estimation 	<ul style="list-style-type: none"> -Skew angle estimation
Pitot Tube Failure	<ul style="list-style-type: none"> -Airspeed estimation [3, 49, 50, 28] -Controller robustness [19, 21] 	<ul style="list-style-type: none"> -INDI robustness to airspeed uncertainty -Airspeed estimation method for hybrid aircraft -Accurate detection on hybrid aircraft

Table 7.3: Critical Failure Cases for VSQP



Pitot Tube Failure

To precisely understand the effects of a pitot tube failure on the VSQP, section 8.1 outlines the VSQP's whole controller's use of airspeed. Section 8.2 presents how INDI is highly robust to model uncertainties and how previous work attempted to quantify it but it also highlights the lack of experimental validation. Section 8.3 discusses how different sensors and/or model knowledge can be used to obtain relatively accurate airspeed estimations. Section 8.4 discusses simple detection methods based on residuals that can be used to identify failures of the pitot system.

8.1. Use of Airspeed Data on VSQP

The VSQP uses a cascaded implementation of INDI (presented in section 5.2) with a Weighted Least Square (WLS) control allocation method. Airspeed is used in multiple sections of the VSQP's controller: control surfaces effectiveness estimation, lift estimation, wing skew scheduling and general airspeed control of the aircraft.

8.1.1. Control Effectiveness Estimation

The control effectiveness of both control surfaces and hover motor must be determined for the stabilization loop (inner loop). Additionally, due to the rotating wing mechanism, the ailerons and two of the hover motors rotate with the wing skew, changing their control effectiveness depending on skew angle. De Ponti [10] defines the inner loop control effectiveness with constant inertia tensor I_v :

$$G_{inner}(\omega, \dot{\omega}, \delta, \Lambda, V, \Omega) = I_v^{-1} (M_c(\omega, \delta, \Lambda, V) - M_r(\omega, \dot{\omega}, \Omega)) \quad (8.1)$$

where:

M_r = gyroscopic moments from the motors

M_c = moments generated from the actuators

The actuator moments M_c can be further developed as a combination of hover motor moments $M_{c_{mot}}$ and control surfaces moments $M_{c_{as}}$:

$$M_c(\omega, \delta, \Lambda, V) = \begin{bmatrix} L \\ M \\ N \end{bmatrix} = M_{c_{mot}}(\omega, \Lambda, v) + M_{c_{as}}(\delta, \Lambda, V) \quad (8.2)$$

The hover motors moments are not function of airspeed if cross-flow effects are neglected [10] and therefore will not be further developed. The control surfaces moments are derived by assuming lift generation by the chordwise component of the airspeed ($V_{lift} = \sin(\Lambda) V$), linear lift coefficient of control surfaces with deflection ($L = k \delta q$) and by assuming the pivot of the wing to be coincident with

the CG of the aircraft [10]. The moment generated by the control surfaces of the aircraft are defined by¹:

$$M_{cas}(\delta, \Lambda, V) = \begin{bmatrix} b_{al}k_{al}V^2 \sin(\Lambda)^3 & -b_{al}k_{ar}V^2 \sin(\Lambda)^3 & 0 & 0 \\ -b_{al}k_{al}V^2 (\cos(\Lambda) - \cos(\Lambda)^3) & b_{al}k_{ar}V^2 (\cos(\Lambda) - \cos(\Lambda)^3) & -b_{el}k_{el}V^2 & 0 \\ 0 & 0 & 0 & -b_{ru}k_{ru}V^2 \end{bmatrix} \begin{bmatrix} \delta_{al} \\ \delta_{ar} \\ \delta_{el} \\ \delta_{ru} \end{bmatrix} \quad (8.3)$$

where:

- b_{al} = Arm of the Hover Motor to the CG
- b_{el} = Arm of Elevator to the CG
- b_{ru} = Arm of Rudder to the CG
- k_{al} = Coefficient for Left Aileron Lift
- k_{ar} = Coefficient for Right Aileron Lift
- k_{el} = Coefficient for Elevator Lift
- k_{ru} = Coefficient for Rudder Lift

For the guidance outer loop of the cascaded INDI controller, the control effectiveness between acceleration $\ddot{\xi}$ and the virtual control input $v = [\phi \ \theta \ a_{B_x} \ a_{B_z}]^T$ is defined by Van Wijngaarden and Remes [11] as:

$$G_{outer}(\eta, T, V, \Lambda) = \frac{1}{m} (G_T(\eta, T) + G_L(\eta, V, \Lambda)) \quad (8.4)$$

where:

- G_L = Lift in North-East-Down (NED) Reference Frame
- G_T = Thrust in NED Reference Frame
- a_{B_x} = Acceleration in the x -axis body Frame
- a_{B_z} = Acceleration in the z -axis body Frame

Thrust is assumed to be independent of airspeed. Only the lift control effectiveness G_L is dependent on airspeed and can be further developed:

$$G_L(\eta, V, \Lambda) = \frac{1}{m} \begin{bmatrix} \cos \phi \sin \psi L(\theta, V, \Lambda) & \sin \phi \sin \psi \frac{\partial}{\partial \theta} L(\theta, V, \Lambda) & 0 & 0 \\ -\cos \phi \cos \psi L(\theta, V, \Lambda) & -\cos \psi \sin \phi \frac{\partial}{\partial \theta} L(\theta, V, \Lambda) & 0 & 0 \\ -\sin \phi L(\theta, V, \Lambda) & \cos \phi \frac{\partial}{\partial \theta} L(\theta, V, \Lambda) & 0 & 0 \end{bmatrix} \quad (8.5)$$

The trigonometric terms originate from the transformation from body to NED reference frame. Assuming level flight, with lift generated by the chordwise component of airspeed, lift being produced even in quad mode (offset k_1) and with lift linear to the angle of attack, with offset k_2 , the lift model for the VSQP can be drafted:

$$\begin{aligned} L(\theta, \Lambda, V) &= \frac{1}{2} \rho S V^2 [m_1 \sin(\Lambda)^2 + k_1] [m_2 \theta + k_2] = \frac{1}{2} \rho S V^2 [\lambda_1 \theta \sin(\Lambda)^2 + \lambda_2 \sin(\Lambda)^2 + \lambda_3 \theta + \lambda_4] \\ \frac{\partial L}{\partial \theta}(\Lambda, V) &= \frac{1}{2} \rho S V^2 [\lambda_1 \sin(\Lambda)^2 + \lambda_3] \end{aligned} \quad (8.6)$$

where:

- ρ = Density
- S = Surface
- V = Airspeed
- k_1 = Quad Mode Lift Offset
- k_2 = Zero Angle of Attack Lift
- m_1 = Linear Coefficient for Lift Depending on Skew Angle
- m_2 = Linear Slope of Lift Coefficient
- λ_x = Parameter Encompassing Multiple Constant Coefficients

¹Note that the implementation on the VSQP assumes that the ailerons do not handle pitch control and as such, the two first terms of the second row of Equation 8.3 are set to 0 [11].

The coefficients were obtained from least square estimation with flight or wind tunnel data. The previous mathematical derivations demonstrated that airspeed squared is used in both the inner and outer loop control effectiveness. A small uncertainty in the airspeed estimation would therefore be amplified when calculating the control effectiveness.

8.1.2. Wing Rotation Scheduling

The transition on the VSQP is performed by rotating the wing according to a schedule that maximizes the control effectiveness throughout the transition. De Ponti [10] calculates the maximum control effectiveness for a grid of airspeed and skew angles to obtain surfaces $S_\phi, S_\theta, S_\psi, S_T$ for roll, pitch, yaw and the inverse of thrust utilization, respectively. By selecting weights w , a total control authority surface S_{tot} can be computed:

$$S_{tot} = [w_\phi \quad w_\theta \quad w_\psi \quad w_T] * \begin{bmatrix} S_\phi \\ S_\theta \\ S_\psi \\ S_T \end{bmatrix} \quad (8.7)$$

Depending on the weight, more emphasis can be set on maintaining sufficient roll, pitch, yaw or to reduce the thrust utilization. A modified gradient ascent is used to calculate the skew angle that maximizes total control effectiveness and only increases the skew angle to gain higher control authority. Its application on the total control authority surface is shown in Figure 8.1. By examining the flight test line, at first, with airspeed increasing, no skew angle is commanded. The control surfaces of the aircraft do not provide sufficient control effectiveness. At a speed of approx. 5 m s^{-1} , the wing is skewed to 30° , where some lift can be generated to minimize thrust utilization and the ailerons can be used to generate rolling moments. This configuration is maintained until approx. 12 m s^{-1} , where the wing skews rapidly to 90° , to attain forward flight configuration.

The choice of weights greatly affects skew schedule. In Figure 8.1, the high weight set to γ_T to minimizing the power consumption is the main driver to rotate the wing as airspeed increases. In a situation where the airspeed is uncertain, it is vital to make sure that sufficient control authority is maintained throughout the transition. Transitioning at a higher speed would meet this goal, at the expense of lower efficiency. The γ_T could be reduced in real time to change the skew schedule once a uncertain airspeed is detected.

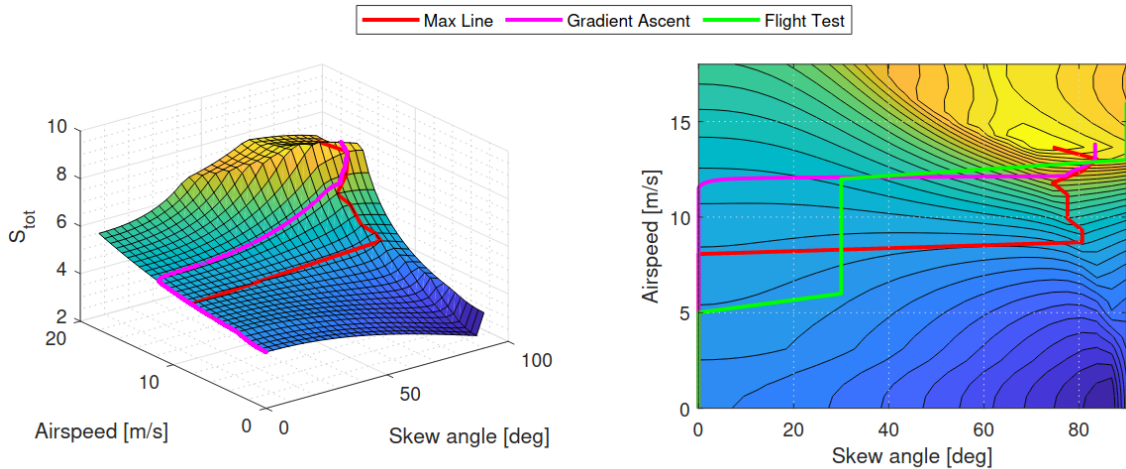


Figure 8.1: Skew Scheduling with Airspeed Using Weights $\gamma_\phi = 2, \gamma_\theta = 3, \gamma_\psi = 1, \gamma_T = 4$ [10]

8.2. INDI Robustness

INDI's main advantage is its low model dependence. Additionally, INDI is shown in multiple papers to be particularly robust to modelling errors [16, 19, 21] and disturbances [18, 1].

Veld, Van Kampen, and Chu [19] evaluated a INDI controlled general system with actuator dynamics. Stability was analyzed as a function of multiple factors: controller frequency, control gain, system gain,

control effectiveness uncertainty and measurement time delay. As a general rule, reducing the sampling time of the controller increases its ability to cope with uncertainty. For a set sampling time, the INDI controller can maintain stability with more control effectiveness overestimation than underestimation, as is shown in Figure 8.2. Although not developed in the paper by Veld, Van Kampen, and Chu [19], this is explained because if the control effectiveness is underestimated, its inverse will be larger and therefore the INDI controller will command more control input increment than is required. This can effectively lead to instability. If the control effectiveness is overestimated, the controller will command less control input than required, which might decrease performance, but will be corrected by the incremental nature of the controller. Note that the graph presented in Figure 8.2 is generated using a non-linear Cessna Citation model and can only be applicable to this model. To analyze a new system, the system's model is required and recalculation of the stability region is needed.

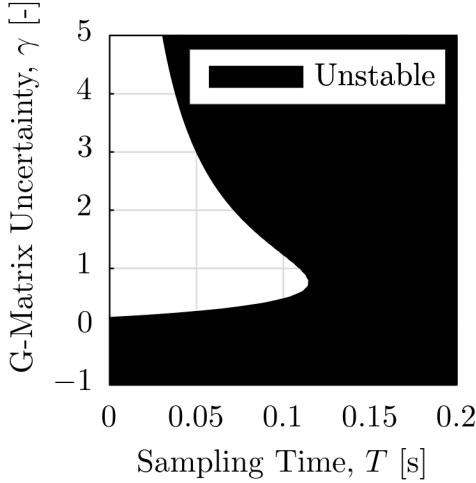


Figure 8.2: INDI Stability with control effectiveness uncertainty by Veld, Van Kampen, and Chu [19] using its non-linear Cessna Citation Model with, $F = 2$, $K_u = 13$, $K_x = 7$ and $\gamma = \frac{G}{G + \Delta G}$

It was also determined that in the case of a delayed state derivative measurement, stability is increased if the actuator measurement is delayed by the same amount. This was implemented experimentally in by Smeur, Croon, and Chu [18]. By delaying both measurements equally, the Taylor expansion fundamental to INDI (Equation 5.2) is performed with measurements using the same time step.

Although work by Veld, Van Kampen, and Chu [19] provides qualitative information as to how increasing the sampling time of the INDI controller helps to increase stability margins when faced with uncertainty, slow actuators, high system gain and delayed measurements, it does not provide strict conditions regarding the stability of the INDI controller. A new analysis would be needed for each new system considered. It is also limited to Single-Input and Single-Output (SISO) systems.

Work by Huang et al. [21] fills this gap by providing valuable insights into how to quantify and generalize the robustness of the INDI controllers against uncertainty for SISO and Multi-Input and Multi-Output (MIMO) systems. By analyzing the INDI controller as a time-delay system and reformulating this system as neutral functional differential equations (refer to Huang et al. [21] for full development), necessary conditions for stability can be obtained. For a SISO system without actuator, stability is guaranteed for these specific conditions:

$$0.5 < \lambda < \frac{1}{\beta\tau} \quad (8.8)$$

where:

$$\beta = \left. \frac{\partial f(x,u)}{\partial x} \right|_{\substack{x=x_0 \\ u=u_0}}$$

$\lambda = \hat{G}G^{-1}$ = Control Effectiveness Uncertainty

\hat{G} = Control Effectiveness Estimation

τ = Controller Sample Time (s)

Generally, the upper bound for the uncertainty is much higher than the lower bound if the sample time τ of the controller is small. This confirms Veld, Van Kampen, and Chu [19] findings from Figure 8.2. Equation 8.8 could also be potentially used to guide the sampling time selection to guarantee uncertainty margins. Additionally, this finding could help guarantee stability with uncertainty, while historically determination required simulation or experimentation [19, 16].

For a MIMO system, a similar method can be used, where the system can be decoupled in parallel SISO systems. In the MIMO case, the condition for stability is defined as:

$$\operatorname{Re}(\lambda_i) > 0.5 \quad (8.9)$$

where:

$$\lambda_i = \text{Eigenvalues of } \hat{G}G^{-1}$$

No upper limit for uncertainty is provided by Huang et al. [21], although it would seem like the procedure used for the SISO system could be re-used on each decoupled system and then selecting the lowest uncertainty allowable. It would, however, require to have a good model of the system, which defeats the initial purpose of INDI, that aims to be less model-dependent.

The MIMO conditions for stability can be even more relaxed when adding actuators. It appears that the actuators act as a damper to the controller's action and damp out instabilities generated by the INDI controller trying to overcompensate. Using a first order actuator model ($A(s) = \frac{1}{\tau_a s + 1}$), the critical uncertainty allowed before instability can be lowered to [21]:

$$\lambda_i > \frac{6\tau_a\tau - 2\tau^2 + 5\tau^2\tau_a k_p - \tau^3 k_p + \tau \sqrt{(\tau k_p + 2)^2 (\tau^2 + 6\tau_a\tau + 21\tau_a^2 - 2\tau^2\tau_a k_p)}}{12(\tau^2\tau_a k_p + 2\tau\tau_a + \tau_a^2)} \quad (8.10)$$

where:

τ = Sample Time of INDI Controller

τ_a = Time Constant of Actuator

k_p = Linear Controller Gain

The mathematical developments presented in the last section show that the INDI controller is highly robust to control effectiveness uncertainty conditions and that these limit can be quantified theoretically. However, the work by Veld, Van Kampen, and Chu [19] and Huang et al. [21] both lack experimental validation of the limits they propose. Additional time delay induced by filtering is not included either, which would lower the robustness margins presented.

8.3. Airspeed Estimation

Airspeed estimation was briefly examined in subsection 7.2.4, where it was proposed to use other sensors on the vehicle to estimate airspeed. Different methods exist to estimate airspeed, with those most relevant for the VSQP being based on different first principles: dynamics based, wind triangle based and forces based. A summary of these methods is presented in Table 8.1.

8.3.1. Dynamics Based

Control effectiveness for the VSQP was developed in subsection 8.1.1 as a function of airspeed squared. Control effectiveness links the change in state derivative per variation of the control input. If the control input and state derivative are measured, it is possible to infer the control effectiveness of the vehicle and to estimate airspeed.

Least square estimation is commonly used with flight test data when control effectiveness cannot be easily estimated using analytical methods [53, 6]. The vehicle can be excited using a doublet, a common input used for system identification, which has the advantage of introducing little deviations in the flight path, as actuator deflection is symmetric [53]. Most methods estimate control effectiveness after flight tests have occurred (offline). Incorporating a control effectiveness estimation while in flight

Method	Advantages	Disadvantages	Knowledge Gap
Control Effectiveness Estimation	-Requires no additional sensor	-Complex -Computationally Heavy Low Estimation Rate	-Perform online control effectiveness estimation
Wind Triangle Model-Dependent	-High Precision	-Complex -Requires model of VSQP	-Model of VSQP for whole flight envelope
Wind Triangle Model-Independent	-Does not require model of VSQP	-Requires angle of attack and sideslip data -Dependent on precise sensor reading	-Effect of using angle of attack and slideslip estimation on airspeed precision
Lift Based	-Simple	-Requires lift parameters -Requires angle of attack data	-Precise Lift Model of VSQP for whole flight envelope -Effect of using angle of attack and slideslip estimation on airspeed precision
Drag/Propulsive Power Based	-Simple	-Requires drag and propulsion power parameters -Requires angle of attack data	-Precise Drag Model of VSQP for whole flight envelope -Effect of using angle of attack and slideslip estimation on airspeed precision

Table 8.1: Summary of Airspeed Estimation Methods

presents challenges. As the estimation of the control effectiveness requires to inject a doublet and record the response of the aircraft, the airspeed estimation rate is limited. Ideally, the controller must momentarily stop stabilizing the aircraft to inject the doublet. The controller must be robust enough to recover from the momentary stabilization pause, which is not guaranteed if the airspeed estimation is irregular, which brings imprecision. Additionally, the control effectiveness estimation method must be completed using the limited online computational power on the vehicle. Finally, noise in sensors and lag in actuators must be filtered and accounted for to obtain a precise estimation [10].

8.3.2. Wind Triangle Based

The ground speed of an aircraft v_g is the vector sum of airspeed v_a and wind speed v_w :

$$\vec{v}_g = \vec{v}_a + \vec{v}_w \quad (8.11)$$

At the simplest level, airspeed could be estimated if the wind speed and direction were known, as ground speed can be measured from the IMU and GNSS. Using the cosinus rule for triangles (more easily visualized with Figure 8.3), the following relationship can be exploited:

$$v_a^2 = v_w^2 + v_g^2 - 2v_g v_w \cos(\psi_w - \psi_g) \quad (8.12)$$

where:

ψ_g = Heading of the aircraft

ψ_w = Wind Direction (points in the direction it blows)

Estimating the wind speed can be challenging as it evolves throughout the flight of the vehicle. Lie [49] uses a cascaded Extended Kalman Filter (EKF) estimator architecture supported by a linearized model of the vehicle, illustrated in Figure 8.4. The first filter estimates the attitude and ground speed of the aircraft from the GNSS and IMU. The role of the second filter is to obtain the airspeed, angle of attack and sideslip angle using the output from the first filter as a measurement update and using the aircraft's linearized model for its time update. Test flights with the estimator on a 5 kg fixed wing vehicle flying at 21 m s^{-1} led to a 2 m s^{-1} 3σ error (three standard deviations or 93.3% of estimations fall within this range). In 45° turns, the estimator does not perform well as it is out of its trim point, with airspeed overestimated by $5\text{-}6 \text{ m s}^{-1}$. The precision of the air data estimates is dependent on the trim airspeed used to linearize the model. As the filter cannot handle airspeed deviations from the trim airspeed, the author mentions that linear model scheduling with the estimated airspeed would be required to obtain precision in a wide airspeed band.

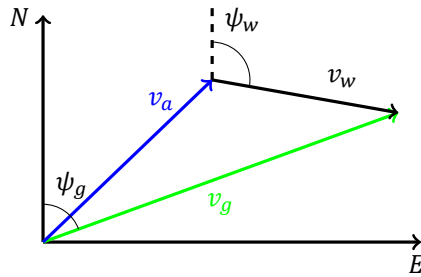


Figure 8.3: Wind Triangle

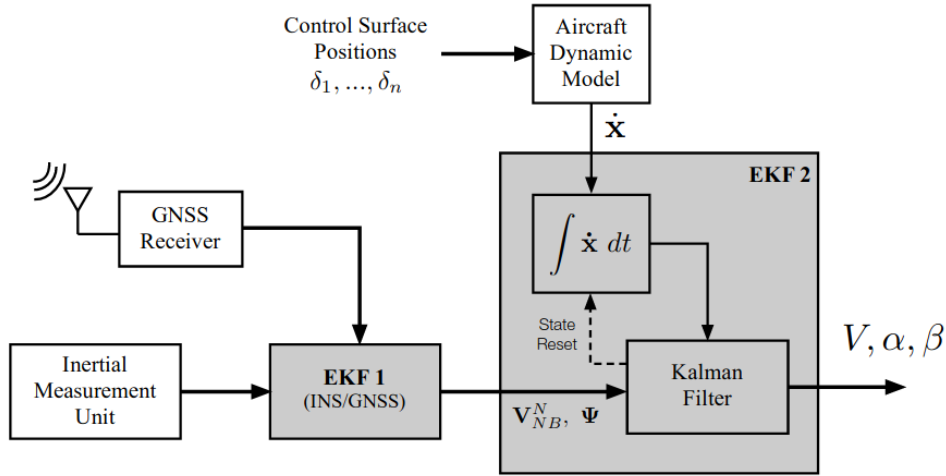


Figure 8.4: Dual EKF Architecture with Aircraft Dynamic Model [49]

To circumvent this, Rhudy et al. [54] use a model-independent fusion algorithm of IMU acceleration, gyroscopes angular rates, GNSS velocities, sideslip and angle of attack based on kinematics equations. The following state estimation vector, input vector and output vector are used:

$$\begin{aligned}\dot{\mathbf{x}}(t) &= [u(t) \quad v(t) \quad w(t) \quad \phi(t) \quad \theta(t) \quad \psi(t) \quad \mu_x(t) \quad \mu_y(t) \quad \mu_z(t)]^T \\ \mathbf{u}(t) &= [a_x(t) \quad a_y(t) \quad a_z(t) \quad p(t) \quad q(t) \quad r(t)]^T \\ \mathbf{y}(t) &= [V_x(t) \quad V_y(t) \quad V_z(t) \quad \alpha(t) \quad \beta(t)]^T\end{aligned}\tag{8.13}$$

where:

- u, v, w = Velocity in the Body Frame
- ϕ, θ, ψ = Attitude
- μ_x, μ_y, μ_z = Wind Velocity in Earth Fixed Frame
- p, q, r = Angular Rates Measured by Gyroscopes
- a_x, a_y, a_z = Accelerations Measured by Accelerometers
- V_x, V_y, V_z = Velocity in Earth Fixed Frame

The state derivatives are defined by Equation 8.14 to 8.16:

$$\begin{bmatrix} \dot{u}(t) \\ \dot{v}(t) \\ \dot{w}(t) \end{bmatrix} = \begin{bmatrix} 0 & -w(t) & v(t) \\ w(t) & 0 & -u(t) \\ -v(t) & u(t) & 0 \end{bmatrix} \left(\begin{bmatrix} p(t) \\ q(t) \\ r(t) \end{bmatrix}^{IMU} + \mathbf{w}^\omega(t) \right) + \mathbf{DCM}(\phi, \theta, \psi)^T \begin{bmatrix} 0 \\ 0 \\ g \end{bmatrix} + \begin{bmatrix} a_x(t) \\ a_y(t) \\ a_z(t) \end{bmatrix}^{IMU} + \mathbf{w}^a(t)\tag{8.14}$$

$$\begin{bmatrix} \dot{\phi}(t) \\ \dot{\theta}(t) \\ \dot{\psi}(t) \end{bmatrix} = \begin{bmatrix} 1 & \sin \phi(t) \tan \theta(t) & \cos \phi(t) \tan \theta(t) \\ 0 & \cos \phi(t) & -\sin \phi(t) \\ 0 & \sin \phi(t) \sec \theta(t) & \cos \phi(t) \sec \theta(t) \end{bmatrix} \times \left(\begin{bmatrix} p(t) \\ q(t) \\ r(t) \end{bmatrix}^{IMU} + \mathbf{w}^\omega(t) \right) \quad (8.15)$$

$$\begin{bmatrix} \dot{\mu}_x(t) \\ \dot{\mu}_y(t) \\ \dot{\mu}_z(t) \end{bmatrix} = \mathbf{w}^\mu(t) \quad (8.16)$$

where:

DCM = Direction Cosine Matrix to Convert from Body Axes and Earth-Fixed Axes

\mathbf{w}^α = Gaussian Process Noise of Accelerometers

\mathbf{w}^ω = Gaussian Process Noise of Gyroscopes

\mathbf{w}^μ = Gaussian Process Noise of Wind Velocity, Modeled as a Random Walk Process

Since they are derived from kinematics, the only uncertainty (process noise) in the state equations comes from the gyroscopes and accelerometers sensor noise. This results in an estimator that is not dependent on model specific parameters. The covariance matrices related to the sensors needs be calculated for every vehicle, but can be easily obtained using flight test data [54]. The GNSS velocities, angle of attack and sideslip vane measurements are used to update the output vector using Equation 8.17 and 8.18.

$$\begin{bmatrix} V_x(t) \\ V_y(t) \\ V_z(t) \end{bmatrix} = \mathbf{DCM}(\phi(t), \theta(t), \psi(t)) \begin{bmatrix} u(t) \\ v(t) \\ w(t) \end{bmatrix} + \begin{bmatrix} \mu_x(t) \\ \mu_y(t) \\ \mu_z(t) \end{bmatrix} \quad (8.17)$$

$$\begin{aligned} \alpha(t) &= \tan^{-1} \left(\frac{w(t)}{u(t)} \right) \\ \beta(t) &= \sin^{-1} \left(\frac{v(t)}{\sqrt{u(t)^2 + v(t)^2 + w(t)^2}} \right) \end{aligned} \quad (8.18)$$

Flights tests with two different aircraft led to an average error of 0.2 m s^{-1} and average standard deviation error of 1.7 m s^{-1} when cruising at 25 m s^{-1} , with turns and level flight. The precision of airspeed estimation is independent of the attitude of the aircraft, but the author mentions correlation between the attitude precision and the airspeed estimation, as the attitude is used to project the Earth Frame measured airspeed.

The VSQP is currently not equipped with an angle of attack or sideslip vane. Additionally, if it was present, the readings would be influenced by the substantial downwash caused by the hover motors when they are operating. Alternative methods to estimate these states need to be explored. Sideslip can be estimated using side acceleration as explained in section 5.2. In steady flight with wings leveled without sideslip, the angle of attack can be estimated as the difference between the pitch angle and climb angle [55]:

$$\alpha = \theta - \gamma \quad (8.19)$$

Knowing the definition of the climb angle ($V_z = V_a \sin \gamma$) and neglecting vertical wind, the angle of attack can be estimated for wings level flight:

$$\alpha = \theta - \arcsin \frac{w}{\sqrt{u^2 + v^2 + w^2}} \quad (8.20)$$

This method, although only valid in steady wings level flight, should be sufficient to obtain an estimate of the angle of attack. The precision of this estimation and its effect on the airspeed estimation is unknown and would need to be evaluated.

8.3.3. Forces Based

Section 8.3.2 reviewed methods that were based on estimating the wind and using the wind triangle in order to estimate the airspeed. It would be advantageous to skip this step and to estimate the airspeed based on airspeed-dependent phenomena occurring directly on the vehicle.

Lift and drag are linear to the square of airspeed [55]. If there was a way to estimate the forces acting on the aircraft, by knowing the vehicle's parameters, airspeed could be obtained. This is the strategy followed by Youn et al. [56], that considers lift generated by the wing and the horizontal stabilizer. Using Newton's Second law on the z axis and assuming a small angle of attack and pitch rate, airspeed can be estimated:

$$\frac{1}{2}\rho V_a^2 S (C_{L0} + \alpha C_{L\alpha} + \delta_e C_{L\delta_e}) = ma_z \rightarrow \tilde{V}_a \approx \sqrt{-\frac{2ma_z}{\rho S (C_{L0} + \alpha C_{L\alpha} + \delta_e C_{L\delta_e})}} \quad (8.21)$$

where:

C_{L0} = Lift Coefficient at 0 Angle of Attack

$C_{L\alpha}$ = Lift Coefficient as a Function of Angle of Attack

δ_e = Elevator Deflection

$C_{L\delta_e}$ = Lift Coefficient of Horizontal Stabilizer as a Function of Elevator Deflection

$$\begin{aligned} \dot{V}_a = & a_x \cos \alpha \cos \beta + a_y \sin \beta + a_z \sin \alpha \cos \beta \\ & + \mathbf{g}(-\cos \alpha \cos \beta \sin \theta + \sin \beta \sin \phi \cos \theta) \\ & + \sin \alpha \cos \beta \cos \phi \cos \theta \end{aligned} \quad (8.22)$$

Knowing the dynamic change of airspeed with Equation 8.22, an EKF can be built, with the estimated airspeed from Equation 8.21 acting as a measurement. If the sideslip angle is not available, it can be assumed to be zero, with no measurable difference in estimation performance [56]. The author also proposes a complementary formulation that performs similarly to the EKF estimator with significant lower computational requirements, which makes it highly suitable for an application on the VSQP. With an angle of attack vane, the mean airspeed error is 2 m s^{-1} for flight at 25 m s^{-1} . This method is attractive for the VSQP as the lift parameters required can be easily obtained using wind tunnel data. The lift model would require modifications to take into account the hover motor lift forces. The lift coefficients would need to be scheduled depending on the skew angle of the wing, data that is available as well. Angle of attack can be estimated using the same method as in subsection 8.3.2 or could be set to the pitch angle but would risk underestimating the airspeed in descents.

A similar method can be applied for forces acting in the x -axis of the aircraft: drag and thrust [28]. Thrust can be estimated using wind tunnel data linking the thrust force to the command sent to the motor. Hansen and Blanke [28] implemented this method to detect pitot tube faults on a UAV but does not provide its precision. It could be argued that the lift and the drag should be expected to have similar precision as they are based on the same sensor: accelerometers and angle of attack estimation. The precision of the model parameters in both these methods is vital in order to obtain high precision in the airspeed estimation.

8.4. Pitot Tube Fault Detection Methods

In order to switch the airspeed data from the pitot tube to an alternative estimation method, the pitot tube failure must be identified. This section addresses a few methods suggested by the literature to identify this specific failure case. As detection is not the primary goal of this research, the following review is limited in its scope.

If the failure case exhibits a characteristic failure pattern, this pattern can be used to identify the fault. For water blockage, Sun and Gebre-Egziabher [3] assumes that the pitot tube airspeed reading will reduce at a constant rate after a fault. Looking at a receding horizon, they identify any constant airspeed reduction as a fault. The main drawback is that if any other type of failure occurs, the detection will fail.

If the airspeed estimators are used in parallel to the pitot tube during flight, residuals i.e the difference between the pitot tube airspeed and the estimator's airspeed, can be calculated. Once these residuals are calculated, deterministic or stochastic methods can be used to detect failures [23, 3]. Hansen

and Blanke [28] proposes to calculate three different residuals: pitot vs GNSS based airspeed, pitot vs drag/propulsive power based airspeed, GNSS based airspeed vs drag/propulsive power based airspeed. Using these three different estimators, a failure of any of these airspeed sources can be identified. For example, if the pitot vs GNSS based airspeed shows high residuals but GNSS based airspeed vs drag/propulsive power based airspeed does not, the pitot tube is the cause of the fault.

Summary

Airspeed squared is used in both the stabilization (control surface effectiveness) and guidance (lift model) control effectiveness matrix, leading to an amplification of airspeed uncertainty. The wing skew angle is scheduled using airspeed. A safer transition with increased control effectiveness could be assured by reducing the weight on thrust, inducing a higher speed transition.

INDI is shown to be highly robust to uncertainty, with a higher robustness to control effectiveness overestimation than underestimation. These limits were quantified for both SISO and MIMO systems based on the sample time of the controller and on the eigenvalues of the control effectiveness uncertainty. However, the theoretical findings lack experimental validation.

Different methods can be used to estimate airspeed. Online control effectiveness estimation can be used to derive the airspeed but would require significant calculations to be performed online. The wing triangle can be used to estimate the vehicle airspeed knowing ground speed and an estimation of wind speed. A model-independent method is most promising as it is only based on kinematics equations but requires angle of attack and sideslip data. An estimation scheme for this information is provided, but its effect on the airspeed estimation is unknown. Forces based methods can also be used to estimate airspeed by knowing the lift or drag and propulsion parameters of the vehicle and the angle of attack of the vehicle. A precise model of these forces (induced by the wing, hover motors and stabilator) would be required for the VSQP in all its flight envelope in addition to a angle of attack estimation. All those methods can be implemented on the VSQP and compared to better understand in which conditions they perform better. Ultimately, if different methods lead to a precise airspeed estimation, it might be possible to envision removing the pitot tube altogether to simplify the design.

Limited pitot tube detection methods failure are listed. They rely on the use of residuals to detect a difference between the pitot tube reading and the airspeed estimation data.

9

Project Plan

This chapter offers an overview of the research work and what are the next steps after this literature review. The identified knowledge gaps are used to generate research questions in section 9.1. The methodology that is to be used to answer these questions is explained in section 9.2. Finally, the plan for the whole thesis is presented in section 9.3.

9.1. Updated Research Objective

Following the FMEA, the pitot tube was selected for further examination. Accordingly, the research goal is now:

Research Objective

To obtain pitot-tube free airspeed estimation and provide pitot tube failure detection capabilities for the Variable Skew Quad Plane (VSQP) in its whole flight envelope, using existing conventional sensors.

The literature review has highlighted significant scientific work on each research question relating to the pitot tube failure, with knowledge gaps mostly centered on the unique configuration of the VSQP. Multiple airspeed estimation methods exist for fixed wing aircraft. Their potential application on a hybrid vehicle similar to the VSQP is a significant knowledge gap. For model-dependent methods, the model of the vehicle needs to be adapted to account for both VSQP's configurations. Additionally, most methods require angle of attack and sideslip data. An estimation is provided using acceleration and rate of climb, but its precision and its effect on the overall airspeed precision are still open problems. Detection of a failure is an integral part of building a fault tolerant system.

9.2. Methodology

In order to answer the research questions proposed in the last section, the airspeed estimators will first be modeled, then simulated and finally tested experimentally. To limit risk, the method used allows to address several research questions using simulations, with practical testing for validating results.

9.2.1. Modeling and Simulation

Modeling and simulation will be completed using Matlab/Simulink. Its graphical "block-like" interface increases the speed at which systems can be modeled and tested. The main limitation of Matlab/Simulink is its relatively "closed" architecture and its high computational load. It is not feasible to run Matlab/Simulink code directly on MAVs. However, there are conversion libraries ¹ for converting from a Simulink file to C-code. The conversion can also be completed manually if required.

¹<https://nl.mathworks.com/help/dsp/ug/generate-c-code-from-simulink-model.html>

The airspeed estimators can first be modeled in Simulink. Verification of the implementation of the estimators can be completed using ideal test scenarios where the outcome is known. For model-dependent estimators, the different vehicle coefficients (aerodynamic, control effectiveness, etc.) can be verified using wind-tunnel test data already gathered by De Ponti [10] for the prototype aircraft and by static tests completed in the OJF at the TU Delft in November 2022 with the new VSQP. For parameters requiring dynamic flight of the aircraft, verification can be achieved by using flight test data. If additional verification needs to be completed, the OJF can be used in March, during a time slot reserved by the MAVLab Team.

Validation of the simulation can be performed using flight test data. Flight states of the aircraft (velocity, accelerations, angular rates, attitude, airspeed, actuator commands, etc.) extracted from existing flight logs can be used as an input to the estimators. The airspeed estimation can be compared to the real airspeed measured by the pitot in flight. A broad overview of the performance of each type of estimator will be obtained depending on the flight conditions and their sensitivity to parameters explored.

9.2.2. Experimentation

Simulation can be a quick and effective way to rapidly iterate on a design. The experimental tests aim to validate the results obtained in the simulations, as certain phenomena might not have been modeled precisely or accurately. Additionally, an experimental set-up can help verify phenomena not identified earlier or that could not be modelled. Real life implementation considerations (sampling rate, computational load, memory usage, etc.) might also require re-design or optimization of certain concepts

To test experimentally, the estimators modeled in Simulink will need to be implemented on the VSQP. The Paparazzi open source autopilot software² is used on the VSQP for control (guidance and stabilization) and managing the vehicle (telemetry, logging, etc.). The estimators will need to be converted into C or C++ code used on Paparazzi. Paparazzi was selected due to the MAVLab's considerable experience using it and developing new modules such as a custom one for the VSQP.

Flights tests are to be completed at Valkenburg, a facility without obstacles that can allow validation of the VSQP in its whole flight envelope. Flights at Valkenburg require the use of a trained pilot and is dependent on weather. Flight tests could also be completed in the OJF although they could only test level flight and transition. Due to the limited test section, the aircraft cannot maneuver vertically or laterally. Additionally, the GNSS measurement would need to be simulated using an Optitrack positioning system³.

During flight tests, the estimators could first be running in background to reduce risk if the airspeed estimation diverges from the real airspeed. Once sufficient confidence in the algorithms are achieved, they could be switched on as a source of airspeed data for the whole vehicle. If any error in the estimation occurs, the airspeed source can be reverted back to the pitot. Ideally, the vehicle would be equipped with an angle of attack and sidelip vane in order to measure the real airspeed of the aircraft instead of the x-component of the airspeed.

9.3. Project Planning

This section elaborates on the different work packages that structure the planning of this project and how scheduling limitations were taken into account.

9.3.1. Limitations

The project planning was initiated by listing all the potential limitations that it could face. It allows to have a number of milestones as "hard" milestones. They are structured in different categories:

- Administrative Limitations
 - Due to administrative reasons, the thesis must be completed before the start of the 2023-2024 academic year

²<https://github.com/paparazzi/paparazzi/>.

³<https://optitrack.com/>

- Finding a defense committee during the summer break is not possible (between mid-July and end of August)
- Facility Limitations
 - If additional verification data is required with the Open Jet Facility, the only current availability is in March.
 - The Open Jet Facility requires training to operate it
 - The Cyberzoo is available all year, but is used more in Q3. Training will be required before using it.
 - Flights tests at Valkenburg are dependent on weather (wind and precipitations)
- Physical Limitations
 - A crash after an experimental flight could lead to broken part and require more than a week for repairs. High-risk situations or crashing should be avoided

Using these limitations, the main milestones of the thesis are set. Therefore, the defense must occur before mid-July.

9.3.2. Work Packages

To better structure the work during the thesis, work is structured using work packages. Each work package deals with a specific phase of the work:

- Literature review
- Modeling
- Simulation
- Experimentation
- Thesis writing

Each work package is divided in tasks. Figure 9.1 presents a Gantt Chart with the general schedule of each work package. The work has a scheduled duration of 9 months with 2 months set for the literature review. The schedule is arranged such as that experimental tests will take place at the mid-term review. This will help determine if research is addressing the initial research questions.

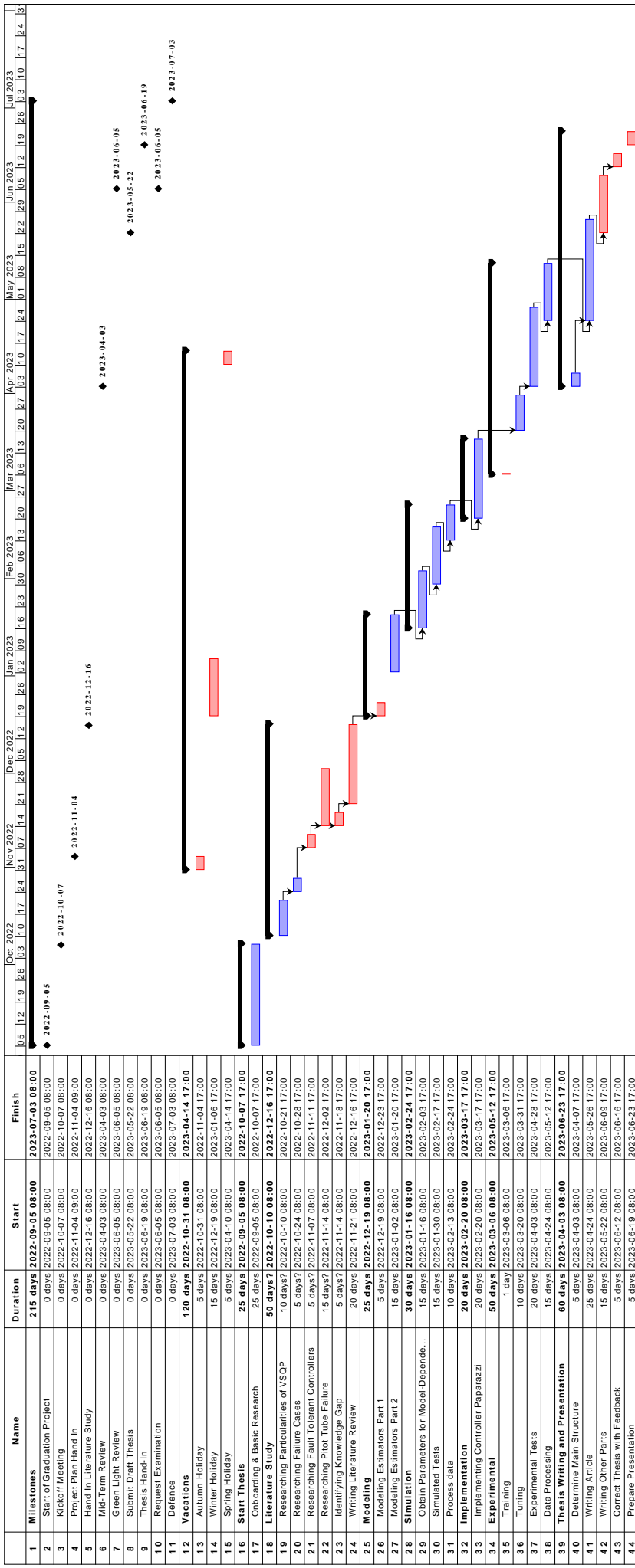


Figure 9.1: Gantt Chart of Project Plan for VSQP as of December 15th 2023

10

Conclusion

The initial goal of this thesis was to improve safety of the Variable Skew Quad Plane (VSQP) using fault tolerant control methods. First, the distinct feature of the hybrid VSQP were analyzed to identify potential critical flight phases or components. It shows similarity to an oblique wing, strong coupling between axis, varying control effectiveness of actuators and non-symmetric forces occurs during transition, when the wing skew angle is changed. These characteristics make the transition phase of the vehicle hard to model and to control. Transition is therefore a critical flight phase for failures. Incremental Nonlinear Dynamic Inversion (INDI) is used in a cascaded architecture to control the VSQP, as it requires limited model knowledge. The incremental nature of INDI leads to high robustness compared to other control methods such as aProportional Integral and Derivative (PID) controller, which can potentially be used as an advantage for future Fault Tolerant Control (FTC).

Different FTC methods exist to maintain stability after a fault. It was concluded that active FTC is well suited for VSQP, a vehicle with existing but limited redundancy, and tight performance margins in transition. By detecting and identifying a fault, the controller can change control allocation or adapt gains and saturation limits to maintain the vehicle within a stable flight envelope. The main drawback of the method is the high dependency on detection and high computational load which might limit the use of complex algorithms.

A Failure Mode and Effects Analysis (FMEA) lead to the identification of the four most critical failure modes for the VSQP: complete rotor loss, stuck stabilator, wing angle sensor fault and pitot tube failure. The rotor loss failure case is well documented for small quadcopters but data is lacking for bigger vehicles with a tail. The literature proposes the use of a new rotating equilibrium position in which the quadcopter can maintain stability after a rotor loss. The addition of flight surfaces change the ability of the vehicle to reach and maintain this new state. Preliminary calculations lead to believe that the VSQP can reach the equilibrium state if the fault detection time and motor spool up time are quick. Even if it was not selected for further research as part of this work, the lack of documentation for a complete rotor loss on a quadplane configuration like the VSQP makes it an interesting topic to investigate further. The stuck stabilator and wing angle sensor fault both have documented solutions that do not warrant additional research effort, but they could require implementation effort on the VSQP.

The pitot tube failure is selected for further research as it presents the most severe effects on the controller and being particularly prone to water blockage on small Unmanned Air Vehicle (UAV)s. Airspeed error is amplified in both the stabilization and guidance control effectiveness matrix calculations when calculating the lift generated by the control surfaces and wing. These highlight the importance of obtaining a precise airspeed estimation that is independent of the pitot tube. The INDI controller's robustness can partially compensate for the estimation error. Theoretical limits for underestimating or overestimating the control effectiveness are available in the literature, but lack experimental validation.

Airspeed estimation is well covered for airliners and fixed wing aircraft but is limited for hybrid vehicles. The main challenges with these vehicles is the difficulty to obtain a precise model and estimate airspeed in the whole flight envelope, from hover all the way to horizontal flight. For this reason, a model-

independent method is most promising as it only relies on kinematics. However, it requires angle of attack and sideslip angle readings, which can be estimated using other sensors, but with undefined precision. The propagation of this estimation error on airspeed estimation is not covered in the literature examined. Other methods based on estimating the forces acting on the aircraft show great promises as they require limited sensors and are simpler. A model of forces acting on the VSQP would be required to adapt these types of estimation algorithms to the VSQP. Again, angle of attack would need to be estimated. Ultimately, the estimation methods presented in the literature review should be implemented and compared to analyze which perform best on the VSQP. In a case where airspeed estimation is precise enough to allow flight within the whole flight envelope, complete removal of the pitot tube could be envisioned to simplify the design of the vehicle.

Following the literature review, an updated research goal was formulated to drive the next steps of the thesis work. Its goals are develop a synthetic air data system and pitot tube detection for the VSQP. Different airspeed estimation methods are to be adjusted and merged for use on the VSQP and their performance are to be evaluated.

Bibliography

- [1] C. De Wagter et al. "The NederDrone: A hybrid lift, hybrid energy hydrogen UAV". In: *International Journal of Hydrogen Energy* 46.29 (Apr. 2021), pp. 16003–16018. ISSN: 0360-3199. DOI: 10.1016/J.IJHYDENE.2021.02.053.
- [2] R.P.G Collinson. *Introduction to Avionics Systems*. 3rd. New York: Springer, 2011, pp. 217–230.
- [3] Kerry Sun and Demoz Gebre-Egziabher. "Air data fault detection and isolation for small UAS using integrity monitoring framework". In: *Institute of Navigation* 68.3 (2021), pp. 577–600. DOI: 10.1002/navi.440.
- [4] John Downer. *When failure is an option : redundancy, reliability and regulation in complex technical systems*. London: Centre for Analysis of Risk, Regulation at the London School of Economics, and Political Science, 2009, p. 24. ISBN: 9780853283959.
- [5] Adnan S. Saeed et al. "A survey of hybrid Unmanned Aerial Vehicles". In: *Progress in Aerospace Sciences* 98 (Apr. 2018), pp. 91–105. ISSN: 03760421. DOI: 10.1016/j.paerosci.2018.03.007.
- [6] Ewoud J. J. Smeur, Murat Bronz, and Guido C. H. E. de Croon. "Incremental Control and Guidance of Hybrid Aircraft Applied to a Tailsitter UAV". In: *Journal of Guidance, Control, and Dynamics: devoted to the technology of dynamics and control* 43.2 (Feb. 2018). DOI: 10.2514/1.G004520. URL: <http://arxiv.org/abs/1802.00714>.
- [7] Bin Xian and Wei Hao. "Nonlinear Robust Fault-Tolerant Control of the Tilt Trirotor UAV under Rear Servo's Stuck Fault: Theory and Experiments". In: *IEEE Transactions on Industrial Informatics* 15.4 (Apr. 2019), pp. 2158–2166. ISSN: 15513203. DOI: 10.1109/TII.2018.2858143.
- [8] Rumit Kumar et al. "Reconfigurable fault-tolerant tilt-rotor quadcopter system". In: *ASME 2018 Dynamic Systems and Control Conference, DSCC 2018*. Vol. 3. American Society of Mechanical Engineers (ASME), 2018. ISBN: 9780791851913. DOI: 10.1115/DSCC2018-9197.
- [9] Xuerui Wang and Sihao Sun. "Incremental fault-tolerant control for a hybrid quad-plane UAV subjected to a complete rotor loss". In: *Aerospace Science and Technology* 125 (June 2022), p. 107105. ISSN: 1270-9638. DOI: 10.1016/J.AST.2021.107105.
- [10] Tomaso Maria Luigi De Ponti. *Incremental Nonlinear Dynamic Inversion Controller for a Variable Skew Quad Plane*. Delft: Master's Thesis, 2022.
- [11] D C Van Wijngaarden and B D W Remes. "INDI Control for the Oblique Wing-Quad Plane Drone". In: *International Micro Air Vehicle Conference*. Delft, 2022, pp. 119–126.
- [12] Enrico Petritoli, Fabio Leccese, and Lorenzo Ciani. "Reliability assessment of UAV systems". In: *4th IEEE International Workshop on Metrology for AeroSpace, MetroAeroSpace 2017 - Proceedings*. Institute of Electrical and Electronics Engineers Inc., Aug. 2017, pp. 266–270. ISBN: 9781509042340. DOI: 10.1109/MetroAeroSpace.2017.7999577.
- [13] Michael J. Hirschberg, David M. Hart, and Thomas J. Beutner. "A summary of a half-century of oblique wing research". In: *Collection of Technical Papers - 45th AIAA Aerospace Sciences Meeting*. Vol. 3. 2007, pp. 1781–1815. ISBN: 1563478900. DOI: 10.2514/6.2007-150.
- [14] Lixin Wang, Zijian Xu, and Ting Yue. "Dynamic characteristics analysis and flight control design for oblique wing aircraft". In: *Chinese Journal of Aeronautics* 29.6 (Dec. 2016), pp. 1664–1672. ISSN: 1000-9361. DOI: 10.1016/J.CJA.2016.10.010.
- [15] I. KROO. "The aerodynamic design of oblique wing aircraft". In: American Institute of Aeronautics and Astronautics (AIAA), Oct. 1986. DOI: 10.2514/6.1986-2624.
- [16] S. Sieberling, Q. P. Chu, and J. A. Mulder. "Robust flight control using incremental nonlinear dynamic inversion and angular acceleration prediction". In: *Journal of Guidance, Control, and Dynamics* 33.6 (2010), pp. 1732–1742. ISSN: 15333884. DOI: 10.2514/1.49978.

- [17] Ewoud J.J. Smeur, Qiping Chu, and Guido C.H.E. De Croon. "Adaptive incremental nonlinear dynamic inversion for attitude control of micro air vehicles". In: *Journal of Guidance, Control, and Dynamics* 39.3 (2016), pp. 450–461. ISSN: 15333884. DOI: 10.2514/1.G001490.
- [18] Ewoud J. J. Smeur, Guido C. H. E. de Croon, and Qiping Chu. "Cascaded Incremental Nonlinear Dynamic Inversion Control for MAV Disturbance Rejection". In: *Control Engineering Practice* 73 (Jan. 2018), pp. 79–90. DOI: 10.1016/j.conengprac.2018.01.003. URL: <http://arxiv.org/abs/1701.07254>.
- [19] R. C. van't Veld, E. Van Kampen, and Q. Ping Chu. "Stability and robustness analysis and improvements for incremental nonlinear dynamic inversion control". In: *AIAA Guidance, Navigation, and Control Conference, 2018*. Vol. 0. 210039. American Institute of Aeronautics and Astronautics Inc, AIAA, Jan. 2018. ISBN: 9781624105265. DOI: 10.2514/6.2018-1127.
- [20] Ewoud J.J. Smeur, Guido C.H.E. De Croon, and Qiping Chu. "Gust disturbance alleviation with incremental nonlinear dynamic inversion". In: *IEEE International Conference on Intelligent Robots and Systems*. Vol. 2016-November. Institute of Electrical and Electronics Engineers Inc., Nov. 2016, pp. 5626–5631. ISBN: 9781509037629. DOI: 10.1109/IROS.2016.7759827.
- [21] Yingzhi Huang et al. "Time-Delay Margin and Robustness of Incremental Nonlinear Dynamic Inversion Control". In: *Journal of Guidance, Control, and Dynamics* 45.2 (2022), pp. 394–404. ISSN: 15333884. DOI: 10.2514/1.G006024.
- [22] Xuerui Wang et al. "Stability analysis for incremental nonlinear dynamic inversion control". In: *Journal of Guidance, Control, and Dynamics* 42.5 (2019), pp. 1116–1129. ISSN: 15333884. DOI: 10.2514/1.G003791.
- [23] Zhiwei Gao, Carlo Cecati, and Steven X Ding. "A Survey of Fault Diagnosis and Fault-Tolerant Part I: Fault Diagnosis With Model-Based and Signal-Based Approaches". In: *IEEE Transactions on Industrial Electronics* 62.6 (2015), p. 3757. DOI: 10.1109/TIE.2015.2417501.
- [24] Alireza Abbaspour et al. "A Survey on Active Fault-Tolerant Control Systems". In: *Electronics* 2020, Vol. 9, Page 1513 9.9 (Sept. 2020), p. 1513. ISSN: 2079-9292. DOI: 10.3390/ELECTRONICS9091513. URL: <https://www.mdpi.com/2079-9292/9/9/1513>.
- [25] Hussein Hamadi. "Fault-tolerant control of a multirotor unmanned aerial vehicle under hardware and software failures". PhD thesis. Université de Technologie de Compiègne, 2020. URL: <https://tel.archives-ouvertes.fr/tel-03116827>.
- [26] Zhiwei Gao, Carlo Cecati, and Steven X. Ding. "A survey of fault diagnosis and fault-tolerant techniques-part II: Fault Diagnosis with Knowledge-Based and Hybrid/Active Approaches". In: *IEEE Transactions on Industrial Electronics* 62.6 (June 2015), pp. 3757–3767. ISSN: 02780046. DOI: 10.1109/TIE.2015.2417501.
- [27] Søren Hansen, Mogens Blanke, and Jens Adrian. "Diagnosis of UAV Pitot Tube Defects Using Statistical Change Detection". In: *IFAC Proceedings Volumes* 43.16 (Jan. 2010), pp. 485–490. ISSN: 1474-6670. DOI: 10.3182/20100906-3-IT-2019.00084.
- [28] Søren Hansen and Mogens Blanke. "Diagnosis of Airspeed Measurement Faults for Unmanned Aerial Vehicles". In: *IEEE Transactions on Aerospace and Electronic Systems* 50.1 (2014). DOI: 10.1109/TAES.2013.120420.
- [29] Youmin Zhang. "An Adaptive Fault-Tolerant Sliding Mode Control Allocation Scheme for Multirotor Helicopter Subject to Simultaneous Actuator Faults". In: *IEEE TRANSACTIONS ON INDUSTRIAL ELECTRONICS* 65.5 (2018). DOI: 10.1109/TIE.2017.2772153.
- [30] Alaeddin Bani Milhim, Youmin Zhang, and Camille Alain Rabbath. "Gain scheduling based PID controller for fault tolerant control of a quad-rotor UAV". In: *AIAA Infotech at Aerospace 2010* (2010). DOI: 10.2514/6.2010-3530.
- [31] G Ducard et al. "Evaluation of Reduction in the Performance of a Small UAV After an Aileron Failure for an Adaptive Guidance System". In: *American Control Conference*. New York: IEEE, July 2007.

- [32] Ibrahim Mizrak, Halim Alwi, and Christopher Edwards. "Fault Tolerant Control of a Quadplane UAV Using Sliding Modes". In: *2021 European Control Conference, ECC 2021* (2021), pp. 1699–1704. DOI: 10.23919/ECC54610.2021.9655032.
- [33] Fuyang Chen et al. "Robust Backstepping Sliding-Mode Control and Observer-Based Fault Estimation for a Quadrotor UAV; Robust Backstepping Sliding-Mode Control and Observer-Based Fault Estimation for a Quadrotor UAV". In: *IEEE Transactions on Industrial Electronics* 63.8 (2016). DOI: 10.1109/TIE.2016.2552151.
- [34] Peng Lu et al. "Aircraft fault-tolerant trajectory control using Incremental Nonlinear Dynamic Inversion". In: *Control Engineering Practice* 57 (Dec. 2016), pp. 126–141. ISSN: 09670661. DOI: 10.1016/j.conengprac.2016.09.010.
- [35] D.A. Joosten and J.M. Maciejowski. "MPC design for fault-tolerant flight control purposes based upon an existing output feedback controller". In: *IFAC Proceedings Volumes* 42.8 (Jan. 2009), pp. 253–258. ISSN: 1474-6670. DOI: 10.3182/20090630-4-ES-2003.00042.
- [36] Shawn Reimann et al. *UAV for Reliability*. Tech. rep. 2013.
- [37] Justin Fortna Murtha. *An Evidence Theoretic Approach to Design of Reliable Low-Cost UAVs*. Master's Thesis, 2009.
- [38] Paul Freeman and Gary J. Balas. "Actuation failure modes and effects analysis for a small UAV". In: *Proceedings of the American Control Conference*. Institute of Electrical and Electronics Engineers Inc., 2014, pp. 1292–1297. ISBN: 9781479932726. DOI: 10.1109/ACC.2014.6859482.
- [39] Quanterion. *Nonelectronic Parts Reliability Data Publication*. 2016th ed. 2016.
- [40] Dainius Udris, Domantas Bručas, and Raimondas Pomarnacki. "Reliability Improvement of Power Distribution System for UAV". In: *Electronics* 8.6 (2019), p. 636. DOI: 10.3390/electronics8060636. URL: www.mdpi.com/journal/electronics.
- [41] Remma Matsuda, Tatsuya Ibuki, and Mitsuji Sampei. "A Hoverability Analysis Method for Multirotor UAVs with a Case Study on Fault Tolerance". In: *2018 IEEE Conference on Decision and Control (CDC)*. 2018, pp. 4264–4269. ISBN: 9781538613955. DOI: 10.1109/CDC.2018.8619161.
- [42] Guang Xun Du et al. "Controllability analysis for multirotor helicopter rotor degradation and failure". In: *Journal of Guidance, Control, and Dynamics* 38.5 (2015), pp. 978–984. ISSN: 15333884. DOI: 10.2514/1.G000731.
- [43] Mueller W. Mark and D'Andrea Raffaello. "Stability and control of a quadrocopter despite the complete loss of one, two, or three propellers". In: *IEEE International Conference on Robotics and Automation*. IEEE, 2014. ISBN: 9781479936847.
- [44] Peng Lu and Erik-Jan van Kampen. "Active fault-tolerant control for quadrotors subjected to a complete rotor failure". In: *2015 IEEE/RSJ International Conference on Intelligent Robots and Systems (IROS)*. IEEE, 2015.
- [45] Chenxu Ke, Kai-Yuan Cai, and Quan Quan. "Uniform Fault-Tolerant Control of a Quadcopter With Rotor Failure". In: *IEEE/ASME Transactions on Mechatronics* (2022). DOI: 10.1109/TMECH.2022.3202804. URL: [https://doi.org/10.1109/TMECH.2022.3202804..](https://doi.org/10.1109/TMECH.2022.3202804)
- [46] Raghu Venkataraman et al. "Reliability assessment of actuator architectures for unmanned aircraft". In: *IFAC-PapersOnLine*. Vol. 28. 21. Sept. 2015, pp. 398–403. DOI: 10.1016/j.ifacol.2015.09.559.
- [47] Karl Frederik Prochazka and Gösta Stomberg. "Integral Sliding Mode based Model Reference FTC of an Over-Actuated Hybrid UAV using Online Control Allocation". In: *American Control Conference*. 2020. ISBN: 9781538682661.
- [48] Christer Ebbesson. *Rotary Position Sensors Comparative study of different rotary position sensors for electrical machines used in an hybrid electric vehicle application*. Tech. rep. 2011.
- [49] F. Adhika Pradipta Lie. "Synthetic Air Data Estimation". PhD thesis. University of Minnesota, Sept. 2014.

-
- [50] Omar Hazbon Alvarez. "Fault Tolerant Air Data System for Pitot Tube Failure". PhD thesis. Medelin: Universidad Pontificia Bolivariana, 2020.
 - [51] Sihao Sun et al. "Incremental Nonlinear Fault-Tolerant Control of a Quadrotor with Complete Loss of Two Opposing Rotors". In: *IEEE Transactions on Robotics* 37.1 (Feb. 2021), pp. 116–130. ISSN: 19410468. DOI: 10.1109/TRO.2020.3010626.
 - [52] Marcin Zugaj, Przemysław Bibik, and Mariusz Jacewicz. "UAV aircraft model for control system failures analysis". In: *Journal of Theoretical and Applied Mechanics (Poland)* 54.4 (2016), pp. 1405–1415. ISSN: 14292955. DOI: 10.15632/jtam-pl.54.4.1405.
 - [53] Christophe Wagter et al. "Modelling of a Hybrid UAV Using Test Flight Data". In: *International Micro Air Vehicle Conference*. 2014.
DOI: <https://doi.org/10.4233/uuid:2eed26cf-a7e8-4a6c-ac42-89a9608e4d2a>.
 - [54] Matthew B. Rhudy et al. "Aircraft model-independent airspeed estimation without pitot tube measurements". In: *IEEE Transactions on Aerospace and Electronic Systems* 51.3 (July 2015), pp. 1980–1995. ISSN: 00189251. DOI: 10.1109/TAES.2015.130631.
 - [55] Jan Roskam. *Airplane Flight Dynamics and Automatic Flight Controls Part 1*. Design, Analysis and Research Corporation, 2001. ISBN: 1-884885-17-9.
 - [56] Wonkeun Youn et al. "Model-Aided Synthetic Airspeed Estimation of UAVs for Analytical Redundancy". In: *IEEE Robotics and Automation Letters* 6.3 (July 2021), pp. 5841–5848. ISSN: 23773766. DOI: 10.1109/LRA.2021.3086428.

Appendices

A

Failure Mode Analysis

The FMEA was completed in an excel file, where failure modes are explored and detailed. A PDF version is presented in the following pages. The critical failures chosen are highlighted in green. Alternatively, a digital version is attached to this report¹.

Click the icon to access the full Excel File or download it to your computer²



¹A digital version of this document can be found on <https://repository.tudelft.nl>

²Make sure your PDF reader is compatible with attachments. Adobe Acrobat Reader and Foxit PDF Reader are.

Categories 1/2

Systems

Actuators	Sensors	Electronics
Rudder	Gyroscopes	ESC
Elevator	Accelerometers	Pixhawk
Ailerons	Wing angle	BECs
Wing rotation	Pitot tube	Cables
Pusher Motor	GPS	Battery
Hover Motor	Magnetometer	Servo

Phases of flight:
Quad Mode (vertical flight)
Transition Vertical --> Horizontal mode
Transition Horizontal --> Vertical mode
Plane Mode (horizontal flight)

Failures Modes

Possible Failure Modes for actuator [1]	Possible Failure Modes for Sensors	Possible Failure Modes for Electronics
Bias	Bias	Decreased Power Output/Input
Dynamics change	Increased noise	No Power Output/Input
Floating surface	No value / stuck at value	
Stuck in position		
Loss in Performance		

Venkataraman et al. [13] specifies that actuators can fail in different ways such as stuck, runaway, loss of efficiency, oscillatory, and mentions that the first three failure cases are more common when large loads are present on the actuator. Freeman and Balas [14] continues in the same vein while merging the "stuck" and "runaway" failure modes together, as a runaway is an extreme case of a stuck actuator (also called hardover).		Electronics failure modes were not evaluated as their effects will ultimately lead to sensor or actuator failure. It was deemed sufficient to look at actuator and sensor failures to account for electronics failure modes.
---	--	--

Categories 2/2

Structural	Communication
Wing	Herelink (control and datalink, both ways)
Vertical Stabilizer	GPS antenna
Horizontal Stabilizer	
Hover Motor Arm	
Fuselage	
Landing gear	
Whole Tail	

Possibles Failure Modes for Structural
Partial (flexible, still hanging)
Complete (ripped off)

Structural failures modes were not evaluated as the airframe is assumed to be built with sufficient safety margins and have a good record of reliability [3].	Communication failure modes were not evaluated as they were deemed out of the scope of the thesis, which is centered around control of the vehicle. It was assumed that the vehicle can accomplish all tasks autonomously.
---	--

Actuators 1/6

Component	Potential Failure Mode	Explanation	Probability	Potential Failure Effects
Rudder	Offset	The actual deflection of the control surface is offset from the required control surface deflection	Low	-Control surface not where controller think it is: undesired yaw moment
	Unpredicted Dynamics Change (gain, response)	The actuator has different dynamics than the modeled dynamics (for example: much slower actuator)	High	-transient response different, most probably slower
	Floating surface (stays neutral)	Control surface is no longer actuated or stays in neutral position.	High	Loss of aerodynamical directional control
	Stuck in position	Control surface holds a specific deflection angle and does not move, even when ordered to by the flight controller. Worst case scenario is a hardover, where the control surface is stuck in one of its extreme limit.	High	-Loss of aerodynamical directional control -Undesired Yaw Moment
Elevator	Offset	The actual deflection of the control surface is offset from the required control surface deflection	Low	-Control surface not where controller think it is: undesired pitch moment
	Unpredicted Dynamics Change (gain, response)	The actuator has different dynamics than the modeled dynamics (for example: much slower actuator)	High	-transient response different, most probably slower
	Floating surface (stays neutral)	Control surface is no longer actuated or stays in neutral position.	High	Partial loss of aerodynamical pitch control
	Stuck in position	Control surface holds a specific deflection angle and does not move, even when ordered to by the flight controller. Worst case scenario is a hardover, where the control surface is stuck in one of its extreme limit.	High	-Partial loss of aerodynamical pitch control -Undesired Pitching Moment

Actuators 2/6

Severity of Effects	Solution	Questions to be answered
Low	INDI compensation (acts as a disturbance)	How much can INDI compensate?
Low	Partial INDI compensation	How much can INDI compensate?
Low	<ul style="list-style-type: none"> -Redundant Control Surface using Splitted Control Surface [8] -Natural directional stability of aircraft -Directional control using hover motors (torque) 	<ul style="list-style-type: none"> -How damped is the lateral behavior of the aircraft in forward flight? -Is there significant yaw moment during the start of the transition (before motor spin up), that could not be counteracted? -How much downforce can the motor create trying to counteract torque? Can that downforce be compensated by the wing?
Medium	<p><u>Forward Flight:</u></p> <ul style="list-style-type: none"> -Redundant Control Surface using Splitted Control Surface [8] -New trim position with sideslip can be achieved [7] -Counteract undesired yaw moment using hover motors (torque) and roll moment using ailerons <p><u>Hover:</u></p> <ul style="list-style-type: none"> -Low airspeed, hence should not have significant effect 	<ul style="list-style-type: none"> -In what enveloppe can a sideslip (beta angle) compensate for the undesired yawing moment? -In what enveloppe can hover motors compensate for the loss directional control? (at high speed, might not be able to counteract vertical stabilizer moment)
Low	INDI compensation (acts as a disturbance)	How much can INDI compensate?
Low	Partial INDI compensation	How much can INDI compensate?
Medium	<p><u>Forward Flight</u></p> <ul style="list-style-type: none"> -Redundant Control Surface using Splitted Control Surface [8] -Attain equilibrium position with increased angle of attack and different speed [7] -Pitch Control using hover motors -Possible to obtain some pitch control using ailerons with wing skew <p><u>Transition:</u></p> <ul style="list-style-type: none"> -tbd, see questions <p><u>Hover:</u></p> <ul style="list-style-type: none"> -low airspeed, hence should not have significant effect 	<ul style="list-style-type: none"> -How much pitching authority can be gained by skewing the wing slightly? -Does skewing the wing lead to any instability (negative angle of attack on horizontal stabilizer?) or loss of rolling moment effectiveness? -Can transition be achieved without elevator? (in the critical 30 deg of skew)?
High	<p><u>Forward Flight</u></p> <ul style="list-style-type: none"> -Redundant Control Surface using Splitted Control Surface [8] -Counteract pitch control using hover motors -Possible to obtain some pitch control using ailerons with wing skew <p><u>Transition:</u></p> <ul style="list-style-type: none"> -Pitch Control using hover motors <p><u>Hover:</u></p> <ul style="list-style-type: none"> -low airspeed, hence should not have significant effect 	<ul style="list-style-type: none"> -At what airspeed does the elevator overpower the pitching moment achievable using the hover motors?

Actuators 3/6

Component	Potential Failure Mode	Explanation	Probability	Potential Failure Effects
Ailerons	Offset	The actual deflection of the control surface is offset from the required control surface deflection	Low	-Control surface not where controller think it is: undesired roll moment
	Unpredicted Dynamics Change (gain, response)	The actuator has different dynamics than the modeled dynamics (for example: much slower actuator)	Low	-transient response different, most probably slower
	Floating surface (stays neutral)	Control surface is no longer actuated or stays in neutral position.	High	Partial loss of aerodynamical roll control
	Stuck in position	Control surface holds a specific deflection angle and does not move, even when ordered to by the flight controller. Worst case scenario is a hardover, where the control surface is stuck in one of its extreme limit.	High	-Partial loss of aerodynamical roll control -Undesired Roll Moment
Wing rotation	Offset	The actual deflection of the control surface is offset from the required control surface deflection	Medium	Wrong skew angle leading to wrong actuator Effectiveness Matrix
	Stuck in position	Wing holds a specific deflection angle and does not move, even when ordered to by the flight controller. Worst case scenario is a hardover, where the wing is stuck in one of its extreme limit.	Medium	-If in hover phase, unable to transition. -If in transition, stuck in unstable position -If in forward flight, stuck in high speed configuration
	Free-floating	Wing rotating mechanism is free floating. The wing can tilt freely	Low	-wing rotation depending on flight manoeuvre -highly unpredictable
Hover Motor (fixed)	Loss in Performance	Motor is producing less thrust than its normal performance.	Low	-Lower pitch effectiveness -Lower vertical force effectiveness -Lower reactionary torque effectiveness
	Complete loss	Motor is producing 0 thrust.	Medium	-Lower pitch effectiveness -Lower vertical force effectiveness -Reactionary torque
	Stuck in position	Motor is producing thrust when it should not. Worst case is motor producing 100% thrust.	Low	-Undesired pitching moment -Undesired vertical force -Undesired reactionary torque

Actuators 4/6

Severity of Effects	Solution	Questions to be answered
Low	INDI compensation (acts as a disturbance)	How much can INDI compensate?
Low	Partial INDI compensation	How much can INDI compensate?
Low	<u>Forward Flight:</u> -Use other ailerons to induce roll moments, with reduce effectiveness overall [8] -If required, skew wing to get hover motor outside fuselage and apply rolling moments <u>Transition:</u> -Use hover motors for rolling moments <u>Hover:</u> -low airspeed, hence should not have significant effect	-Can the remaining aileron produce enough rolling moment? -Can the wing transition back to normal using only one aileron (reduce control effectiveness)
Low	<u>Forward Flight:</u> -Use other ailerons to counteract roll moments [8] -If required, skew wing to get hover motor outside fuselage and apply rolling moments <u>Transition:</u> -Use hover motors for rolling moment <u>Hover:</u> -low airspeed, hence should not have significant effect	-Can the wing transition back to normal if an aileron is stuck in downward position? -How big of a pitching moment can be created in forward flight by two ailerons? -During transition, the stuck aileron will induce pitching and rolling moment. Can the other aileron, elevator and hover motor counteract it?
High	Measure Skew Angle with sensor	Is skew angle already measured and feed back to the controller?
Medium	<u>Hover:</u> -Stop transition and come back to a hover <u>Transition:</u> -tbd <u>Forward Flight:</u> -Stop transition and land as an airplane, with hover motors active to reduce airspeed	-If in hover and try to do transition (or in forward flight to hover transition) but wing does not rotate, how are control allocated? -What are skew angle in which aircraft is still stable?
Medium	<u>Hover Flight:</u> -angled motor induce a torque that keeps the wing closed over the fuselage <u>Transition:</u> -tbd <u>Forward flight:</u> -Keep aircraft in a sideslip to induce drag that should keep wing open in fixed wing configuration -Alternatively, the ailerons can be used to create that torque	-Is the torque induced by the angled motors enough to keep the wing close over the fuselage? -How much sideslip or aileron input is required to keep the wing open in forward flight configuration? -How to perform transition? Is it better to land in forward flight configuration?
Low	Possible partial INDI compensation	How much can INDI compensate?
High	<u>Hover:</u> -get in yawing equilibrium position (high rate rotation) <u>Transition:</u> -tbd <u>Forward Flight:</u> -Does not apply	-Is a yawing rolling equilibrium position possible with such a big drone and with a vertical stabilizer? -Can the drone accelerate fast enough on the yaw axis?
High	<u>Hover:</u> -counteract pitching moment with other motor -reduce other pair of motor to keep hover flight -get in yawing equilibrium position (incline the vertical force vector) while keeping altitude <u>Transition:</u> -tbd <u>Forward flight:</u> -Does not apply	-Can the drone get into a stable yawing equilibrium position?

Actuators 5/6

Component	Potential Failure Mode	Explanation	Probability	Potential Failure Effects
Hover Motor (skewing)	Loss in Performance	Motor is producing less thrust than its normal performance.	Low	-Lower pitch and roll effectiveness -Lower vertical force effectiveness -Lower reactionary torque effectiveness
	Complete loss	Motor is producing 0 thrust.	Medium	-Lower pitch effectiveness -Lower vertical force effectiveness -Reactionary torque
	Stuck in position	Motor is producing thrust when it should not. Worst case is motor producing 100% thrust.	Low	-Undesired pitching and rolling moment (depending on skew angle) -Undesired vertical force -Undesired reactionary torque
Pusher Motor	Loss in Performance	Motor is producing less thrust than its normal performance.	Low	Partial loss of forward thrust
	Complete loss	Motor is producing 0 thrust.	Medium	Loss of forward thrust
	Stuck in position	Motor is producing thrust when it should not. Worst case is motor producing 100% thrust.	Low	Undesired forward thrust

Actuators 6/6

Severity of Effects	Solution	Questions to be answered
High	Possible partial INDI compensation	How much can INDI compensate?
High	<u>Hover:</u> -get in yawing equilibrium position (high rate rotation) <u>Transition:</u> -tbd <u>Forward Flight:</u> -Does not apply	-Is a yawing rolling equilibrium position possible with such a big drone and with a vertical stabilizer? -Can the drone accelerate fast enough on the yaw axis?
High	<u>Hover:</u> -counteract pitching moment with other motor -reduce other pair of motor to keep hover flight -get in yawing equilibrium position (incline the vertical force vector) while keeping altitude <u>Transition:</u> -tbd <u>Forward flight:</u> -Does not apply	-Can the drone get into a stable yawing equilibrium position? -Can transition be completed with a motor stuck?
Low	<u>Hover:</u> -Tilt drone to induce forward flight (as was already implemented) <u>Transition:</u> -Tilt drone to induce forward flight <u>Forward Flight:</u> -Reduce top speed	How much can INDI compensate? How much actuator loss is too much?
Medium	<u>Hover:</u> -Not applicable <u>Transition:</u> -Not perform transition <u>Forward Flight:</u> -Glide to get forward velocity	Can the drone transition while in a glide?
High	<u>Hover:</u> -Tilt drone to counteract forward thrust by pusher motor <u>Transition:</u> -Not perform transition <u>Forward Flight:</u> -tbd	What angle is required by thrust motors to compensate full forward pusher thrust?

Sensors 1/2

Component	Potential Failure Mode	Explanation	Probability	Potential Failure Effects
Gyroscopes	Bias	The actual state is offset from the measured state	Low	Wrong attitude calculation
	Increased noise	The sensor's reading has more noise in the signal	Low	Increased variability in sensor reading
	No value / stuck at value	The sensor's reading is 0 or stuck at a value. No valid state reading is provided.	Low	Wrong attitude calculation
Accelerometers	Bias	The actual state is offset from the measured state	Low	Wrong attitude calculation
	Increased noise	The sensor's reading has more noise in the signal	Low	Increased variability in sensor reading
	No value / stuck at value	The sensor's reading is 0 or stuck at a value. No valid state reading is provided.	Low	Wrong attitude calculation
Wing angle	Bias	The actual state is offset from the measured state	Low	Wing is not where vehicle think it is. Wrong calculation of control effectiveness
	Increased noise	The sensor's reading has more noise in the signal	Low	Increased variability in sensor reading
	No value / stuck at value	The sensor's reading is 0 or stuck at a value. No valid state reading is provided.	Low	Wing is not where vehicle think it is. Wrong calculation of control effectiveness.
Pitot tube	Bias (static hole plugged)	The actual state is offset from the measured state	Medium	-Perform transition at a lower speed than required -Underestimate or overestimate airspeed in control effectiveness matrix
	Increased noise (sensor issue)	The sensor's reading has more noise in the signal	Low	Increased variability in sensor reading
	No value (Dynamic hole plugged)	The sensor's reading is 0 or stuck at a value. No valid state reading is provided.	High	Unable to know airspeed to estimate control effectiveness of vehicle
	Stuck at value (sensor issue)	The sensor's reading is 0 or stuck at a value. No valid state reading is provided.	High	Wrong control Effectiveness Airspeed might decrease without the vehicle knowing and stall can happen
GPS	Bias	The actual state is offset from the measured state	Low	Vehicle thinks its at a certain position but is offset
	Increased noise	The sensor's reading has more noise in the signal	Low	Increased variability in sensor reading
	No value / stuck at value	The sensor's reading is 0 or stuck at a value. No valid state reading is provided.	Low	No more GPS position estimation.
Magnetometer	Bias	The actual state is offset from the measured state	Low	Vehicle thinks it is heading in a different attitude that it is, leading to some sideslip
	Increased noise	The sensor's reading has more noise in the signal	Low	Increased variability in sensor reading
	No value / stuck at value	The sensor's reading is 0 or stuck at a value. No valid state reading is provided.	Low	Vehicle no longer knows its heading

Sensors 2/2

Severity of Effects	Solution	Questions to be answered
High	Triple Redundant IMU [9]	-
High	Triple Redundant IMU [9]	-
High	Triple Redundant IMU [9]	-
High	Triple Redundant IMU [9]	-
High	Triple Redundant IMU [9]	-
High	Triple Redundant IMU [9]	-
High	<ul style="list-style-type: none"> -Use last known wing angle position as position. Keep wing as it is. -Redundancy 	<ul style="list-style-type: none"> -How can redundancy be integrated in the wing angle sensor system to identify faults and isolate the faulty sensor? -Could control effectiveness be estimated online to estimate the wing angle?
Low	<ul style="list-style-type: none"> -Use last known wing angle position as position. Keep wing as it is. -Estimate the wing angle by estimating the control effectiveness of actuators -Redundancy 	-
High	<ul style="list-style-type: none"> -Use last known wing angle position as position. Keep wing as it is. -Estimate the wing angle by estimating the control effectiveness of actuators -Redundancy 	<ul style="list-style-type: none"> -How can redundancy be integrated in the wing angle sensor system to identify faults and isolate the faulty sensor? -Could control effectiveness be estimated online to estimate the wing angle?
Low	<ul style="list-style-type: none"> -Estimate the wing angle by estimating the control effectiveness of actuators 	<ul style="list-style-type: none"> -Which methods can be used to estimate airspeed without a pitot tube, for a hybrid aircraft in different flight phases using conventional sensors? -By what means can the stability of the aircraft be maintained with uncertainty on airspeed? -Which methods for a pitot tube failure can be used to detect a pitot tube failure?
Low		
High		
High		
Low	Use IMU and dead reckoning	-
Low	Use IMU and dead reckoning	-
Low	Use IMU and dead reckoning	At which rate does the IMU position drift once GPS position is lost?
Low	Triple Redundant IMU [9]	-
Low	Triple Redundant IMU [9]	-
Low	Triple Redundant IMU [9] Use GPS to estimate Psi [10]	-

Sources 1/1	
Reference #	Complete Reference
[1]	Justin Fortna Murtha. An Evidence Theoretic Approach to Design of Reliable Low-Cost UAVs. Tech. rep. 2009.
[2]	Remma Matsuda, Tatsuya Ibuki, and Mitsuji Sampei. A Hoverability Analysis Method for Multi-rotor UAVs with a Case Study on Fault Tolerance; A Hoverability Analysis Method for Multirotor UAVs with a Case Study on Fault Tolerance. 2018. isbn: 9781538613955. doi: 10.0/Linux-x86\64.
[3]	Enrico Petritoli, Fabio Leccese, and Lorenzo Ciani. “Reliability assessment of UAV systems”. In: 4th IEEE International Workshop on Metrology for AeroSpace, MetroAeroSpace 2017 - Proceedings. Institute of Electrical and Electronics Engineers Inc., Aug. 2017, pp. 266–270. isbn: 9781509042340. doi: 10.1109/MetroAeroSpace.2017.7999577
[4]	Shawn Reimann et al. UAV for Reliability. Tech. rep. 2013.
[5]	Secretary of Defense. Defense Science Board Study on unmanned Aerial Vehicles and Uninhabited Combat Aerial Vehicles. Tech. rep. 2004.
[6]	Dainius Udris, Domantas Bru'cas, and Raimondas Pomarnacki. “Reliability Improvement of Power Distribution System for UAV”. In: (). doi: 10.3390/electronics8060636. url: www.mdpi.com/journal/electronics.
[7]	Raghu Venkataraman et al. “Reliability assessment of actuator architectures for unmanned aircraft”. In: IFAC-PapersOnLine. Vol. 28. 21. Sept. 2015, pp. 398–403. doi: 10.1016/j.ifacol.2015.09.559.
[8]	Marcin Zugaj, Przemyslaw Bibik, and Mariusz Jacewicz. “UAV aircraft model for control system failures analysis”. In: Journal of Theoretical and Applied Mechanics (Poland) 54.4 (2016), pp. 1405–1415. issn: 14292955. doi: 10.15632/jtam-pl.54.4.1405.
[9]	Ardupilot. The Cube Module Overview - CubePilot. 2022. url: https://docs.cubepilot.org/user-guides/autopilot/the-cube-module-overview
[10]	Strategies for sensor-fault compensation on UAVs: Review, discussions & additions
[11]	Diagnosis of Airspeed Measurement Faults for Unmanned Aerial Vehicles
[12]	Air data fault detection and isolation for small UAS using integrity monitoring framework
[13]	Raghu Venkataraman et al. “Reliability assessment of actuator architectures for unmanned air craft”. In: IFACPapersOnLine . Vol. 28. 21. Sept. 2015, pp. 398–403. DOI: 10.1016/j.ifacol.2015.09.559.
[14]	Paul Freeman and Gary J. Balas. “Actuation failure modes and effects analysis for a small UAV”. In: Proceedings of the American Control Conference. Institute of Electrical and Electronics Engineers Inc., 2014, pp. 1292–1297. ISBN: 9781479932726. DOI: 10.1109/ACC.2014.6859482.

Probability of failure 1/1

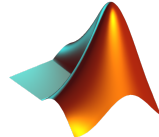
Component	Failure Probability	Justification
Servo	High	failure after 50 hours of use for high torque servo under normal aero loads [1]
		failure after 2 min of maximum torque [6]
Airframe	Low	Airframe is highly reliable due to ability to properly model airload and apply sufficient safety factor [3]

B

Rotor Loss Initial Calculations

As part of the evaluation of the rotor loss failure case, equations governing the rotating equilibrium yaw rate state presented initially by Mueller W. Mark and D'Andrea Raffaello [43] was reproduced. Modeling of the vertical tail stabilizer and the angled hover motors was added. The simulation aimed to identify the effect of those modifications and see if the vehicle could reach the equilibrium position rapidly enough to not lose control. A PDF version of the initial calculations is presented in the following pages. Alternatively, a digital version is attached to this report¹.

Click the icon to access the full Matlab File or download it to your computer²



¹A digital version of this document can be found on <https://repository.tudelft.nl>

²Make sure your PDF reader is compatible with attachments. Adobe Acrobat Reader and Foxit PDF Reader are.

Quadcopter with Loss of One Rotor

Initialization

```
clear all
close all
clc
```

Conventions

Code based on (Mueller, 2014):

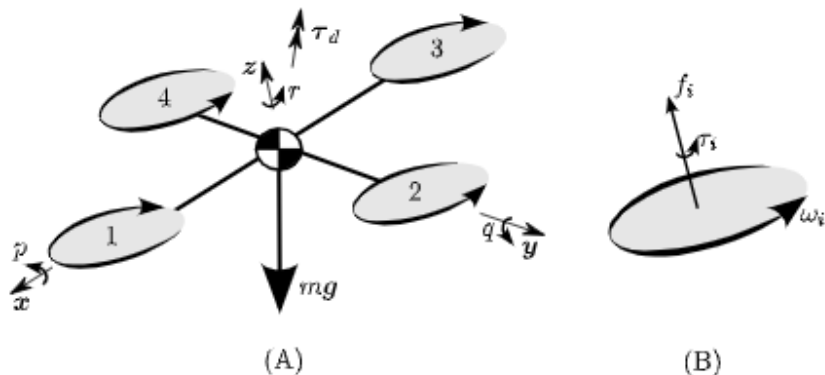


Fig. 2. (A) A dynamic model of a quadrocopter with four propellers arranged symmetrically about the vehicle centre of mass, showing a body-fixed reference frame consisting of the directions \mathbf{x} , \mathbf{y} and \mathbf{z} . Propellers 1 and 3 rotate in the opposite sense of propellers 2 and 4. A drag torque τ_d acts to oppose the vehicle's angular velocity ω^B expressed in the body-fixed frame as $\omega^B = (p, q, r)$. The vehicle has a weight force mg . (B) shows a detail of a propeller i rotating at angular velocity ω_i with respect to the body. Each propeller produces a thrust force f_i and torque τ_i , both in the direction of the propeller's axis of rotation. As drawn in (B), $\omega_i > 0$, and $\tau_i < 0$.

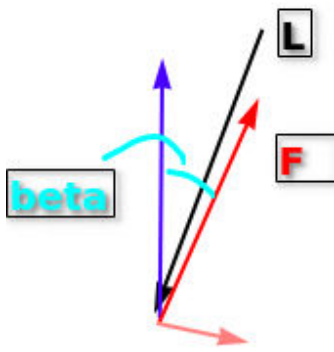
Where:

$$\tau_i = (-1)^i \kappa_f f_i$$

$$f_i = \kappa_f \omega_i^2$$

Model Additions: Tilted Hover Motors and Tail

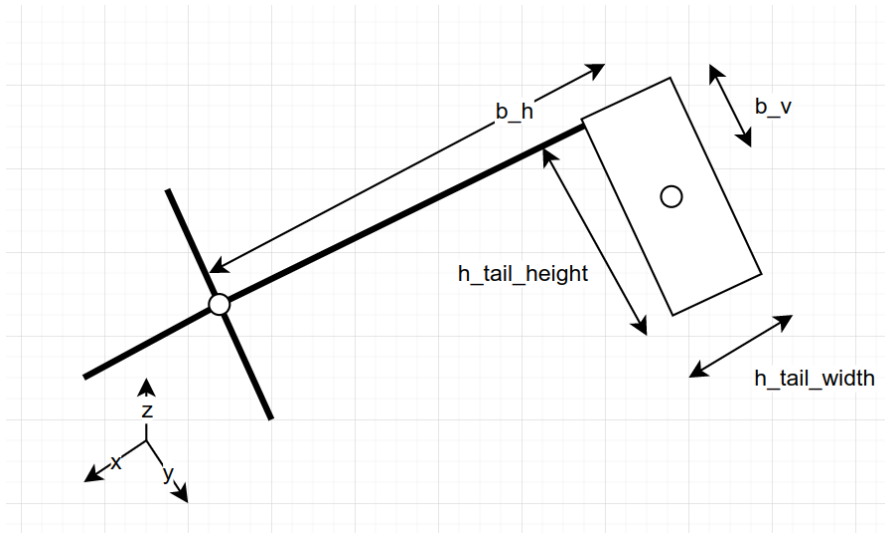
We model the hover motors as tilted with a angle beta:



Where a part of the force generated by the rotor is projected to the side, generating a yawing moment:

$$M_z = f_i \sin(\beta) l$$

The vertical stabilizer at the end of the vehicle can generate forces when turned around its yaw axis. The vertical stabilizer is assumed to act as a flat plate. Note that the horizontal tail stabilizer is not modeled, but could be added using the same method.



$$M_z = F b_h = 0.5 \rho v^2 C_d S b_h = 0.5 \rho (r b_h)^2 C_d S b_h = 0.5 \rho r^2 C_d S b_h^3$$

$$M_x = F b_v = 0.5 \rho v^2 C_d S b_v = \rho r^2 C_d S b_h^2 b_v$$

The full derivation of the model is presented in the "equation" section. The platform first needs to be selected.

Choosing Platform

By selecting the "mueller" platform, all the parameters used by Mueller in its paper can be reused, to reproduce its results. The "prototype" platform is in reference to the first iteration of the variable skew quad plane (VSQP). The "VSQP" platform is the best estimation of the new version of VSQP, with parameters estimated using CAD data, motor benchmark data and using existing data from the prototype.

```

platform = "VSQP_V2";

rho = 1.225; %kg/m^3

%% Parameters
switch platform
    case "mueller"
        % Parameters from (Mueller, 2014)
        I_xx_T = 3.2E-3; %kg m^2
        I_zz_T = 5.5E-3; %kg m^2
        I_zz_P = 1.5E-5*1E-6; %kg mm^2
        I_xx_P = 0;
        g = 9.81; %m/s^2
        m = 0.5; %kg
        l = 0.17; %m
        k_f = 6.41E-6; %Ns^2/rad^2
        k_t = 1.69E-2; %Nm/N
        gamma_1_z = 2.75E-3; %Nms/rad
        gamma_1_x = 0;
        gamma_2_z = 0; %Nms^2/rad^2
        gamma_2_x = 0;
        beta = 0; %rad

    case "prototype"
        %% Parameters (VSQP prototype)
        I_xx_T = 2.862E-2; % kg m^2 %(De Ponti, 2022) p.47
        I_zz_T = 2.158E-1; % kg m^2 %(De Ponti, 2022) p.47
        I_zz_P = 0; % kg m^2
        I_xx_P = 0; % kg m^2
        g = 9.81; %m/s^2
        m = 3; %kg %(De Ponti, 2022) p.47
        l = ((614+690)/2)/2/1000; %(De Ponti, 2022) p.48 %Average between fuselage
        % motor and arms length
        k_f = (3.4E-7)/((2*pi/60)^2); % RCtestbench test results for T motor MN3510-25
        k_t = 1.85E-2; % RCtestbench test results for T motor MN3510-25
        gamma_1_z = 0; %Nms/rad %proportionnal to r
        gamma_1_x = 0;
        Cd = 1.17; %(Hoerner 1992),p.3-17 drag coefficient for flat plates
        b_h = (1185-518-150/2)/1000; %m %(De Ponti, 2022) p.47-48
        S = ((75*300)+(300*75/2))*1E-6; %m^2 %(De Ponti, 2022) p.48
        gamma_2_z = 0.5*1.225*S*Cd*b_h^3; %Nms^2/rad^2 %proportionnal to r^2
        gamma_2_x = 0;
        beta = 0; %deg

    case "VSQP_V2"
        %% Parameters (VSQP V2)
        I_xx_T = 2.862E-2; % kg m^2 %Estimated from Prototype
        I_zz_T = 2.158E-1; % kg m^2 %Estimated from Prototype
        I_zz_P = 0; % kg m^2
        I_xx_P = 0; % kg m^2
        g = 9.81; %m/s^2
        m = 6.5; %kg

```

```

l = ((470+400)/2)/1000;
k_f = ((1.27E-6+8.75E-7)/2)/((2*pi/60)^2); %Based on RCtestbench results for T-motor
k_t = 2.85E-2; %Based on RCtestbench results for T-motor MN3520 400kv - Tarot 17x50
gamma_1_z = 0; %Nms/rad %proportionnal to r
gamma_1_x = 0; %Nms/rad %proportionnal to r
Cd = 1.17; %flat plane drag coefficient
h_tail_width = 0.17; %taken on V3 CAD %m
h_tail_height = 0.25; %taken on V3 CAD %m
b_h = 0.757; %taken on V3 CAD %m
b_v = h_tail_height/2; %taken on V3 CAD %m
S = h_tail_width*h_tail_height; %m^2
gamma_2_z = 0.5*rho*S*Cd*b_h^3; %Nms^2/rad^2 %M_z = F*b_h = 0.5*rho*v^2*Cd*S*b_h =
% = 0.5*rho*(r*b_h)^2*Cd*S*b_h = 0.5*rho*r^2*Cd*S*b_h^3
gamma_2_x = 0.5*rho*S*Cd*b_h^2*b_v; % M_x = F*b_v = 0.5*rho*(r*b_h)^2*Cd*S*b_v =
% = 0.5*rho*r^2*b_h^2*Cd*S*b_v
beta = deg2rad(3); %rad
end

```

Moments due to tail

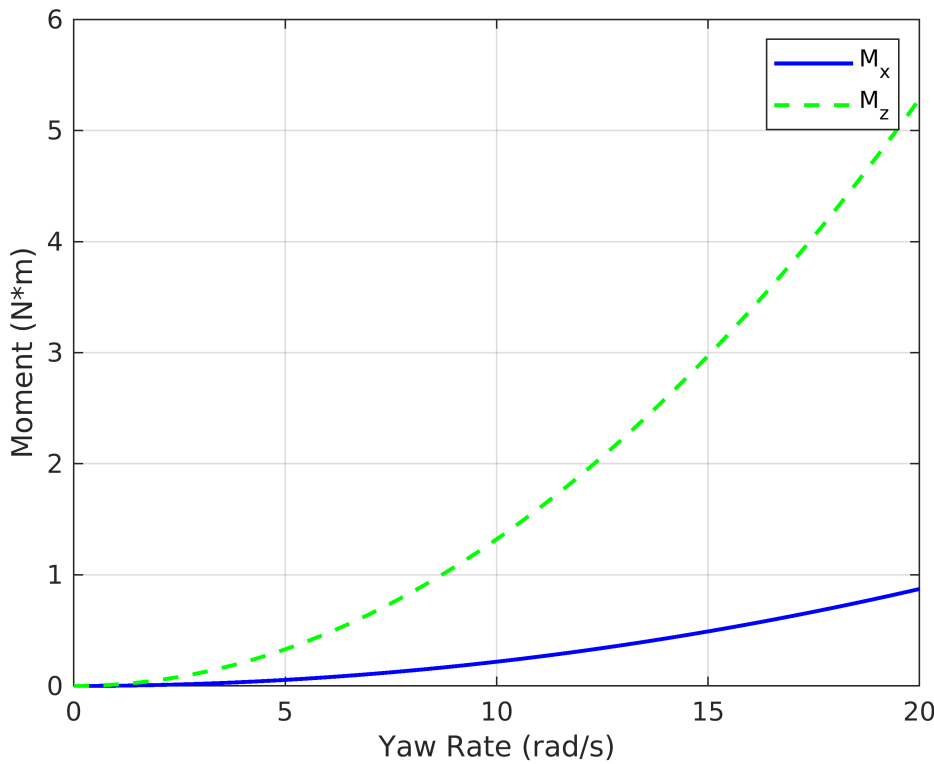
Estimation of the moment induced by the tail when spinning

```

r_list = [0:0.1:20]; %rad/s
M_x = gamma_1_x.*r_list+gamma_2_x.*r_list.^2; %N/m
M_z = gamma_1_z.*r_list+gamma_2_z.*r_list.^2; %N/m

% Plot moment created by tail spinning
figure
plot(r_list,M_x,'-b','LineWidth',1.5)
hold on
plot(r_list,M_z,'--g','LineWidth',1.5)
legend({'M_x','M_z'})
ylabel('Moment (N*m)')
xlabel('Yaw Rate (rad/s)')
grid on

```



It can be observed that the yaw moment increases sharply with yaw rate, opposing the rotation. The rolling moment induced by the tail is of much smaller magnitude than the yawing moment.

Equilibrium Equations

This section builds the whole model to estimate a new equilibrium state when rotating rapidly around a primary axis.

Original Equations 12-14:

$$\begin{aligned} I_{xx}^B \dot{p} &= \kappa_f (\omega_2^2 - \omega_4^2) l - (I_{zz}^T - I_{xx}^T) qr - I_{zz}^P q (\omega_1 + \omega_2 + \omega_3 + \omega_4), \\ I_{xx}^B \dot{q} &= \kappa_f (\omega_3^2 - \omega_1^2) l + (I_{zz}^T - I_{xx}^T) pr + I_{zz}^P p (\omega_1 + \omega_2 + \omega_3 + \omega_4). \\ I_{zz}^B \dot{r} &= -\gamma r + \kappa_r \kappa_f (\omega_1^2 - \omega_2^2 + \omega_3^2 - \omega_4^2). \end{aligned}$$

We modify equation 14 to adapt it to our case (tail creating yaw moment linear to r^2 in opposition to yaw direction + yaw due to angled motors):

$$I_{zz}^B \dot{r} = -\gamma_1 r - \gamma_2 r^2 + \kappa_r \kappa_f (\omega_1^2 - \omega_2^2 + \omega_3^2 - \omega_4^2) + \kappa_f l \sin(\beta) (\omega_1^2 - \omega_2^2 + \omega_3^2 - \omega_4^2)$$

We modify equation 12 to adapt it to our case (tail creating roll moment linear to r^2 of positive sign):

$$I_{xx}^B \dot{p} = \kappa_f (\omega_2^2 - \omega_4^2) l - (I_{zz}^T - I_{xx}^T) qr - I_{zz}^P q (\omega_1 + \omega_2 + \omega_3 + \omega_4) + \gamma_1 r + \gamma_2 r^2$$

Where the drag caused by the tail is modeled as:

$$\gamma_2 = \frac{1}{2} \rho S C_d b^3$$

And the moment caused by tilting the rotors:

$$M_z = \kappa_f l \sin(\beta) (\omega_1^2 - \omega_2^2 + \omega_3^2 - \omega_4^2)$$

Equation 16:

$$\bar{n} = e\bar{\omega}^B$$

Equation 17:

$$||\bar{n}|| = ||e\bar{\omega}^B|| = 1$$

Equation 18:

$$\bar{f}_\Sigma \bar{n}_z = m ||g||$$

Equation 10:

$$f_i = \kappa_f \omega_i^2$$

Failed propeller equations

If one propeller is failed:

$$\omega_4 = 0, \omega_1 = \omega_3$$

We add a new variable:

$$\rho = f_2/f_1$$

We have 11 unknowns:

$$\omega_1, \omega_2, \omega_3, \omega_4, n_x, n_y, n_z, p, q, r, \epsilon$$

Analysis Domain

This section analyzes the equilibrium state depending on the ratio of force between f_2 and f_1 .

```
% List of rho to evaluate
rho_incr = 0.1;
max_rho = 1.5;
rho_list = [0,[0.01:rho_incr:max_rho]];
% Delete rho = 2 (asymptote)
rho_list(rho_list==2) = [];
clear n_x_list n_y_list n_z_list p_list q_list r_list epsi_list ...
w_1_list w_2_list w_3_list w_4_list ...
f_1_list f_2_list f_3_list f_4_list r_ps_list
```

Solving Equations

```
% Iterate through all rho value
for i=1:length(rho_list)

    % Initialization
    clear sol temp_sol
    rho = rho_list(i); % Cleanup

    fprintf('Currently evaluating rho = %.2f\n',rho)

    % Symbolic variables
    syms n_x n_y n_z p q r epsi w_1 w_2 w_3 w_4 f_1 f_2 f_3 f_4

    % Equations
    % Eq 10 (Force proportionnal to angular velocity squared)
    eqn10 = [f_1 == w_1^2*k_f, f_2 == w_2^2*k_f, f_3 == w_3^2*k_f, f_4 == w_4^2*k_f];

    % Eq 16 (Primary axis requirement)
    eqn16 = [n_x == epsi*p, n_y == epsi*q, n_z == epsi*r];

    % Eq 17 (Unit vector requirement)
    eqn17 = sqrt(n_x^2+n_y^2+n_z^2) == 1;

    % Eq 18 (Sum of forces equal in z)
    eqn18 = (f_1+f_2+f_3+f_4)*n_z == m*g;

    % Eq 12 (Rotationnal roll)
    eqn12 = 0 == k_f*(w_2^2-w_4^2)*l-(I_zz_T-I_xx_T)*q*r-I_zz_P*q*(w_1+w_2+w_3+w_4)+...
        gamma_1_x*r+gamma_2_x*r^2;

    % Eq 13 (Rotationnal pitch)
    eqn13 = 0 == k_f*(w_3^2-w_1^2)*l+(I_zz_T-I_xx_T)*p*r+I_zz_P*p*(w_1+w_2+w_3+w_4);

    % Eq 14 (Rotationnal yaw)
    eqn14 = 0 == -gamma_1_z*r-gamma_2_z*r^2+k_t*k_f*(w_1^2-w_2^2+w_3^2-w_4^2)+...
        sin(beta)*l*k_f*(w_1^2-w_2^2+w_3^2-w_4^2);

    % One failed propeller
    eqn_failed = [ w_4 == 0, w_1 == w_3 ];
    eqn_rho = rho == f_2/f_1;

    % System of equations
    eqn = [eqn10 eqn16 eqn17 eqn18 eqn12 eqn13 eqn14 eqn_failed eqn_rho];

    % Solve
    temp_sol = solve(eqn); %vpasolve and solve with conditions did not work

    % Select only real values with positive angular propeller speed
    fn = fieldnames(temp_sol);
    c = cell(length(fn),1);
    sol = cell2struct(c,fn);
```

```

for j=1:length(temp_sol.(fn{1}))
    if isreal(double(temp_sol.w_1(j))) && double(temp_sol.w_1(j))>=0 && ...
        double(temp_sol.w_2(j))>=0 && double(temp_sol.w_3(j))>=0 && ...
        double(temp_sol.w_4(j))>=0 && temp_sol.r(j)>=0
        for k=1:length(fn)
            sol.(fn{k})(end+1) = double(temp_sol.(fn{k}))(j));
        end
    end
end

% Save results
% Primary Axis
n_x_list(i) = double(sol.n_x);
n_y_list(i) = double(sol.n_y);
n_z_list(i) = double(sol.n_z);

% Angular Rates
p_list(i) = double(sol.p);
q_list(i) = double(sol.q);
r_list(i) = double(sol.r);

epsi_list(i) = double(sol.epsi);

%Propeller Angular Rates
w_1_list(i) = double(sol.w_1);
w_2_list(i) = double(sol.w_2);
w_3_list(i) = double(sol.w_3);
w_4_list(i) = double(sol.w_4);

%Thrust Forces
f_1_list(i) = double(sol.f_1);
f_2_list(i) = double(sol.f_2);
f_3_list(i) = double(sol.f_3);
f_4_list(i) = double(sol.f_4);

% Radius of turn
r_ps_list(i) = sqrt(1-n_z_list(i)^2)*g/(n_z_list(i)*(1	epsi_list(i))^2);

end

```

Currently evaluating rho = 0.00
 Currently evaluating rho = 0.01
 Currently evaluating rho = 0.11
 Currently evaluating rho = 0.21
 Currently evaluating rho = 0.31
 Currently evaluating rho = 0.41
 Currently evaluating rho = 0.51
 Currently evaluating rho = 0.61
 Currently evaluating rho = 0.71
 Currently evaluating rho = 0.81
 Currently evaluating rho = 0.91
 Currently evaluating rho = 1.01
 Currently evaluating rho = 1.11
 Currently evaluating rho = 1.21
 Currently evaluating rho = 1.31
 Currently evaluating rho = 1.41

Plot Results

```

%% Plot results
figure
% Angular Rates
subplot(4,1,1)
plot(rho_list,p_list,'-b','Linewidth',1.5)
hold on
plot(rho_list,q_list,'--g','Linewidth',1.5)
plot(rho_list(rho_list<2),r_list(rho_list<2),'-.r','Linewidth',1.5)
plot(rho_list(rho_list>2),r_list(rho_list>2),'-.r','Linewidth',1.5)
plot(rho_list,sqrt(p_list.^2+q_list.^2+r_list.^2),':c','Linewidth',1.5)
if strcmp(platform,'mueller')
    axis([0 10 -30 30])
else
    %axis([-inf inf 0 15])
end
legend({'p','q','r','w_b'})
ylabel('Rates (rad/s)')
grid on

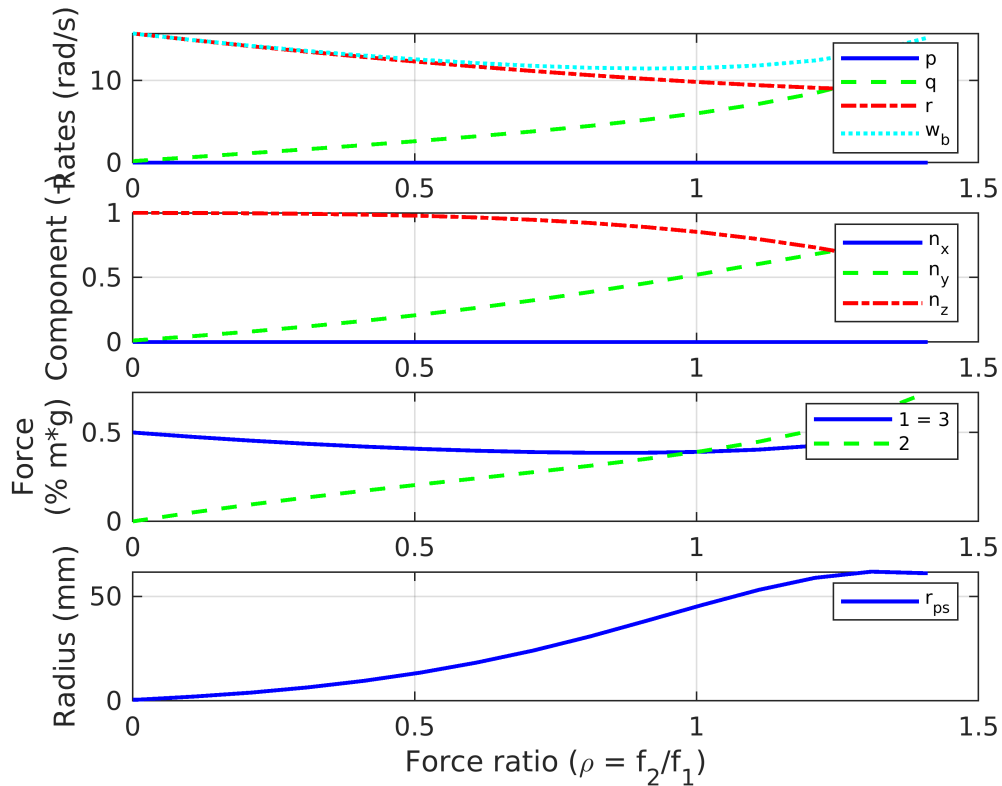
subplot(4,1,2)
% Vector
plot(rho_list,n_x_list,'-b','Linewidth',1.5)
hold on
plot(rho_list,n_y_list,'--g','Linewidth',1.5)
plot(rho_list,n_z_list,'-.r','Linewidth',1.5)
if strcmp(platform,'mueller')
axis([0 10 0 1])
end
legend('n_x','n_y','n_z')
ylabel('Component (-)')
grid on

subplot(4,1,3)
% Force
if strcmp(platform,'mueller')
    plot(rho_list,f_1_list,'-b','Linewidth',1.5)
    hold on
    plot(rho_list,f_2_list,'--g','Linewidth',1.5)
    axis([0 10 0 6])
    legend({'f_1 = f_3','f_2'})
    ylabel('Force (N)')
else
    plot(rho_list,f_1_list/(m*g),'-b','Linewidth',1.5)
    hold on
    plot(rho_list,f_2_list/(m*g),'--g','Linewidth',1.5)
    legend({'1 = 3','2'})
    ylabel(['Force',newline,'(% m*g)'])
end
grid on

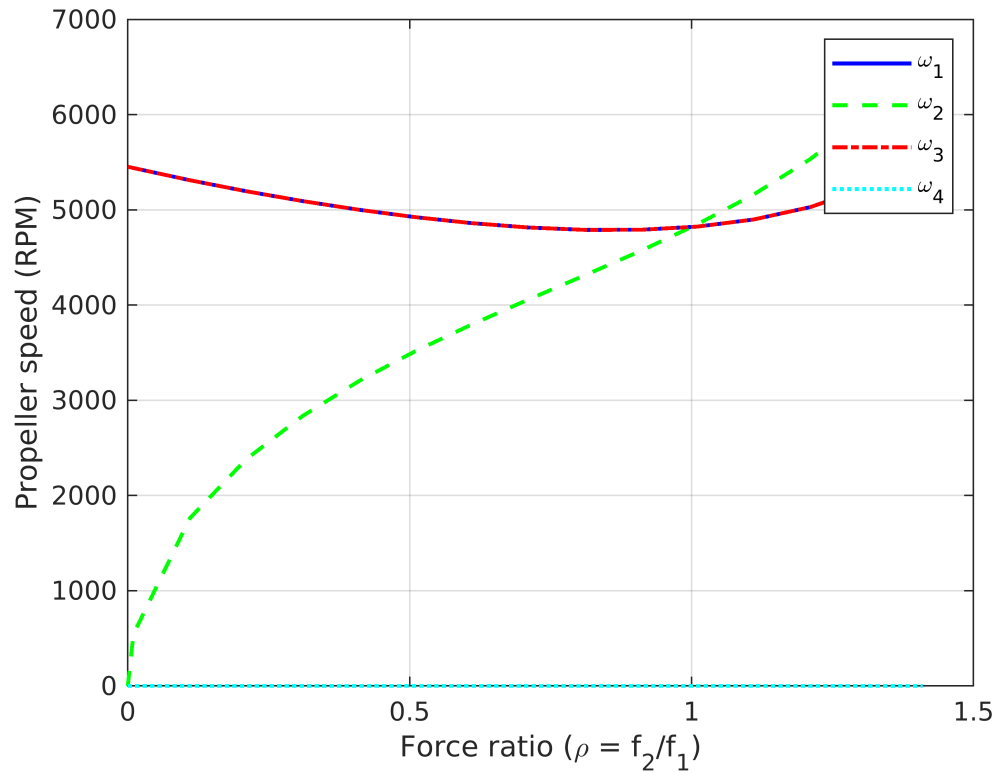
subplot(4,1,4)

```

```
% Radius
plot(rho_list,r_ps_list*1E3,'-b','Linewidth',1.5)
if strcmp(platform,'mueller')
axis([0 10 0 25])
end
legend('r_{ps}')
ylabel('Radius (mm)')
xlabel('Force ratio (\rho = f_2/f_1)')
grid on
```



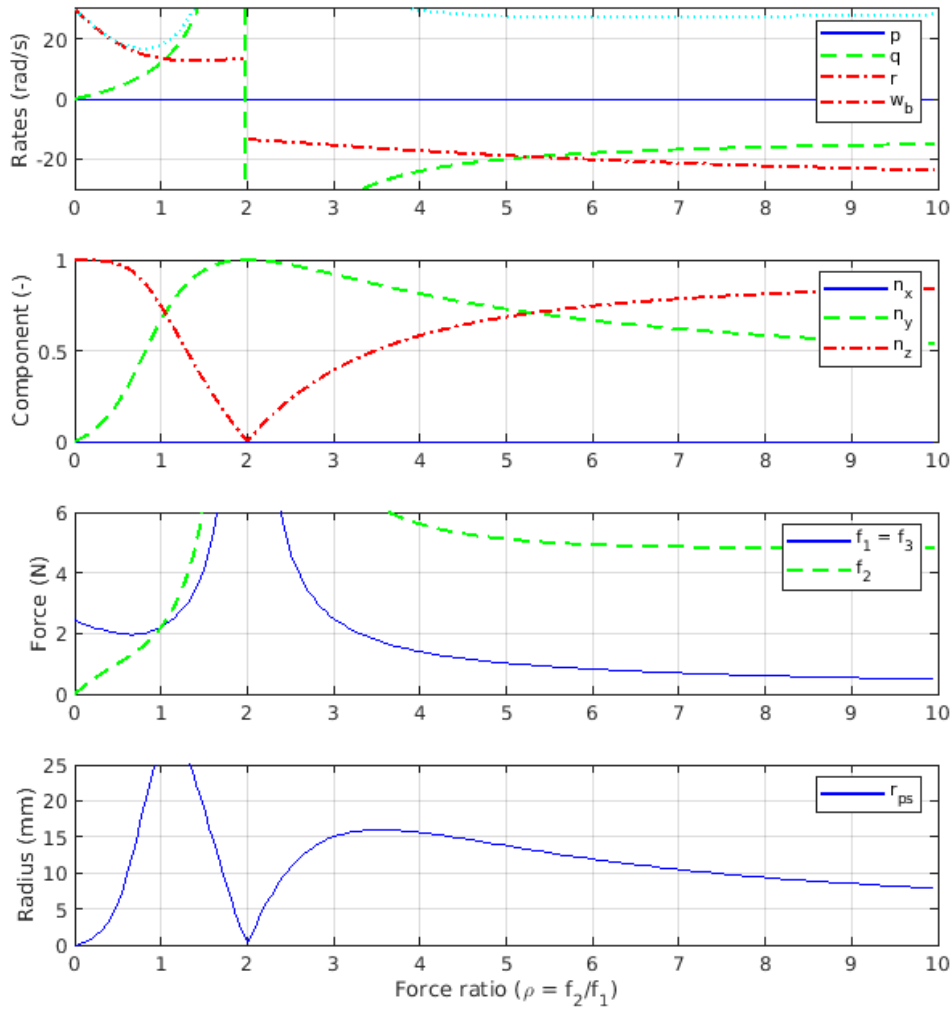
```
% Plot RPM depending on force ratio
figure
plot(rho_list,w_1_list*60/(2*pi),'-b','Linewidth',1.5)
hold on
plot(rho_list,w_2_list*60/(2*pi),'--g','Linewidth',1.5)
plot(rho_list,w_3_list*60/(2*pi),'-.r','Linewidth',1.5)
plot(rho_list,w_4_list*60/(2*pi),':c','Linewidth',1.5)
legend({'\omega_1','\omega_2','\omega_3','\omega_4'})
ylabel('Propeller speed (RPM)')
xlabel('Force ratio (\rho = f_2/f_1)')
grid on
```



Analysis of Results

Reproducing Mueller's data

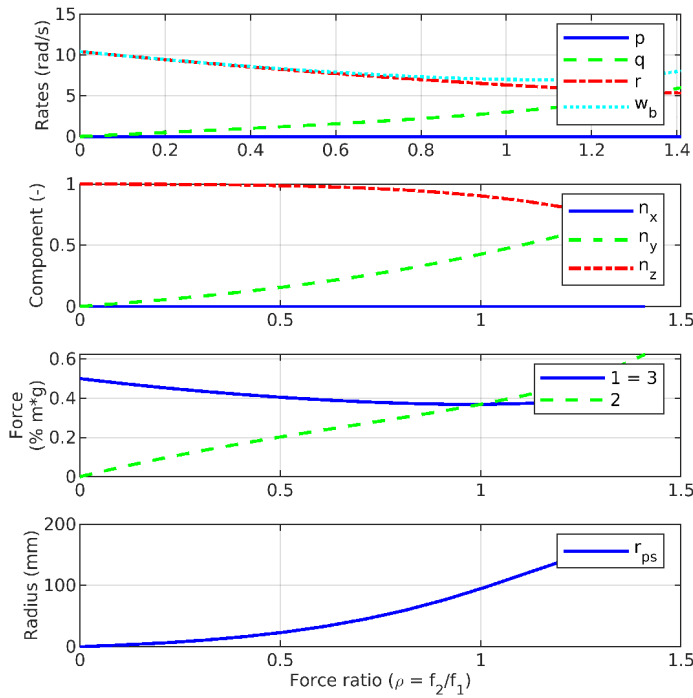
By selecting the "mueller" configuration, it is possible to reproduce the results presented in their paper. This serves as verification of the model. The results obtained using this matlab script are presented below:



Prototype

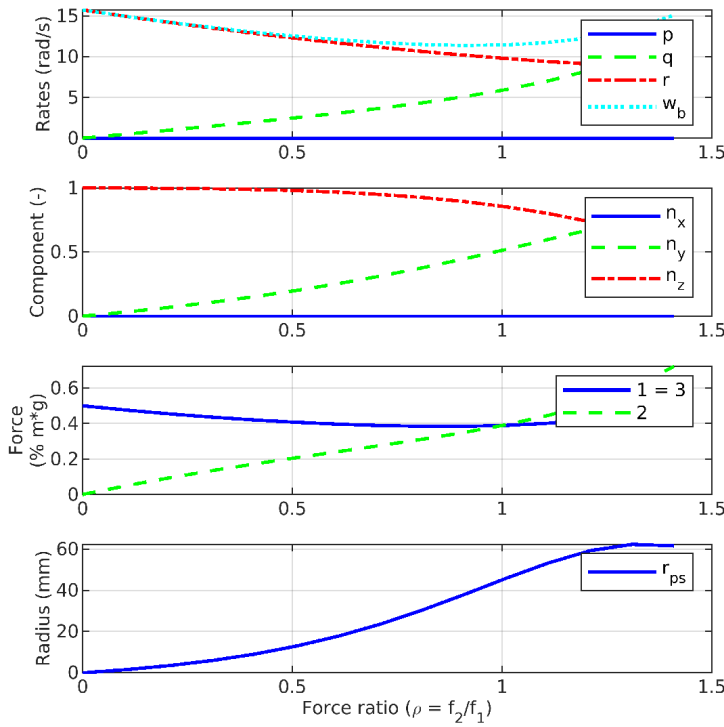
Selecting the "prototype" configuration calculates the equilibrium state for the prototype. It can be observed that the yaw rate required for equilibrium is significantly lower than for the "mueller" configuration. This is due to the increased rotational drag coefficient from the tail.

With a maximum thrust to weight ratio((TWR) of approx. 1.5, each VSQP prototype could lift 37.5% the weight of the prototype. The force required from the motors to maintain the equilibrium state is always higher than 0.38. This rotating equilibrium state is therefore unable to be maintained by the VSQP prototype. A higher TWR is required.



V2 VSQP

The following figure shows the rotating equilibrium state depending on the force ratio between f_1 and f_2 . Compared to the VSQP prototype, the V2 has a higher equilibrium yaw rate. This is due to the angled motors that generate yawing moment that increase the yaw rate. With a estimated TWR of 2, each motor of the V2 can lift 0.5 of their weight. With this increased TWR, a wide variety of equilibrium state can be reached.



Time to reach equilibrium point

This section aims to evaluate broadly how much time would be required to reach the equilibrium yaw rate. Ideally, this should take less than 1 second to guarantee fast transition from rotor loss to the equilibrium state.

Equation 14 is Reused:

$$I_{zz}^B \dot{r} = -\gamma_1 r - \gamma_2 r^2 + \kappa_f \kappa_f (\omega_1^2 - \omega_2^2 + \omega_3^2 - \omega_4^2) + \kappa_f l \sin(\beta) (\omega_1^2 - \omega_2^2 + \omega_3^2 - \omega_4^2)$$

It is assumed that the failure is detected instantaneously and that motors are instantaneously at max throttle.

Propeller max speed: approx. 5000 RPM

If one propeller is failed:

$$\omega_4 = 0, \omega_1 = \omega_3$$

```
dt = 0.005; %timestep
r_crit = 10; %rad/s
w_max = 5000/(60/(2*pi)); %rad/s

r = 0; % initial yaw rate
```

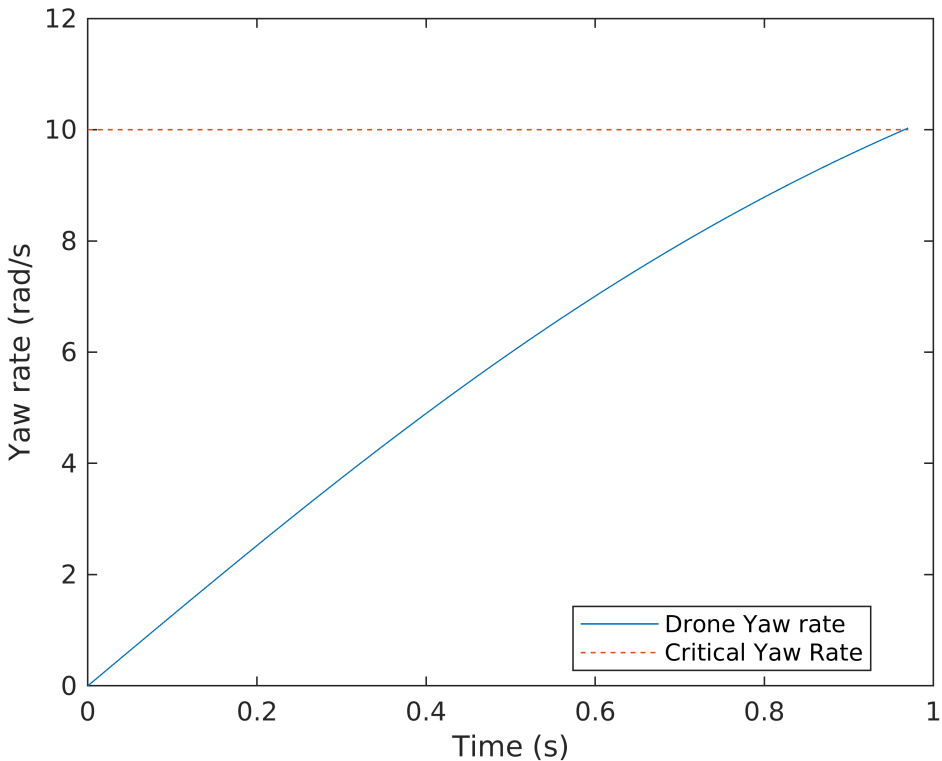
```
%torque assumed constant
torque = k_t*k_f*(w_max^2+0^2+w_max^2+0^2)+k_f*l*sin(beta)*(w_max^2+0^2+w_max^2+0^2);

% Loop to advance in time until the critical yawing speed is reached
while r(end)<r_crit
    r_dot = (-gamma_1_z*r(end)-gamma_2_z*r(end)^2+torque)/I_zz_T;
    r(end+1) = r_dot*dt+r(end);

    % Exit condition in case it is not reachable in less than 10 s
    if length(r)*dt > 10
        error('Time to reach critical yawing speed bigger than 10s')
    end

end

% Plot Results
t = [0:dt:dt*(length(r)-1)];
figure
plot(t,r)
hold on
plot([min(t) max(t)],[r_crit r_crit], '--')
xlabel('Time (s)')
ylabel('Yaw rate (rad/s)')
legend({'Drone Yaw rate', 'Critical Yaw Rate'}, 'location', 'best')
```



```
fprintf('Time to reach critical yawing speed: %.2f s\n',max(t))
```

Time to reach critical yawing speed: 0.97 s

Based on the following calculation for VSQP V2, the time required to reach the equilibrium yaw speed is approx. 1 sec. However, this does not take into account the time required to detect the fault and to spool up the motor.

References

(Mueller, 2014):

Mueller W. Mark and D'Andrea Raffaello. "Stability and control of a quadrocopter despite the complete loss of one, two, or three propellers". In: IEEE International Conference on Robotics and Automation. IEEE = Institute of Electrical and Electronics Engineers, 2014. ISBN: 9781479936847.

(De Ponti, 2022):

Tomaso De Ponti. Incremental Nonlinear Dynamic Inversion Controller for a Variable Skew Quad Plane. Delft: Master's Thesis, 2022

(Hoerner, 1992):

Cheeseman, I. (1976). Fluid-Dynamic Drag: Practical Information on Aerodynamic Drag and Hydrodynamic Resistance. S. F. Hoerner. Hoerner Fluid Dynamics, Brick Town, New Jersey. 1965. 455 pp. Illustrated. \$24.20. *The Aeronautical Journal* (1968), 80(788), 371-371. doi:10.1017/S0001924000034187